Master's thesis

NTNU
Norwegian University of Science and Technology
Faculty of Information Technology and Electrical Engineering
Department of Engineering Cybernetics

Håken Sivesindtajet Lunn

Control of power converters as Virtual Synchronous Machines for flexible system integration of single battery installation in a two-bus ship power system

Master's thesis in Industrial Cybernetics
Supervisor: Jon Are Wold Suul
June 2022

NTNU
Norwegian University of
Science and Technology

Håken Sivesindtajet Lunn

Control of power converters as Virtual Synchronous Machines for flexible system integration of single battery installation in a two-bus ship power system

Master's thesis in Industrial Cybernetics
Supervisor: Jon Are Wold Suul
June 2022

Norwegian University of Science and Technology
Faculty of Information Technology and Electrical Engineering
Department of Engineering Cybernetics

Preface

This report is the product of my Master's Thesis, estimated to be 30 credits, and the work was conducted between January 2022 and June 2022. The submission and completion of the Master's Thesis are the final mandatory tasks for completion of my Masters's degree in Industrial Cybernetics at the Norwegian University of Science and Technology (NTNU).

The project assignment is provided by NTNU, with the goal being to control power converters for flexible system integration of single battery installation in a two-bus ship power system. The Master's thesis is a continuation of my specialization project and will utilize the Synchronous Reference Frame (SRF) current controlled Voltage Source Converter (VSC) developed during my specialization project. The project has developed a complete simulation model of a two-bus ship power system to verify the effects of integrating a Virtual Synchronous Machine (VSM)-based Energy storage System (ESS) in a ship power system. The targeted audience is students with knowledge within cybernetics, power electronics, and other specialists represented as supervisors and industry representatives.

I want to thank my supervisor, Jon Are Wold Suul, for all his guidance throughout this project. His time, knowledge, and feedback have been key factors that enable the completion of this report.

Håken Sivesindtajet Lunn
Trondheim, June 2022

Summary

This project studies the control of power converters for simple battery integration in AC-distributed ship power systems utilizing the Virtual Synchronous Machine (VSM) control structure. The primary purpose of the VSM is to emulate the behaviors of a traditional Synchronous Machine (SM) in power converters and inherit important electromechanical properties contributing to grid stability. A VSM-based Energy storage System (ESS) can potentially improve stability and efficiency in AC-distributed ship power systems by providing an emission-free spinning reserve and enabling seamless transitions between the grid-following and grid-forming operation of the power converter.

However, to assess this, the project has developed a time-domain simulation model of a two-bus ship power system used to verify the effects of adding a dual-infeed VSM-based ESS in a two-bus ship power system. The VSM-controlled converter uses a reduced-order VSM architecture based on the Quasi-Stationary Electrical Model (QSEM), omitting the dynamical properties of the electrical model to reduce complexity while maintaining essential properties. Simulation results have shown that the immediate energy supply of batteries combined with the VSM-controlled converter design has increased grid stability by adding ”virtual” inertia and providing a fast primary frequency control. Furthermore, the simulation model shows that the VSM-based ESS reduces previous limitations related to battery integration in AC-distributed power systems and enables seamless transitions between load sharing, grid support, and islanded operation of the ESS. The dual-in-feed configuration using a common DC bus also provides ”virtual” closed bus ties and allows power cycling between each AC bus during operations with open bus ties. Further work on an Energy Management System (EMS) using the increased flexibility of a dual-infeed configured VSM-based ESS can potentially reduce operational costs and GHG emissions in ships by optimizing energy utilization.

Sammendrag

Prosjektet studerer kontroll av kraftelektronikkomformere for enkel batteriintegrasjon i AC-distribuerte fremdriftssystemer i skip ved hjelp av kontrollstrukturen kjent som ”virtuell” synkronmaskin (VSM). Hovedformålet med en VSM er å etterligne oppførselen til en tradisjonell synkronmaskin (SM) i en kraftelektronikkomformer og dermed arve viktige elektromekaniske egenskaper som bidrar til nettstabilitet. Et VSM-basert energilagringssystem (ESS) er forventet å kunne forbedre nettstabilitet og øke energieffektiviteten i AC-distribuerte fremdriftssystemer i skip ved å gi en utslippsfri roterende reserve, muliggjøre sømløse overganger mellom nettfølgende og nettdannende drift av kraftelektronikkomformere.

For å kunne verifisere effekten av å installere en VSM-basert ESS med dobbelinnmating i et to-buss fremdriftssystem har prosjektet utviklet en simuleringsmodell i tidsdomene. Det finnes mange forskjellige implementasjoner av VSMer, men dette prosjektet har valgt en løsning basert på en kvasi stasjonær elektrisk modell (QSEM), som utelater de dynamiske egenskaper av den elektriske SM modellen. En kontrollstruktur basert på en QSEM vil redusere kompleksiteten til VSMen, men samtidig opprettholde viktige elektromekaniske egenskaper til SMen. Simuleringsresultater har vist at den umiddelbare energitilførselen som batterier representerer kombinert med en VSM-kontrollerte kraftelektronikkomformere har økt nettstabiliteten ved å tilføre et ”virtuelt” treghetsmoment samt en hurtig frekvenskontroll. Videre viser simuleringsmodellen at en VSM-basert ESS reduserer tidligere begrensninger knyttet til batteriintegrasjon i AC-distribuerte kraftsystemer og muliggjør sømløse overganger mellom lastdeling, nettstøtte og øydrift av ESSen. En ESS med dobbelinnmating gir muligheten til å drifte systemet med en ”virtuelt” lukket buss som tillater energitransportering mellom AC-bussene i driftssituasjoner som krever separerte busser. Et videre arbeid med et energistyringssystem (EMS) som utnytter fleksibiliteten til en dobbelinnmatet VSM-basert ESS kan potensielt redusere driftskostnader og klimagassutslipp i ship.

Contents

List of Tables

List of Figures

Nomenclature

E_{gen}	The stored kinetic energy of a generator at nominal speed
H_{gen}	Inertia constant of a generator at nominal speed
H_{sys}	Total system inertia constant of the entire system at nominal speed
J_{gen}	Rotor inertia of a generator
S_{gen}	The power rating of a generator at nominal speed
S_{sys}	The power rating of the entire total system at nominal speed
ω_{gen}	Angular velocity of a generator
C_b	Base capacitance
I_b	Base current
L_b	Base inductance
R_b	Base resistance
S_b	Rated apparent power
V_b	Base AC-voltage
$V_{LL,RMS}$	Rated system voltage
$V_{b,dc}$	Base DC-voltage
δ	An unspecified phase angle of voltage or current in the $\alpha\beta$ reference frame
ω	An unspecified angular velocity of voltage or current in the $\alpha\beta$ reference frame
ω_b	Base angular velocity

θ	An unspecified phase angle of voltage or current in the dq reference frame
a	Phase a (0°)
b	Phase b (-120°)
c	Phase c (120°)
f_b	Rated system frequency
v_{AC}	AC-bus voltage
v_{DC}	DC-bus voltage
x	An unspecified voltage or current
x_0	An unspecified zero voltage or current
x_a	An unspecified phase a voltage or current
x_b	An unspecified phase b voltage or current
x_c	An unspecified phase c voltage or current
x_d	An unspecified d-axis voltage or current
x_q	An unspecified q-axis voltage or current
x_{abc}	An unspecified three-phase voltage or current
$x_{f,d}$	An unspecified low-pass filtered d-axis voltage or current
$x_{f,q}$	An unspecified low-pass filtered q-axis voltage or current
ω_f	PLL low-pass filter crossover frequency
ω_{PLL}	PLL per unit angular velocity
θ_{PLL}	PLL phase angle
$k_{p\delta}$	PLL integral gain
$k_{p\delta}$	PLL propositional gain
T_{sum}	VSC SRF CC linear delay approximation
γ	VSC SRF CC integral state
ω_{AD}	VSC SRF CC active damping crossover frequency
φ	VSC low-pass filtered capacitor voltage

c_f	VSC LCL-filter capacitance
i_c	VSC converter current
i_c^*	VSC converter current reference
$i_{c,d}$	VSC d-axis converter current
$i_{c,d}^*$	VSC d-axis converter current reference
$i_{c,q}$	VSC q-axis converter current
$i_{c,q}^*$	VSC q-axis converter current reference
k_{AD}	VSC SRF CC active damping gain
k_{ffc}	VSC SRF CC feedforward gain
k_{ic}	VSC SRF CC integral gain
k_{pc}	VSC SRF CC propositional gain
l_f	VSC LCL-filter inductance
m	VSC 1$^{\text{st}}$ harmonic modulation index in dq
m_3	VSC 3$^{\text{rd}}$ harmonic modulation index in $\alpha\beta$
m_d	VSC 1$^{\text{st}}$ harmonic q-axis modulation index
m_q	VSC 1$^{\text{st}}$ harmonic q-axis modulation index
m_{abc}	VSC three-phase 1$^{\text{st}}$ harmonic modulation index in $\alpha\beta$
r_{lf}	VSC LCL-filter resistance
v_c	VSC converter voltage
v_c^*	VSC converter voltage reference
v_f	VSC LCL-filter voltage
$v_{c,d}$	VSC d-axis converter voltage
$v_{c,d}^*$	VSC d-axis converter voltage reference
$v_{c,q}$	VSC q-axis converter voltage
$v_{c,q}^*$	VSC q-axis converter voltage reference
$v_{f,d}$	VSC d-axis LCL-filter voltage

$v_{f,q}$	VSC q-axis LCL-filter voltage
D	Damping coefficient
J_r	Rotor inertia
T_a	VSM inertia time constant
T_m	Mechanical torque
T_{el}	Electrical torque
$\hat{v}_e^*$	VSM internally induced voltage
$\hat{v}_f$	VSM filter voltage amplitude
$\hat{v}_f^*$	VSM filter voltage reference
ω_d	VSM inertia damping filter crossover frequency
ω_g	Angular velocity of the grid
ω_r	Angular velocity of the rotor
ω_{VMS}	VSM angular velocity
ω_m	VSM reactive power filter crossover frequency
ω_{vf}	VSM LCL-filter voltage low-pass filter crossover frequency
θ_{VMS}	VSM phase angle
ξ	VSM voltage controller integral state
$i_{vs,d}^{QSEM}$	QSEM virtual stator current d-axis
$i_{vs,q}^{QSEM}$	QSEM virtual stator current q-axis
i_{vs}	VSM virtual stator current
i_{vs}^{QSEM}	QSEM virtual stator current
k	Angular velocity feedback
k_ω	VSM frequency control gain
k_d	VSM inertia damping constant
k_{iv}	VSM voltage controller integral gain

k_{pv}	VSM voltage controller propositional gain
k_{qf}	VSM reactive power filter crossover frequency
k_q	VSM reactive power droop gain
l_{vs}	VSM virtual stator inductance
p^{r*}	Ideal power source
p_m	Mechanical power source
p_{VSM}	VSM active power
p^*_{VSM}	VSM active power reference
p_{el}	Electrical power
q_{VSM}	VSM reactive power
q^*_{VSM}	VSM reactive power reference
q_m	VSM low-pass filtered reactive power
r_{vs}	VSM virtual stator resistance
v_m	VSM LCL-filter voltage low-pass filtered
$v_{m,d}$	VSM d-axis LCL-filter voltage low-pass filtered
$v_{m,q}$	VSM q-axis LCL-filter voltage low-pass filtered
L_{f1d}	SM Canay inductance
S_{SM}	Nominal power of the generator
T_e	SM Prime mover time response
$V_{LL,RMS,SM}$	Nominal voltage of the generator
$\hat{v}_{SM}$	SM stator voltage
$\hat{v}^*_{SM}$	SM stator voltage reference
$\mathbf{i^r}$	SM current vector
$\mathbf{l^r}$	SM internal inductance matrix
$\mathbf{r^r}$	SM internal resistance matrix
$\mathbf{v^r}$	SM voltage vector

ω_e	SM Prime mover crossover frequency
$\omega_r \mathbf{J}\boldsymbol{\Psi}^{\mathbf{r}}$	SM decoupling matrix
ω_{qfg}	SM reactive power filter crossover frequency
τ	SM Prime mover fuel command
ζ	SM voltage controller integral state
f_{SM}	Nominal frequency of the generator
$f_{f,sm}$	Friction factor of the generator
$j_{c,SM}$	Inertia constant (H) of the generator
k_{ivg}	SM voltage controller integral gain
k_{pvg}	SM voltage controller propositional gain
k_{qg}	SM reactive power droop gain
l_{lfd}	SM field leakage inductance referred to stator side
l_{lkd}	SM d-axis leakage inductance referred to stator side
l_{lkq}	SM q-axis leakage inductance referred to stator side
l_{ls}	SM stator resistance
l_{md}	SM d-axis magnetizing inductance
l_{mq}	SM q-axis magnetizing inductance
p_{SM}	SM active power
p^*_{SM}	SM active power reference
$p_{p,SM}$	SM number of pole pairs
q_{SM}	SM active power
q^*_{SM}	SM active power reference
q_{mg}	SM low-pass filtered reactive power
r_{fd}	SM field resistance referred to stator side
r_{kd}	SM d-axis resistance referred to stator side
r_{kq}	SM q-axis resistance referred to stator windings

r_s	SM stator resistance
v_d	SM stator d-axis voltage
v_{fd}	SM field d-axis voltage
v_q	SM stator q-axis voltage
k_{ω_g}	SM Frequency control gain
η	VSC load DC voltage controller integral state
c_{dc}	VSC/Twelve-pulse rectifier load capacitance
i_{dc}	VSC/Twelve-pulse rectifier load controlled DC-current source
k_{idc}	VSC load DC voltage controller integral gain
k_{pdc}	VSC load DC voltage controller propositional gain
R_{on}	Twelve-pulse rectifier load diode internal on resistance
V_{df}	Twelve-pulse rectifier load diode forward voltage
l_{p1}	Twelve-pulse rectifier load transformer inductance primary winding
l_{s1}	Twelve-pulse rectifier load transformer inductance secondary winding one
l_{s2}	Twelve-pulse rectifier load transformer inductance secondary winding two
r_{p1}	Twelve-pulse rectifier load transformer resistance primary winding
r_{s1}	Twelve-pulse rectifier load transformer resistance secondary winding one
r_{s2}	Twelve-pulse rectifier load transformer resistance secondary winding two
v_{p1}	Twelve-pulse rectifier load transformer voltage primary winding
v_{s1}	Twelve-pulse rectifier load transformer voltage secondary winding one
v_{s2}	Twelve-pulse rectifier load transformer voltage secondary winding two
Z_h	Constant hotel load impedance
$i_{h,d}$	Constant hotel load d-axis current
$i_{h,q}$	Constant hotel load q-axis current
i_h	Constant hotel load current
l_h	Constant hotel load inductance

p_{dc}	VSC/Twelve-pulse rectifier DC-load
p_h	Constant hotel active load
q_h	Constant hotel reactive load
r_h	Constant hotel load resistance

Acronyms

AC Alternating Current. ii, iii, 2, 5, 7–11, 15, 18, 19, 22, 26, 33, 41, 44, 46, 49–52, 58, 66, 74, 82, 83, 89, 90

AVR Automatic Voltage Regulator. 28, 35, 39, 56, 72, 101

CII Carbon Intensity Indicator. 1

DC Direct Current. 2, 5–9, 15, 17–19, 22, 26, 39, 43, 44, 46, 50, 52, 70, 73, 82, 83, 89, 91

DEM Dynamic Electrical Model. 27, 28

DNV Det Norske Veritas. 5, 51, 53, 54, 66, 67, 70, 72, 73, 76, 78, 86

DP Dynamic Positioning. viii, 11, 12, 50, 82

EEDI Energy Efficiency Design Index. 1

EEXI Energy Efficiency Existing Ship Index. 1

EMC Electromagnetic Compatibility. 51

EMI Electromagnetic Interference. 51

EMS Energy Management System. ii, iii, 15, 49, 50, 69, 74, 76, 78, 80, 83

ESS Energy storage System. i–iii, 2, 4–6, 8–11, 13–15, 17, 27, 29, 49–52, 69, 70, 72–74, 76, 78, 80, 82, 83, 85, 86, 89, 91

GHG Greenhouse Gas. ii, 1, 2, 4–6, 11, 49, 78, 82, 83, 89–91

IEEE Institute of Electrical and Electronics Engineers. 27, 38

IGBT Insulated-gate Bipolar Transistor. viii, 22, 23

IMO International Maritime Organization. 1

L Inductor. 22

LCL Inductor Capacitor Inductor. 22, 24, 29, 30, 56

LNG Liquefied Natural Gas. 78

MVDC Medium voltage direct Current. 7

NTNU Norwegian University of Science and Technology. i

PI Proportional–Integral. 20, 23, 24, 31, 39, 56

PLL Phase Locked Loop. 19–21, 23, 27, 33, 44, 45, 64, 80

PMS Power Management System. 10, 15, 49, 50, 54, 69, 72–74, 76, 78, 80, 83

PSV Platform Supply Vessel. vii, 2–4, 11, 14, 50, 51

PWM Pulse Width Modulation. 22, 24, 26

QSEM Quasi-Stationary Electrical Model. ii, iii, ix, 17, 27–30, 56, 58–60, 62, 63, 90, 91, 101

RMS Root Mean Square. 17

RP Redundant Propulsion. 5

RPS Redundant Propulsion and Separate. 5

SM Synchronous Machine. ii, iii, 9, 19, 27–29, 32–36, 38–42, 50

SOAP State-Of-Available-Power. 83

SRF Synchronous Reference Frame. i, viii, 18–20, 23–26, 29, 44, 90

VSC Voltage Source Converter. i, 17, 22–24, 26–29, 34, 42, 44, 46, 52, 54, 56, 60, 62–64, 66, 70, 72, 74, 80, 90

Chapter 1

Introduction

1.1 Background

The world is facing climate change, and all industries must contribute to reaching the goals of the 2015 Paris Agreement, where participants of UNFCCC agreed to keep the global average temperature well below $2°C$ above pre-industrial levels and pursue efforts to keep it below $1.5°C$ [1]. As a response, regulators and stakeholders in the maritime industry have been intensifying their efforts to cut Greenhouse Gas (GHG) emissions from ships. The International Maritime Organization (IMO), the international regulatory body started an initial strategy of cutting GHG emissions in vessels in 2018 [2]–[5]. IMO intensified this for existing vessels in 2021 with the Energy Efficiency Existing Ship Index (EEXI), used to compare technical energy efficiency between existing ships over 400 gross tons. From 2023, the Carbon Intensity Indicator (CII) will also measure actual operational efficiency in ships over 5000 gross tons. Introducing performance indicators such as Energy Efficiency Design Index (EEDI), EEXI, and CII will make poor performers less attractive in the market and increase demand for improving technical and operational energy efficiency in both new builds and existing ships.

With increased pressure, manufacturers and companies strive to deliver flexible and efficient power systems in ships. These companies constantly search for methods to improve their solutions' compared to their competitors, making them the preferred solution in the market. In the last decade, new hybrid diesel-electric vessels have

shown great potential in their efforts to reduce GHG emissions and operational costs. Full-scale tests and projects have also demonstrated that existing diesel-electric vessels achieve similar results by retrofitting Energy storage System (ESS)s and converting them to hybrid diesel-electric vessels [6]. This increased interest in a retrofit of batteries in existing ships combined with the dual-infeed configuration proposed by Ulstein Design Solutions and BlueCtrl, utilizing a single battery to reduce physical constraints related to GHG installations and increase the flexibility of a two-bus AC-distributed power system formed the basis for this thesis

1.2 Scope

This project will study the control of the power converter interfaces for a single battery installation in a two-bus ship power system and evaluate how the converters can be utilized for supporting the system operation under normal and faulted conditions. The study will be based on analytical considerations and time-domain simulations.

1.3 Report structure

This report starts with a general introduction to marine power systems used in ships. The marine power systems chapter discusses battery integration on a general basis in both AC and DC-distributed power systems and load profiles of a PSV during different operations. The simulation model chapter introduces the mathematical models used to form a complete model of an AC-distributed two-bus hybrid marine ship power system. The discussion/results chapter discusses how the VSM-bases ESS performs during various configurations depending on different operations and failure events of a marine power system. Conclusion/further work includes a conclusion of how the VSM-based ESS performed in ship power systems, limitations related to the simulation model and recommendations for the natural extension of this project.

Chapter 2

Introduction to ship power systems

Traditionally, propulsion systems in ships have been purely mechanical, with prim-mover connected directly to the propeller with gearboxes and axles. Over the last two or three decades have, diesel-electric propulsion systems increased in popularity. Diesel-electric propulsion systems replace mechanical powertrains with electrical powertrains, where generators power electric machines connected to propellers and thrusters. Or alternatively, a combination of mechanical and electric propulsion systems is used with the main propeller driven by a mechanical system and trusters driven by an electrical system. In general mechanical propulsion systems still provide a viable solution for ships, especially ships doing long hauls, and are the preferred choice for containerships, tankers, and other ships used for cross-continental transportation.

Because electric powertrains provide freedom of arrangement superior to mechanical systems, ships requiring a high degree of maneuverability, electric propulsion systems have become the preferred solution [7]. Examples of ships requiring a high degree of maneuverability are PSVs, ferries, icebreakers, tugs, cable layers, and ships with large amounts of special-purpose power, such as self-unloaders, dredges, drilling, and cruise ships. These ships will all benefit from the increased flexibility of electric propulsion that comes from the ability to separate prime movers from thrusters and propellers using electricity to transfer power between power-generating units and loads to improve maneuverability and design. Electrical powertrains also enable multi-power

operation where one or multiple generators provide power to both main propulsion and auxiliary propulsion. One exciting feature of electric propulsion systems is battery-based ESS integration. In the last decade, the number of all-electric, plug-in, and hybrid-electric propulsion systems increased to reduce operational costs and GHG emissions due to decreased battery prices. Hybrid-electric propulsion systems have already proven that PSVs can achieve a 30% reduction in GHG emissions combined with reduced maintenance and fuel costs with appropriate utilization of a battery-based ESS [6], [8]. Full-scale tests have also proven that the same benefits are achievable for existing ships by retrofitting an energy storage system.

However, hybrid-electric propulsion systems do not reduce GHG emissions and operation costs in themself, and pore energy management can indeed result in the opposite. Therefore are, correct sizing of installed battery combined with energy management strategies essential to ensure satisfactory results [9]. The two most significant operations used to reduce operation cost, and GHG emissions with hybrid-electrical propulsion systems are strategic loading of generator sets and providing a "spinning reserve" functionality during critical operations [10]–[12]. Strategic loading of generators maximizes the generator's energy output, compensating for poor performance at low loads by storing energy from generators and using the energy later to support or even operate the propulsion system standalone with generators turned off, reducing the total run time of the generator and increasing efficiency while running. "Spinning reserve" is a concept used in ship operations with high requirements for power reliability, such as DP, cable laying, and crane operations. The "spinning reserve" measures the online energy reserve ready to compensate for changes in power consumption or faults such as generator failure. "Spinning reserve" is typically achieved by running an additional generator synchronized to the grid and dividing the load between the generator set. Systems with excessive requirements for redundancy, such as DP-systems complaint with DPS-2, DYNPOS-AUTR, DPS-3, and DYNPOS-AUTRO, operate with open bus bars and require at least four separate power sources [13]. Operating two or four generators at low loads will increase GHG emissions and operational costs. While this is undesired, is it required to stay compliant with redundancy requirements. Because an ESS meets the requirements as a separate power source, ESS can replace generators used as an emission-free "spinning reserve" and decrease operational costs.

The added functionality of plug-in hybrid diesel-electrical propulsion systems can further reduce GHG emissions and operational costs by replacing or partially replacing the prime mover during transit with energy delivered by an onshore grid. While most harbors have onshore power solutions to cover hotel loads in moored ships, the possibility for onshore chagrining of propulsion systems is limited. However, due to environmental and commercial interest, onshore charging systems are expected to

scale commercially to the point where it delivers environmental benefits [14]. The effectiveness of plug-in hybrid-electric propulsion systems depends on the onshore energy mix and ship operation. For ships with limited possibility of onshore power, will the added plug-in functionality have a limited effect. Conversely, plug-in hybrid ships with good access to onshore power benefit from low energy prices and GHG emissions in onshore grids. Ferries are a great example of a ship that will benefit from a plug-in hybrid-electrical solution. Ferries typically have relatively short transits between terminals and wait during loading/unloading, enabling both all-electric operation and charging during regular operation. During the Norwegian campaign "Klimakur 2030", the Norwegian government decided that all ferries in Norway shall operate with onshore electricity or hydrogen if all electrical operation is unachievable due to technical reasons [15]. According to DNVs, estimates will a change from fossil fuel to mainly electric in ferries reduce GHG emissions between 2021 and 2030 with 1.36 million ton CO_2-equivalents.

2.1 Electrical Propulsion systems

In general, can an electrical propulsion system be divided into two main branches based on how the distribution system works and separated into AC and DC systems. Historically have, AC-distribution systems been the dominating technology for electrical propulsion systems, while usage of DC distribution systems has been steadily increasing recently due to improvements and increased accessibility of power electronics made for DC-distribution systems. Figure 2.1 shows a generic example of a two-bus DC-distributed hybrid ship power system, while figure 2.2 shows an example of an AC-distributed system for comparison. Both represent a Redundant Propulsion (RP) or Redundant Propulsion and Separate (RPS) system [16]. With similar configurations powered by four diesel generators and an onshore power solution when moored. The loads consist of four drives interfacing electrical machines and transformers or converters interfacing sensitive and hotel loads, depending on the system. Two batteries have been added as ESS and can either represent a load while charging or deliver power to support the system.

2.1.1 DC-distributed propulsion power systems

In the DC-distributed power system are, each generator rectified using AC to DC rectifiers and attached to a DC bus enabling variable frequency generators to reduce fuel consumption [10], [12]. Figure 2.1 shows both passive and active rectifiers used to interface generators to the DC bus for illustration purposes. Generator sets with

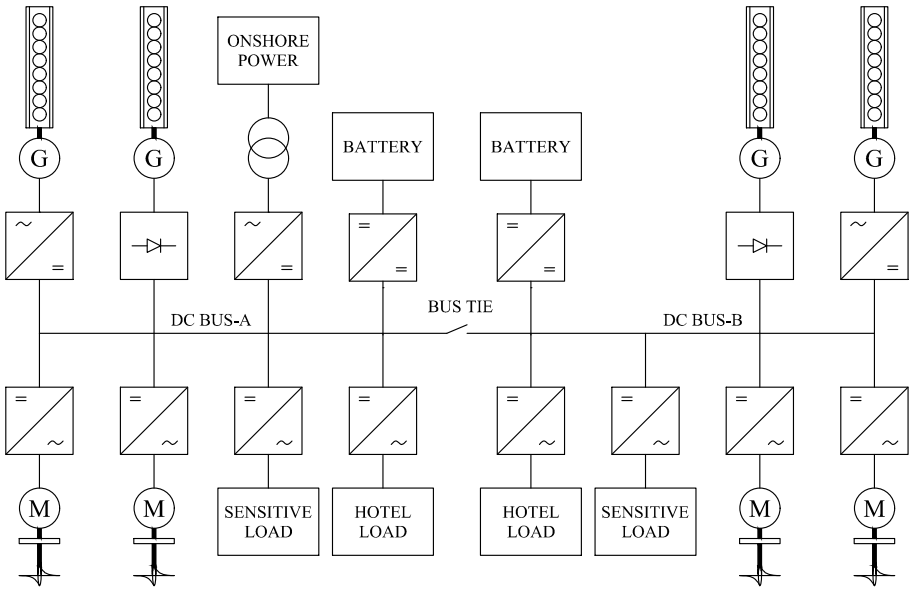

Figure 2.1: Example of a two-bus DC-distributed ship power system

active rectifiers can reduce harmonics, enable power factor correction, and increases generator efficiency in DC systems. Active rectifiers also enable faster regulation and increased control over the DC bus voltage compared to passive solutions. Voltage regulation in DC-distributed power systems with generator sets based on passive rectifiers can face difficulties staying within the maximum voltage variations due to limitations in the dynamic of the diesel generators [17]. These challenges related to voltage stability can increase in systems with variable speed generators at low loads when diesel engines operate at reduced speed to save fuel and GHG emissions.

In DC-distributed power systems without batteries or batteries connected with DC/DC converters, are capacitors used to increase short-term stability and give the DC bus ”inertia” to handle changes in load and transients. Installing a battery-based ESS in DC-distributed power systems can simplify voltage regulation because the ESS can handle fast transients and changes in load by providing an immediate energy reserve in DC systems. One reason for DC systems' popularity in hybrid-electric propulsion is simple battery integration. Depending on the battery capacity and the C-rating, can batteries operate as the DC bus directly because the maximum power delivery/consumption

will never exceed the battery's capabilities. Systems using the battery directly as a DC bus reduce conversions stages and increase overall efficiency. For systems with battery ratings below the generator/load can, high-efficiency DC/DC converters such as buck-boost converts limit maximum power transfer and protect the battery, as shown in figure 2.1.

The loads in DC-distributed systems are connected using variable frequency DC to AC drives, powering electrical machines connected to propellers/thrusters, and constant frequency DC to AC converters power both hotel and sensitive loads. The DC system can also split the A and B-bus in operations with requirements for redundancy in the power supply and required voltage synchronization before reconnecting the bus breaker to limit currents and avoid damaging batteries and other equipment. Spitting a DC bus is challenging because DC-currents have no natural zero-crossing, and breaking DC-currents with traditional switches will cause challenging arcs to extinguish [18]. However, recent reaches and commercialization of DC switches have increased efficiency in MVDC switches and is another reason for the increasing popularity of DC-distribution systems in ships.

2.1.2 AC-distributed propulsion power systems

Figure 2.2 is a two-bus AC-distributed hybrid ship power system designed to be a 1:1 alternative to the DC-distributed power system shown in figure 2.1, with two generators connected in pairs to each AC bus and operated synchronized at a fixed speed. These ship power systems are typically designed with one generator larger than the other to improve efficiency by matching the correct-sized generator to the current load situation. Like the DC system, the bus tie can split the A and B-bus during operations with requirements for redundancy in the power supply. Braking currents in AC systems are done with traditional switches, as the next zero crossing will extinguish any arcs occurring. Reconnecting AC systems require voltage and frequency synchronization between the A and B-bus before closing the bus tie to avoid damage to the system. The last energy source of the system is the onshore power interfaced with a transformer and requires synchronization before the ship is connected. This transformer then matches the bus voltage to the onshore grid voltage, providing a galvanic barrier between the ship power system and the onshore power system. However, if the nominal frequency of the ship differs from the onshore grid, the only solution is an AC to AC power converter.

The electrical machines connected to propellers and thrusters are interfaced to the grid with variable frequency AC to AC drives controlling the output speed and torque of electrical machines. For illustration purposes, figure 2.2 includes drives with active

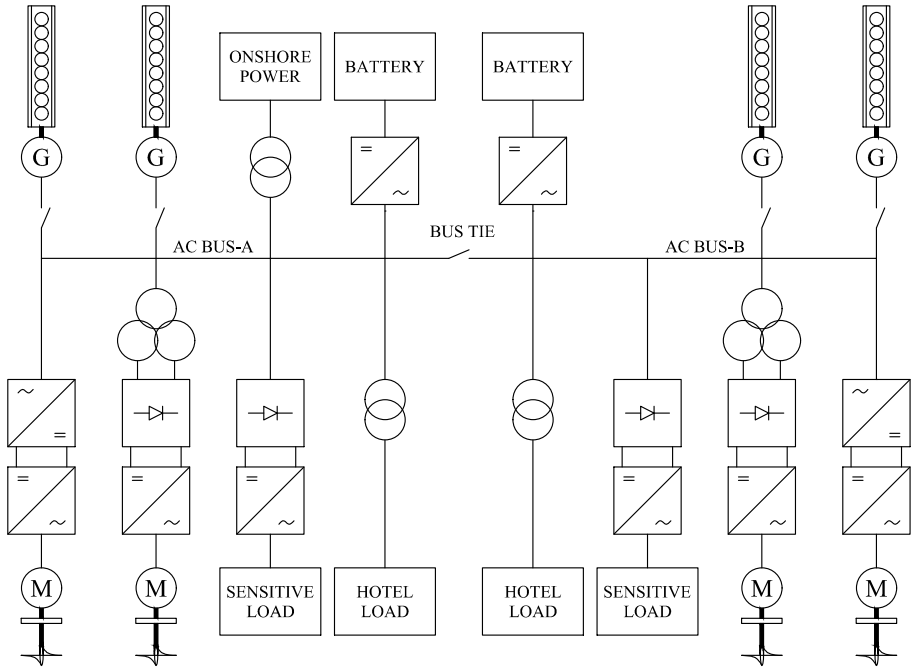

Figure 2.2: Example of a two-bus AC-distributed ship power system

and passive front-ends discussed further in chapter 3.5. Other loads, such as hotel and sensitive loads, are typically connected with transformers or AC to AC converters and used to transform the bus voltage, typically from 690VAC to a standard voltage level used in consumer electronics and equipment typically rated at 400VAC/240VAC. Ship power systems also contain control, navigation, and communication electronics sensitive to noise and power interruptions, typically connected using low-noise UPS systems.

The battery-based ESS solution relay on grid-forming or traditionally grid-following DC to AC converters to interface the battery in AC-distributed power systems [19]. While the grid-following power converter represents tried and tested solution, it has some significant disadvantages compared to DC systems. Because grid-following AC/DC converters rely on a stable grid to synchronize against, they will always require at least one running generator to form a grid and prohibit islanded operation

of the ESS. Unless the control structure can change from grid-following to a fixed frequency, requiring either a blackout of the grid or a time-critical changeover between multi-power and islanded operation of the converter. Furthermore, grid-following AC/DC converters do not contribute to the overall grid inertia related to the short-term frequency stability of the grid discussed in chapter 2.2. A possible solution that enables seamless transitions between multi-power and islanded operation and sustains grid inertia in AC-distribution systems is a grid-forming VSM-based ESS, presented in chapter 3.3. VSM-based converters are an emerging technology and have been researched heavily over the last decades due to their contribution to grid inertia in onshore power grids. Moreover, the VMS-based ESS presents a flexible control structure of the AC/DC converter, enabling seamless transitions between multi-power and islanded operations without any changes to the control system.

2.2 Frequency stability in AC-distribution power systems

The overall power balance in AC-distribution systems determines the grid frequency, and any power imbalance between generating and consuming units will increase or decrease the grid frequency [20]–[22]. Frequency control in AC-distributed ship power systems consists of an immediate inertia response combined with primary control systems. Primary control, also known as "Governor" control, is used to control the mechanical power output of the prime mover electrically connected to the grid through an SM. The governor ensures local power balance by increasing the mechanical power output of the prime mover if the grid frequency decreases or decreasing mechanical power output if the grid frequency increases compared to the nominal system frequency. AC-distributed ship power systems typically use PMS as secondary control systems to manage the overall power balance by adjusting the power reference for each power generating unit. The PMS can also be combined with an EMS to ensure optimal utilization of the power generation units using preplanned trips or optimization algorithms [11].

However, the primary and secondary control systems are relatively slow, and the system inertia determines the immediate frequency response to disturbance or changes in power balance. Because of this, system inertia is considered one of the most vital system parameters of AC-distributed power systems as it relates to the short-term stability of these systems [20]. System inertia comes from the moment of inertia, describing the resistance to change in angular speed of electrical and mechanical machines. Increasing or decreasing this kinetic energy E_{gen} (2.1) requires positive or

negative torque, and the momentum of inertia J_{gen} quantifies this torque needed to increase the angular frequency ω_{gen} of these machines. In electrical power systems, engineers replace the moment of inertia with the inertia constant H_{gen}, which describes the relationship between the stored kinetic energy E_{gen} and the power rating S_{gen} at nominal speed (2.2) of power-generating machinery. To quantify the immediate energy reserve of generators or the entire system.

$$E_{gen} = \frac{1}{2} J_{gen} \omega_{gen}^2 \tag{2.1}$$

$$H_{gen} = \frac{E_{gen}}{S_{gen}} \tag{2.2}$$

The total system inertia H_{sys} describes the relationship between stored kinetic energy in the system and the total system power rating S_{sys}. Derived by the weighted average of each power generating unit or rotating machinery (2.3).

$$H_{sys} = \sum_i \frac{H_{gen,i} \cdot S_{gen,i}}{S_{sys}} \tag{2.3}$$

In AC-distributed ship power systems, inertia is provided by the mechanical rotation of generators or constantly rotating electrical machines electrically connected to the grid. An introduction of a grid following ESS in these systems will increase the total system power rating without contributing to the overall system inertia and, therefore, decrease the total system inertia H_{sys}. Because the goal of adding an ESS is to replace generators, will this also further decrease the total system inertia and affect the grid's short-term stability

Ship power systems typically compensate for low inertia, with load management systems limiting large consumers depending on the total available power to prevent instabilities or blackouts. Load management is typically handled by the PMS, limiting the rate of change in significant consumers, such as main propellers/thrusters. While this delay in thrust provided a solution to low inertia in AC grids, is this unacceptable during critical and requires an increased "spinning" reserve to enable instant thrust.

2.3 Typical load variations in ship power systems

The project received a data set containing information about the entire power system of a PSV sampled between 11. December 2021 and 11. January 2022 from BlueControl [23]. A PSV is a multipurpose vessel used for various operations, such as DP, craning, winching, and pumping, with highly dynamic load profiles [11]. Table 2.1 shows the configuration of the power systems. Where bus-A consists of two generators, $G1$, and $G2$, powering one main propeller $MP1$ and one thruster. Bus-B consists of two generators, $G3$, and $G4$, a second main propeller $MP2$ and a second thruster. This data set has provided information used in chapter 4 to analyze the effects of adding a VSM-based ESS in an AC-distributed two-bus power system and providing insight into typical operations load variations seen by the generators during DP operation with open bus tie, transit with closed bus tie, and moored PSVs.

Table 2.1: PSV configuration

Component	Rating
Generator $G1$ and $G4$	$2359kVA$
Generator $G2$ and $G3$	$994kVA$
Main propeller $MP1$ and $MP2$	$2200kVA$
Bow thruster and retractable bow thruster	$800kVA$

2.3.1 Load variations during critical operation (open bus tie)

During DP operation, presented in figure 2.3, all generators operated as a spinning reserve with an open bus tie to ensure power reliability and stability. However, the load is dynamic, with a low average load at only 10.1% and 8.6% of rated capacity for buses A and B, respectively, and leads to poor fuel economy and high GHG emissions from four generators operating with poor efficiency. Replacing generators $G1$ and $G4$ as a spinning reserve with an ESS will reduce operational costs and GHG emissions. The remaining generators will also have an increased load, with generator $G2$ averaging at 34.1% load and generator $G3$ at 28.9%. Using a virtually closed bus discussed in chapter 2.4 enables less critical DP operations to operate with a single generator, and for example, $G2$ will average at 63.0% load. At the same time, the grid-forming ESS operates as a spinning reserve for generator $G2$ on bus-A. It operates bus-B islanded, reducing the number of running generators from four to possibly one. This generator reduction using a virtually closed bus further reduces operational costs and GHG emissions during some DP operations.

Studying the data set reveals that the most significant step in load occurs at 13:39, where the load changes from 9.5% to 38.8%, resulting in a 30% change in load. Because DP operations require instant thrust, power systems in ships must handle sudden steps like this while maintaining grid voltage and frequency.

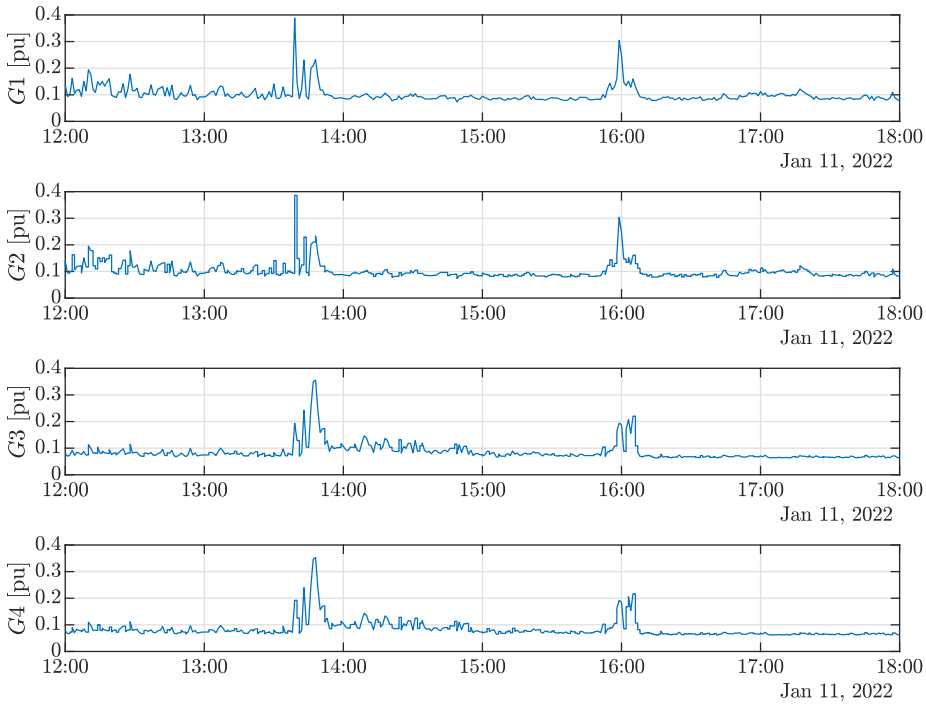

Figure 2.3: Power delivered form each generator during DP

2.3.2 Load variations during transit (closed bus tie)

During transit, the bus tie is closed, and generator sets are operated depending on the current load given by the wind, underwater streams, and speed of the ship. Figure 2.4 shows a six-hour window of transit between sites. During this transit are, the load generally high, with slight variation leaving the generators $G1$ and $G2$ at 60% load, leaving little room for energy optimization with an ESS. However, short transits may be appropriate for all-electric operations with a grid-forming ESS using stored onshore power.

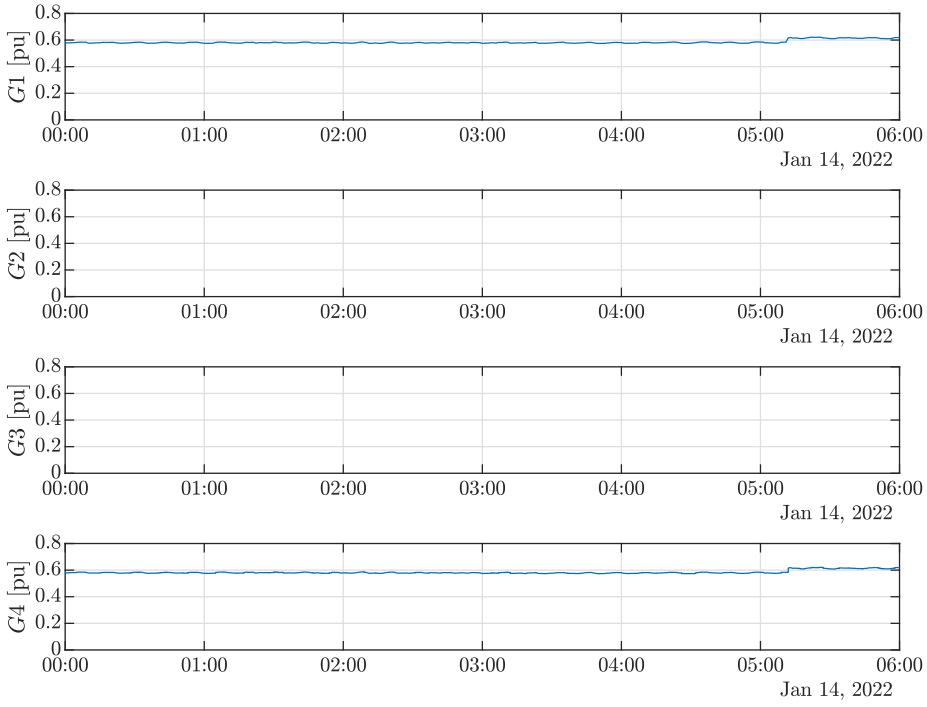

Figure 2.4: Power delivered form each generator during transit

2.3.3 Load variations in moored ships

The moored PSV operates with the bus tie open, running a single generator, $G2$. Figure 2.5 shows a six-hour window of the moored PSV where the power system sustains a hotel load, with a low load at a 22.6% average and only slight variations in load. The preferred solution in moored ships is replacing the generator with onshore power to sustain hotel loads. Another solution is to run the generator at a higher load charging the ESS during transit and using the grid-forming ESS to sustain hotel loads islanded while moored. Using the ESS solution has higher operating costs because it still depends on diesel as it is the primary energy source and has some losses related to charging and discharging the battery compared to an onshore solution. Also, in ships with high hotel loads compared to the battery capacity, will cycling the battery introduces wear, which may reduce battery life to the point where this is not beneficial, depending on the discharge rates.

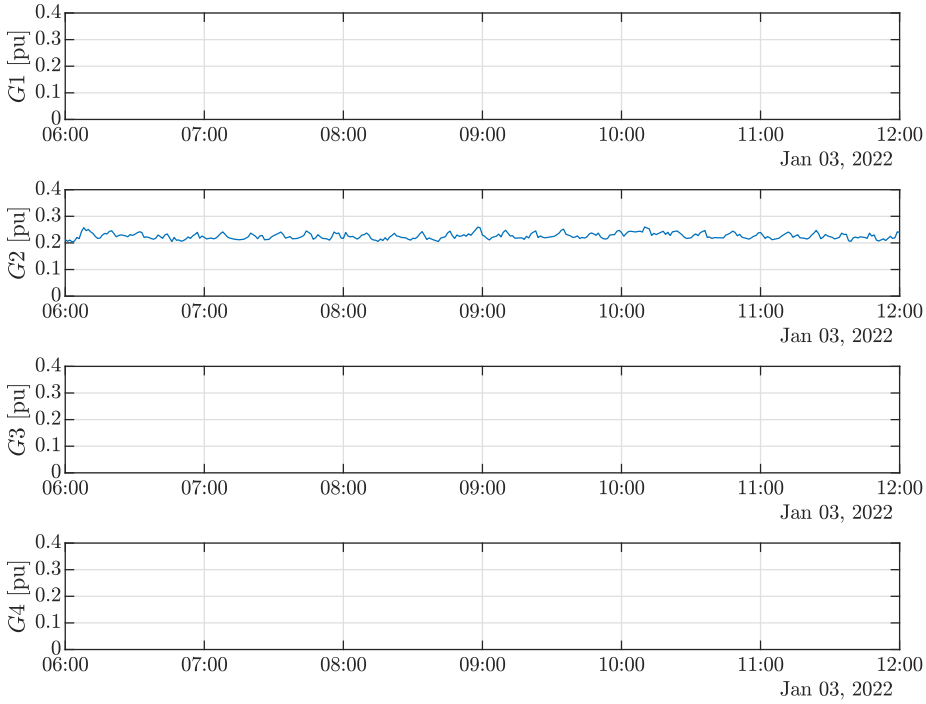

Figure 2.5: Power delivered form each generator moored

2.4 Dual-infeed ESS in ship power systems

Converting traditional diesel-electric ships with AC-distributed power systems to hybrid solutions can be achieved by retrofitting a battery-based ESS. Figure 2.6 shows a proposed solution for single battery installation in a two-bus AC-distributed power system, based on the dual-infeed solution using a common DC bus and two VSM-based converters interface between the DC bus and each AC bus. Depending on battery and converter ratings, the DC bus can either have a battery connected with a DC/DC converter for protection or a battery connected directly to the DC bus if the VSMs are limited or below the capacity and C-rating of the battery. This dual-infeed solution with a grid forming ESS and common DC bus also enables operation with a ”virtual” closed bus. A ”Virtual” closed bus can be beneficial in situations with high requirements for power reliability as this method can use the VSM-based ESS to cycle energy between the A and B-bus in operations with open bus ties. This ”Virtual” closed bus enables the PMS/EMS to reduce the number of running generators by matching any configuration of generators from four to one depending on the load as if the system operated with closed bus ties during operations with a split bus to prevent failures from affecting the entire system. A single battery installation can also overcome physical constraints regarding available space in retrofits.

In ships operating with short transits and reasonable access to onshore power, are plug-in hybrid solutions typically desired. Suppose these ships already have a solution for onshore power with extra capacity. In that case, it may be suitable for charging depending on the available capacity or modified to increase capacity and achieve satisfactory charging speeds. Alternatively, can installing a similar solution used in two-bus DC-distributed hybrid ship power systems, as shown in figure 2.1, be a better option.

Because the dual-infeed solution represents a flexible and exciting alternative for retrofits, will a reduced version of this dual-infeed solution shown in figure 2.6 form the basis for the simulation model and the following discussions.

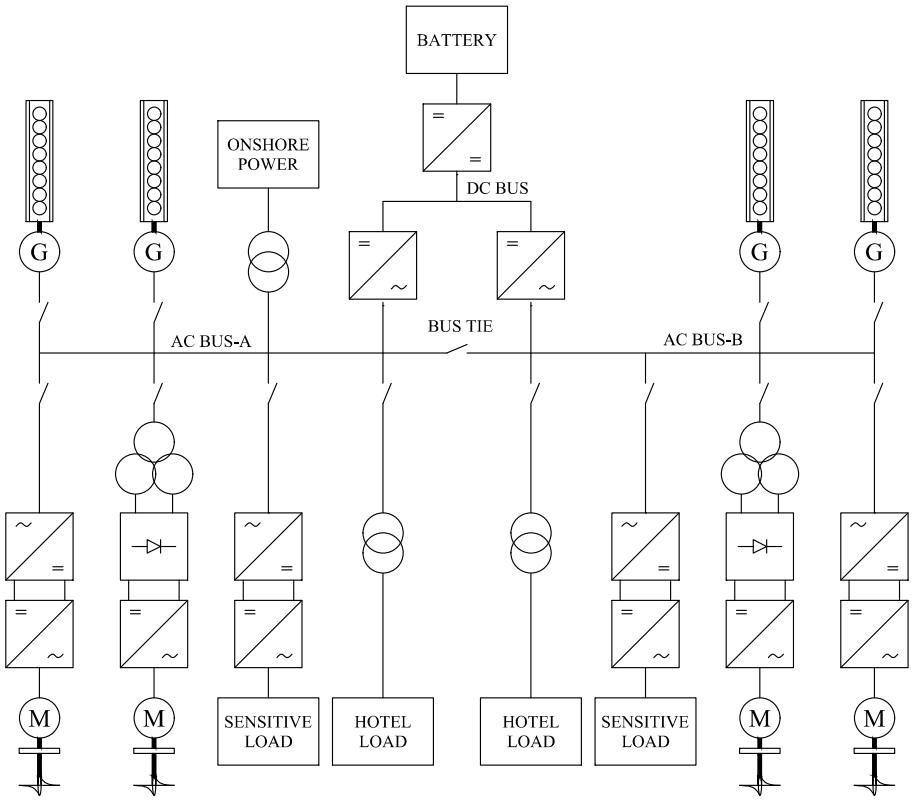

Figure 2.6: Proposed solution of single battery integration in two-bus AC-distributed ship power system

Chapter 3

System modeling

This chapter presents the simulation used to verify the effects of adding a dual-infeed VSM-based ESS in a ship power system. Figure 3.1 shows an overview of the simulation model that includes six load models and two diesel generators as in traditional diesel-electric ship power systems. The dual-infeed ESS solution uses two VSM-controlled VSC connected to an ideal DC-power source. This ideal DC source represents an ideal battery or a regulated DC bus. The A and B-bus are identical, and the bus tie enables simulation of operations requiring rps for safety reasons.

Table 3.1 presents the system ratings of the simulation model designed as a medium-sized marine ship power system. Each power-producing unit is rated at 1 MVA with a combined output of 4 MVA and a line-to-line voltage $V_{LL,RMS}$ at 690V RMS. The nominal frequency f_b of $50Hz$ is a design decision based on the available literature about the QSEM-based VSM used in the VSM-based ESS. The system frequency is not expected to affect the simulation results in this report, while changing the base frequency may require some tuning.

The simulation model is designed in Matlab® and uses Simulink® for control systems, while Simscape™ represents the physical part of the model. A copy of the simulation model will be available on Github, Inc. [24].

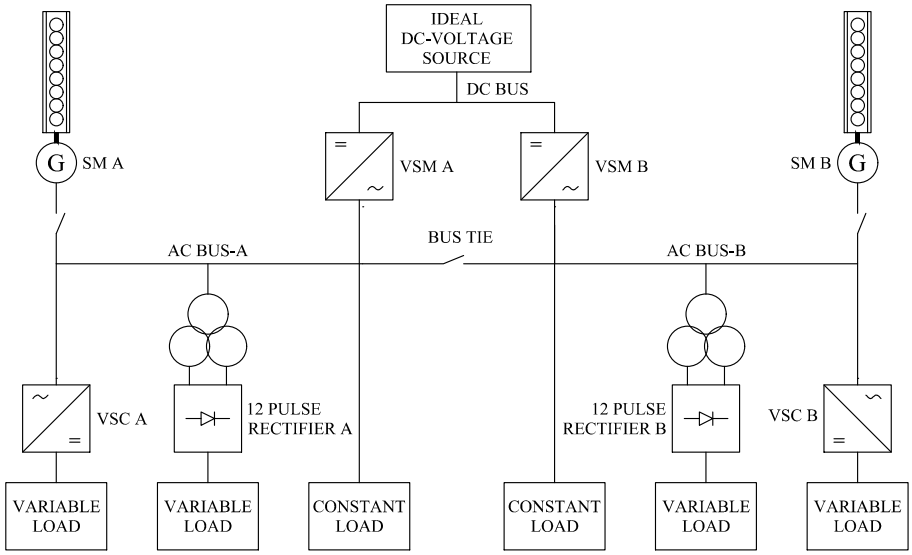

Figure 3.1: Overview of simulation model

3.1 Per-unit representation and SRF orientation

The control structure of the simulation model uses a per-unit system. The per-unit system ensures that all values are relative to the system base ratings [25], [26]. This report denotes all per-unit values with lowercase, while physical values are uppercase. Table 3.1 lists the base values used to form the per-unit system. The base voltage V_b is the phase voltage referred to zero in the AC-grid, and the battery voltage or DC base voltage $V_{b,dc}$ is two times V_b same as the peak-to-peak phase voltage. The base current I_b is the current phase amplitude referred to zero at nominal load. Similar to base current is the apparent power S_b phase amplitude referred to zero at nominal load. The base angular velocity ω_b is the rated system frequency given in radians per second. Finally, the base resistance R_b is determined by ohm's law and calculated using V_b and I_b. The base inductance is calculated by dividing R_b by ω_b and base capacitance by dividing one with both R_b and ω_b.

The control system uses an amplitude invariant park transformation (3.1) to map the three-phase voltage or current measurement into a complex space vector in a Synchronous Reference Frame (SRF) [27], [28]. The selected base values combined with

Table 3.1: System ratings and per-unit base values

Parameter	Value
Rated system voltage, $V_{LL,RMS}$	$690\,V$
Rated system frequency, f_b	$50\,Hz$
Rated apparent power, $S_b = \frac{3}{2} V_b I_b$	1 MVA
Base AC-voltage, $V_b = \frac{\sqrt{2}}{\sqrt{3}} V_{LL,RMS}$	$563.38\,V$
Base DC-voltage, $V_{b,dc} = 2V_b$	$1126.76\,V$
Base current, $I_b = \frac{2S_b}{3V_b}$	$1775.00\,A$
Base resistance, $R_b = \frac{V_b}{I_b}$	$0.032\,\Omega$
Base inductance, $L_b = \frac{R_b}{\omega_b}$	$0.001\,\Omega \frac{rad}{s}^{-1}$
Base capacitance, $C_b = \frac{1}{R_b \omega_b}$	$0.010\,\Omega^{-1} \frac{rad}{s}^{-1}$
Base angular velocity, $\omega_b = 2\pi f_b$	$314.16\,\frac{rad}{s}$

an amplitude invariant park transformation (3.1) enable active and reactive power to be calculated directly in the dq-reference frame. Figure 3.2 illustrates the SRF orientation, where x represents either voltages or currents in the rotating dq-reference frame synchronized to the angular velocity ω of the measurement. The angular velocity used to synchronize the dq-reference frame is determined by directly measuring the rotor speed in an SM or the virtual rotor speed in a VSM. Alternately, a PLL's is used to lock the dq-reference frame to the measurement. In figure 3.2, θ describes the angle between the stationary $\alpha\beta$-frame and the rotating dq-reference frame, while phase angle δ describes the position of x inside the dq-reference frame. The complex space vector x is decomposed into a real component x_d and an imaginary component x_q, and x_0 will always equal zero for balanced systems. The voltage or current vector x in dq can always be mapped back into the three-phase signal x_a, x_b, and x_c using the inverse park transformation (3.2).

$$\begin{bmatrix} x_d \\ x_q \\ x_0 \end{bmatrix} = \frac{2}{3} \begin{bmatrix} \cos\theta & \cos(\theta - \frac{2\pi}{3}) & \cos(\theta + \frac{2\pi}{3}) \\ -\sin\theta & -\sin(\theta - \frac{2\pi}{3}) & -\sin(\theta + \frac{2\pi}{3}) \\ \frac{1}{2} & \frac{1}{2} & \frac{1}{2} \end{bmatrix} \begin{bmatrix} x_a \\ x_b \\ x_c \end{bmatrix} \tag{3.1}$$

$$\begin{bmatrix} x_a \\ x_b \\ x_c \end{bmatrix} = \begin{bmatrix} \cos\theta & -\sin\theta & 1 \\ \cos(\theta - \frac{2\pi}{3}) & -\sin(\theta - \frac{2\pi}{3}) & 1 \\ \cos(\theta + \frac{2\pi}{3}) & -\sin(\theta + \frac{2\pi}{3}) & 1 \end{bmatrix} \begin{bmatrix} x_d \\ x_q \\ x_0 \end{bmatrix} \tag{3.2}$$

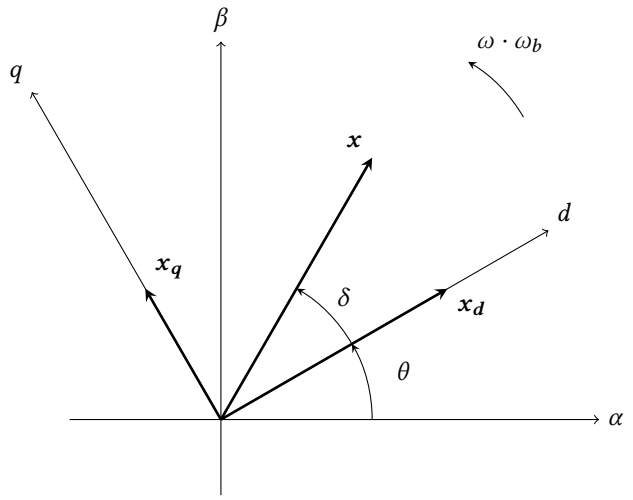

Figure 3.2: Vector diagram defining the SRF, voltage and current vector orientation

3.1.1 Phase locked loop

The PLL is used to lock the dq-reference frame to a measured three-phase signal x_{abc} using a PI-controller and gives a perfect decoupling between the d and q-axis of the measurements stationary [29], [30]. The PLL works by calculating x_d and x_q, then calculating and regulating the phase angle δ towards zero aligning x_d with the d-axis of the dq-reference frame. PLLs can, therefore, measure the grid frequency and enable grid synchronization. Figure 3.3 shows a PLL architecture. Low-pass filters (3.3) were added to the measurements $x_{f,d}$ and $x_{f,q}$ used in the PLL feedback to prevent harmonics and noise from being transferred back into the system. ω_f sets the low-pass filters crossover frequency, and the feed-forward f_b is the rated system frequency.

$$\frac{d}{dt}x_{f,d} = \omega_{f,PLL}x_d - \omega_{f,PLL}x_{d,f} \tag{3.3a}$$

$$\frac{d}{dt}x_{f,q} = \omega_{f,PLL}x_q - \omega_{f,PLL}x_{q,f} \tag{3.3b}$$

To achieve the desired response of the PLL controller, the propositional constant $k_{p\delta}$ and integral constant $k_{i\delta}$ of the PI-controller can be adjusted. The tuning method

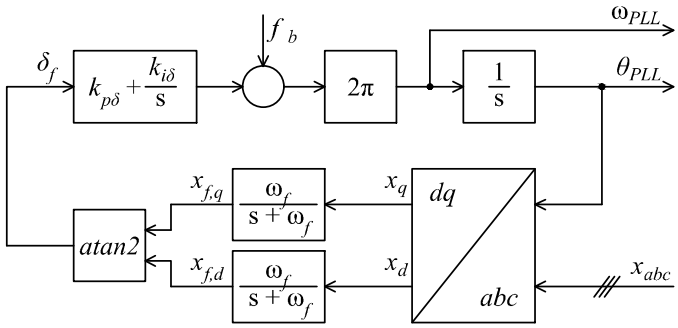

Figure 3.3: Phase locked loop

symmetric optimum (3.4) maximizes the phase margin of the PLL, resulting in a robust tuning decreasing sensitivity towards delays and input disturbances. ω_f is typical in the range 10 to 1000Hz and the tuning parameter a in the range 2 to 10 where values less the three will give complex conjugated roots, values equal to three will result in real and equal poles and for values over three will give real and distinct poles [30]. A thorough introduction of the symmetric optimum tuning method can be found in the specialization project [31]. Finally, table 3.2 lists all tuning parameters of the PLL.

$$k_{p\delta} = \frac{\omega_f}{a2\pi} \tag{3.4a}$$

$$k_{i\delta} = \frac{a^2}{\omega_f} \tag{3.4b}$$

Table 3.2: Parameters phase locked loop

Parameter	Value
PLL tuning parameter, a	3
PLL damping filter, ω_f	100 Hz
PLL propositional gain, $k_{p\delta}$	5.31
PLL integral gain, $k_{i\delta}$	0.09

3.2 Voltage source converter model (inner loop)

VSCs convert DC voltage (V_{DC}) to AC voltage (V_{AC}) or the other way around in power applications [29], [30]. Figure 3.4 shows a three-phase IGBT bridge used for voltage conversion by the VSM and VSC load model. The VSC uses a current controller to control the currents flowing through the IGBT bridge. The specialization project leading up to this master thesis presented the VSC and the belonging control structure used in this report [31]. In short, the VSC consists of six IGBTs denoted G_x connected in a three-phase bridge configuration controlled using PWM. A low-pass LCL filter is added to the VSC to remove the PWM carrier frequency and sideband harmonics. The VSC uses a third-order LCL filter, commonly used in the industry due to an increased attenuation ratio compared to an L filter. LCL filters can achieve 60db/decade attenuation compared to 20db/decade attenuation in first-order L filters [32]. The increased order of LCL filters causes issues with resonance frequencies. LCL filters require, therefore, passive or active damping to prevent instability and harmful voltages/currents occurring in the grid due to low impedance at the crossover frequency. Because passive damping of the LCL filters will lead to increased energy loss, an active damping of LCL filters is the preferred solution, especially for high-power VSC. An LCL filter consists of two inductors in series with each phase and a filter capacitors C_f between phase a, b and c. This project has used two equal inductors with an inductance L_f and an equivalent series resistance R_{lf} representing the resistive loss occurring in the inductor. Table 3.3 lists all parameters used in the VSC simulation model.

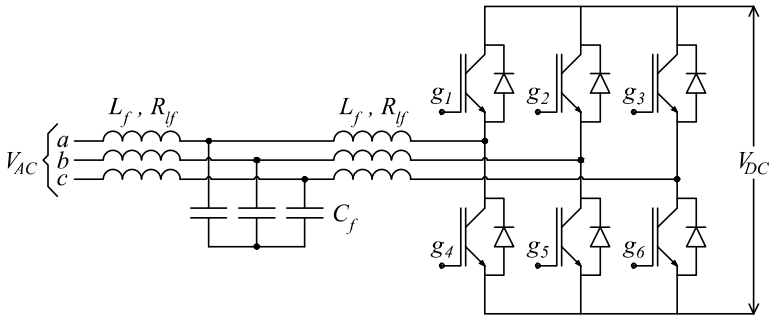

Figure 3.4: *LCL*-filter and three phase IGBT bridge

Table 3.3: Parameters voltage source converter model

Parameter	Value
LCL-filter resistance, r_{lf}	$0.003\,pu$
LCL-filter inductance, l_f	$0.080\,pu$
LCL-filter capacitance, c_f	$0.074\,pu$
Propositional gain, k_{pc}	1.27
Integral gain, k_{ic}	15
Feedforward filter voltage, k_{ffv}	0
Active damping gain, k_{ad}	1.5
Active damping crossover frequency, ω_{ad}	$50\,\frac{Rad}{s}$

3.2.1 SRF current controller

The SRF current controller architecture is shown in figure 3.5 and controls the desired voltage v_c^* of the IGBT bridge [29]–[31], [33]–[36]. The SRF current controller is synchronized to the grid using the PLL presented in chapter 3.1.1, and based on the understanding of the filter inductor used to filter out the switching noise introduced by the IGBT bridge. A model of the filter inductor is determined using Kirchhoff's second law applied in the $\alpha\beta$ frame and then transferred into the SRF (3.5).

$$v_c = v_{AC} + r_{lf} i_c + \frac{l_f}{\omega_{VSC}} \frac{d}{dt}(i_c) + j\omega_{VSC} l_f i_c \tag{3.5}$$

The SRF current controller then combines two conventional PI controllers and a feedforward term to decouple the cross-coupling occurring in the filter inductor (3.5), resulting in individual control over active and reactive currents in the VSC. The state-space model of the SRF current controller (3.6) shows the relationship between the desired converter current i_c* and the desired converter voltage v_c* used to control the modulation index of the VSC model. The propositional gain k_{pc} acts on the error between the desired and actual converter current i_c. While the integral gain k_{ic} acts on the integral state γ. The feedforward term used for decoupling is the product of the per-unit filter inductance l_f, the measured angular velocity of the grid, and the actual converter current.

$$v_c^* = k_{pc}(i_c^* - i_c) + k_{ic} * \gamma + jl_f\omega i_c - v_{ad}^* + k_{kff}v_f \tag{3.6a}$$

$$\frac{d}{dt}\gamma = i_c^* - i_c \tag{3.6b}$$

The most significant contribution to delay in a VSC is the PWM modulation typically modeled with a linear delay approximation in the tuning process of the SRF current controller, resulting in a low order system "without" time delays suitable for modulus optimum (3.7) [29]. Modules optimum uses pole cancellation and ensures that the time constant of the PI-controller is equal to the time constant of the LCL filter. An analytical approach uses physical parameters given by the LCL filter and the linear delay approximation T_{sum} to derive the proportional and integral gain. The filter inductance l_f, T_{sum}, and ω_b give the proportional gain k_{pc} (3.7a). While the integral gain k_{ic} is given by the internal resistance r_{lf} of the inductor and T_{sum} (3.7b).

$$k_{pc} = \frac{l_f}{2\omega_b T_{sum}} \tag{3.7a}$$

$$k_{ic} = \frac{r_{lf}}{2T_{sum}} \tag{3.7b}$$

The SRF current controller shown in figure 3.5 includes a feedforward of the filter capacitor voltage adjusted by the k_{ffv} gain and a control strategy for active damping (3.7) of the LCL filter oscillations using a high-pass filter to subtract undesired osculations and harmonics from v_c^* [33]. The high-pass filter is implemented using a low-pass filter φ with crossover frequency ω_{ad} (3.8b) subtracted from the actual measurement v_f leaving undesired oscillations and harmonics. Finally, are these subtracted from the desired converter voltage v_c* based on the active dampening gain k_{ad}.

$$v_{ad}^* = k_{ad}(\varphi - v_f) \tag{3.8a}$$

$$\frac{d}{dt}\varphi = \omega_{ad}v_f - \omega_{ad}\varphi \tag{3.8b}$$

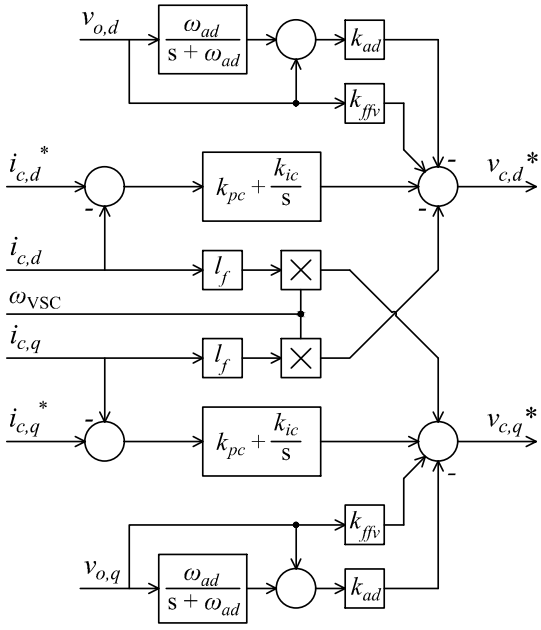

Figure 3.5: SRF current controller with active damping of filter oscillations

3.2.2 Modulation index and third harmonic injection

The VSC model uses an ”average model-based VSC” to overcome issues related to PWM simulation in Simulink® and Simscap™. Precise simulation of PWM signals in Simulink® and Simscape™ requires much smaller increments in the numerical integrator than the PWM carrier frequency. While this is acceptable when simulating fast transients, it will make the model slow during longer simulations with large time constants. Because the simulation model uses an average model of the VSC, the modulation index in the $\alpha\beta$ frame m_{abs} is determined directly using the inverse park transformation (3.2) on m in the dq frame. The modulation index (3.9) m is compensated for DC-voltage deviations by dividing desired converter voltage v_c^* by the DC bus voltage v_{dc} [37]. Because the modulation index is DC-voltage compensated can, the VSC be operated without a regulated DC bus, as this efficiently decouples the AC and DC bus. However, the DC bus can only be left unregulated if the battery is large enough to handle the maximum energy delivered or consumed by the VSC.

$$m = \frac{v_c^*}{v_{dc}} \tag{3.9}$$

A third harmonic component is injected into the first harmonic modulation index m_{abc} to increase the linear relationship between the line-to-line voltage and the modulation index by 115% [37]. A third harmonic injection means that the modulation index can be driven beyond 1.0 to 1.15 before entering over-modulation, increasing energy flow through VSC. Because the third harmonic is a common-mode voltage introduced in all phases of the system, will this third harmonic voltage disappear line-to-line in AC systems with floating neutral. The third harmonic component m_3 (3.10), is equal for all the phases and has an amplitude equal to 1/6 of m. The angular position of m_3 is aligned with m using the angular position of m in the SRF.

$$m_3 = -\frac{|m|}{6} \cos\left(3 * \left(\theta + \arctan\frac{m_q}{m_d}\right)\right) \tag{3.10}$$

3.3 Virtual synchronous machine model

In 2007 [38] presented a concept called VISMA. VISMA combined, for the first time, dynamical power electronic converters with static and dynamic properties of the electromechanical synchronous machine in one single unit, commonly known as the VSM. This way, the VSMs inherit and maintain essential electromechanical properties of the SM [33], [39]–[42]. Maintaining these electromechanical properties of SMs in power electronic converters is essential to ensure grid stability as the future of energy production moves away from centralized power production to distributed power generation with an increased level of electric power transferred with power electronic converters. In ships, the power systems are essentially microgrids, where any change in energy production quickly affects grid stability. Implementing a grid following ESS in a ship power system with PLL-controlled VSCs will increase electric energy transfer without contributing to grid stability, forcing the system to operate generators as a spinning reserve to ensure grid stability. By changing to a grid-forming VSM-controlled ESS, the ESS will contribute to grid inertia and eliminate the need for generators operated as spinning reserves. Ship power systems can also benefit from the VSM's ability to operate islanded or in multi-power grids without changing the control structure.

Because the VSM concept aims to emulate a real SM by controlling a power electronic converter, any implementation of a VSM contains a mathematical model of an SM. However, the development of the VSM has been more an arbitrary design choice than physical requirements, affecting the level of detail between different implementations of VSMs. Systems requiring an accurate emulation of an SM require a 5^{th} order electrical model with a detailed *dq*-representation of stator windings, damper windings, and field windings of the SM. To fully describe the SM's mechanical and electrical properties, the VSM increases to a 7^{th} order model combining the 5^{th} order electrical model with a 2^{nd} order mechanical model, also known as the swing equation. Some VSMs operate with a reduced-order electrical model by omitting some dynamical behaviors of the SM, such as the 2^{nd} order Dynamic Electrical Model (DEM) or Quasi-Stationary Electrical Model (QSEM), resulting in a 4^{th} order model when combined with the second-order mechanical model.

The two main categories of VSM-controlled VSCs, depend on whether the VSC is voltage or current vector referenced [43]. VSMs based on the current vector referenced VSC omits cascaded voltage controllers typically associated with voltage referenced VSCs and reduces the complexity of the VSC. Two examples of current vector referenced VSM models are the DEM and QSEM. The IEEE article [33] has compared the DEM and QSEM architecture and found that QSEM is preferable over the DEM

architecture. Although the DEM emulates some of the SM's dynamical properties, this leads to an increased amount of undesired oscillations compared to the QSEM architecture. The QSEM can also increase decoupling between active and reactive power due to reduced stator resistance compared to the DEM. Based on the findings in [33] the QSEM was chosen as the preferred solution forward in this thesis.

The following chapters give a detailed description of the QSEM-based VSM, and figure 3.6 provides an overview of the VSM-controlled VSC used in the simulation model. The inner loop of the QSEM-based VSM consists of the current controlled VSC presented in chapter 3.2. The outer control loops of the QSEM-based VSM are developed in the same manner as an SM, with a voltage controller, also known as AVR, and a frequency controller, known as the governor. Table 3.4 lists the final tuning of the VSM model in the final simulation model.

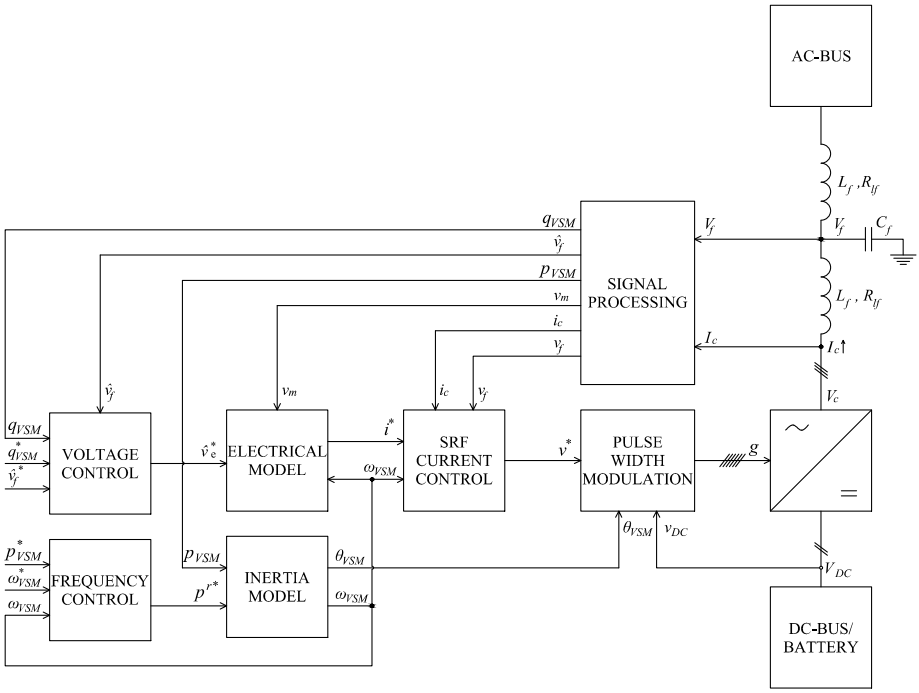

Figure 3.6: Overview of virtual synchronous machine implementation adopted from [33]

Table 3.4: Parameters virtual synchronous machine model

Parameter	Value
Virtual stator resistance, r_{vs}	$0.01\,pu$
Virtual stator inductance, l_{vs}	$0.25\,pu$
VSM LCL-filter voltage low-pass filter crossover frequency, ω_{vf}	$200\,\frac{Rad}{s}$
Reactive power droop gain, k_q	0.1
Reactive power filter crossover frequency, ω_{qf}	$200\,\frac{Rad}{s}$
Voltage controller propositional gain, k_{pv}	0.29
Voltage controller integral gain, k_{iv}	92
Inertia time constant, T_a	$4\,s$
Damping coefficient, k_d	40
Damping filter, ω_d	$5\,\frac{Rad}{s}$
Frequency control gain, k_ω	20

3.3.1 Quasi-stationary electrical model

The VSM-based ESS used in this report uses a quasi-stationary algebraic SRF representation of the stator impedance shown in figure 3.7 [33]. The QSEM reduces the complexity of the VSM by omitting the dynamic, transient, and sub-transient behaviors of the SM model and reduces the electrical model from a 5^{th} order to a pure algebraic model. The VSM uses the quasi-stationary stator current i_{vs} to control the VSC by setting the current reference i^* equal to i_{vs}. The stator current i_{vs} are determined by the voltage difference between the controlled voltage source (field voltage) $\hat{v}_e^*$ and the LCL filter voltage V_f divided by the stator impedance (3.11). The stator impedance consists of the virtual stator resistance r_{vs} and the virtual stator inductance l_{vs} related to the per-unit angular velocity given by the inertia model ω_{VSM}.

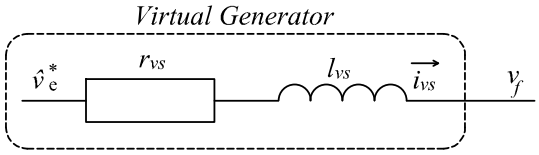

Figure 3.7: Quasi-stationary stator impedance model

$$i_{vs} = \frac{\hat{v}_e^* - v_f}{r_{vs} + j\omega_{VMS} l_{vs}} \tag{3.11}$$

The QSEM-based VSM architecture relay on filtering to prevent oscillatory or even unstable operation of the VSM [33]. This is achieved by introducing a low-pass filtered measurement v_m (3.12) of LCL-filter output voltage v_f. The crossover frequency ω_{vf} of the low-pass filter is recommended to be between 50 and 2000$[rad/s]$ depending on the tuning of the VSM [33].

$$\frac{d}{dt} v_m = \omega_{vf} v_f - \omega_{vf} v_m \tag{3.12}$$

In the final stator impedance model (3.13), V_m has replaced V_f. After replacing V_f with V_m, the stator impedance model increased to a 2$^{\text{nd}}$ order model, and issues with undesired oscillations during transients have been reduced with no effect on the stationary response. However, it is expected that the QSEM will be sensitive to the crossover frequency ω_{vf}, and poor tuning will lead to unstable or oscillatory behaviors in the VSM.

$$i_v s^{QSEM} = \frac{\hat{v}_e^* - v_m}{r_{vs} + j\omega_{VMS} l_{vs}} = \frac{r_{vs}(\hat{v}_e^* - v_m)}{r_{vs}^2 + (\omega_{VMS} l_{vs})^2} - j\frac{\omega_{VMS} l_{vs}(\hat{v}_e^* - v_m)}{r_{vs}^2 + (\omega_{VMS} l_{vs})^2} \tag{3.13}$$

The QSEM has been presented in scalar form (3.14) using the dq orientation presented in chapter 3.1. Splitting (3.13) into a real and an imaginary part by replacing i_{vs}^{QSEM} with $i_{vs,d}^{QSEM} + j i_{vs,q}^{QSEM}$ and v_m with $v_{m,d} + j v_{m,q}$. While $\hat{v}_e^*$ is orientated only along the d-axis and has no imaginary.

$$i_{vs,d}^{QSEM} = \frac{r_{vs}}{r_{vs}^2 + (\omega_{VMS} l_{vs})^2}(\hat{v}_e^* - v_{m,d}) - \frac{\omega_{VMS} l_{vs}}{r_{vs}^2 + (\omega_{VMS} l_{vs})^2} v_{m,q} \tag{3.14a}$$

$$i_{vs,q}^{QSEM} = -\frac{r_{vs}}{r_{vs}^2 + (\omega_{VMS} l_{vs})^2} v_{m,q} - \frac{\omega_{VMS} l_{vs}}{r_{vs}^2 + (\omega_{VMS} l_{vs})^2}(\hat{v}_e^* - v_{m,d}) \tag{3.14b}$$

3.3.2 Voltage control (outer loop)

The voltage source $\hat{v}_e^*$ controls the output voltage v_f of the VSM, similar to adjusting the field voltage on a real SM [33]. The voltage control structure (3.15) uses a standard PI controller to compensate for any deviation in the output capacitor voltage amplitude $\hat{v}_f$ and the desired voltage amplitude $\hat{v}_f^*$. The voltage controller is manually tuned with the propositional gain k_{pv} and integral gain k_{iv} acting on the integral state ξ. The voltage controller also has a reactive power droop, controlled by the reactive droop gain k_q. A reactive power droop minimizes the difference between the measured reactive power flow q_{VSM} and the desired reactive power flow q_{VSM}^*. The reactive droop gain k_q is typically 0.1 to prevent the reactive power drop from forcing $\hat{v}_f$ outside 10% during transients [44].

$$\hat{v}_e^* = k_{pv}(\hat{v}^* - \hat{v}_f) + k_{pv}k_q(q^* - q_m) + k_{iv}\xi \tag{3.15a}$$

$$\frac{d}{dt}\xi = (\hat{v}^* - \hat{v}_f) - k_q(q^* - q_m) \tag{3.15b}$$

Figure 3.8 shows the voltage control structure. A measure to prevent noise from being introduced back to the controller is to replace q_{VSM} with a low-pass filtered measurement q_m (3.16), and the cross-over frequency is set by ω_{qf}.

$$\frac{d}{dt}q_m = \omega_{qf}q_{VSM} - \omega_{qf}q_m \tag{3.16}$$

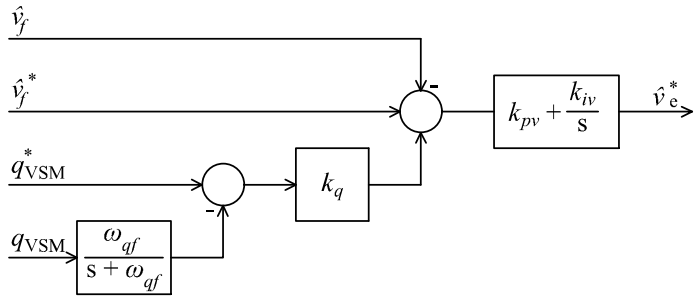

Figure 3.8: VSM voltage control adopted from [33]

3.3.3 Virtual inertia model

The well-known swing equation (3.17) describes the inertia and damping properties of an SM [28], [43]. As the main purpose of the VSM is to emulate inertia and the damping properties of an SM will, the swing equation also forms the foundation of the inertia model. The inertia model is used to determine the angular velocity ω_{VSM} of the VSM. The swing equation describes how the angular velocity of the rotor ω_r changes with mechanical torque T_m and electrical torque T_{el} delivered or consumed by the SM. The damping coefficient D act on the difference between the angular velocity of the grid ω_g and rotor ω_r. D is time-variant and depends on the operation point of the machine. While J_r is the combined rotor inertia of the SM and the mechanical power source feeding the SM, known as the prime mover.

$$J_r \frac{d}{dt}\omega_r = T_m - T_{el} - D(\omega_r - \omega_g) \tag{3.17}$$

For the virtual inertia model of the VSM it is convenient to present the swinging equation in terms of power (3.18) by multiplying all terms in (3.17) with ω_g. P_{el} is the electric power delivered or consumed by the SM, and P_m is the mechanical power driving the SM. SMs exhibits a damping torque almost propositional to the difference between the angular velocity of the grid and the rotor during stationary operation. Because of this proportionality, the time-variant D is replaced with a time-invariant damping coefficient k_d, resulting in a linear approximation of the damping torque around the synchronous working condition of the SM.

$$\omega_g J_r \frac{d}{dt}\omega_r = P_m - P_{el} - k_d(\omega_r - \omega_g) \tag{3.18}$$

The basis for the virtual inertia model (3.19) is the linear approximation of the swing equation (3.18). This linearized inertia model is no longer an approximation for the VSM as it is a design choice to choose the linear behavior of the VSM. There is no reason for the VSM to start at ω_{VSM} equal to zero, and VSM will always operate in the linear region of the SM. In (3.19) is ω_r replaced with the angular velocity of the virtual rotor ω_{VSM}. The VSM replaces the mechanical power source with a DC voltage source, modeled as an ideal virtual power source P^{r*}. Because increasing or decreasing P^{r*} changes the load angle of the VSM directly coupled to active power flow, the active power flow of the VSM is controlled by adjusting P^{r*}.

$$\omega_{AC} J_r \frac{d}{dt}\omega_{VSM} = P^{r*} - P_{VSM} - k_d(\omega_{VSM} - \omega_{AC}) \tag{3.19}$$

In equation (3.20) the virtual inertia model is converted to a per-unit system by changing the ideal virtual power source p^{r*}, the output power of the VSM p_{vsm}, and introducing the inertia time constant T_a equivalent to $2H$ in a traditional SM, where H quantifies the rotor's kinetic energy at synchronous speed [33]. Figure 3.9 shows an implementation of the per-unit inertia model.

$$\frac{d}{dt}\omega_{VSM} = \frac{p^{r*}}{T_a} - \frac{p_{VSM}}{T_a} - \frac{k_d(\omega_{VSM} - k)}{T_a} \tag{3.20}$$

In addition, are the per-unit angular velocity of the AC bus ω_{AC} replaced with a feedback k. k is either measured using a PLL or estimated using a low pass filter (3.21) feedback from ω_{VSM}. Where ω_d sets the cross-over frequency for the low-pass filter. This estimation holds if the grid frequency changes relatively slowly compared to the VSM.

$$\frac{d}{dt}k = \omega_d\omega_{VSM} - \omega_d k \tag{3.21}$$

To derive the phase angle of the VSM θ_{VSM} is the integral of the angular velocity ω_{VSM} multiplied by the base value of the angular velocity ω_b (3.22).

$$\frac{d}{dt}\theta_{VSM} = \omega_{VSM}\omega_b \tag{3.22}$$

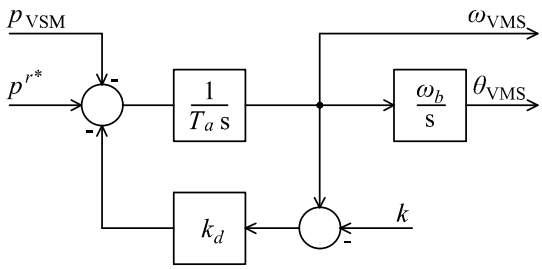

Figure 3.9: Virtual inertia model adopted from [33]

3.3.4 Frequency control (outer loop)

Frequency control, known as governor, controls the SM's frequency by changing the output power of the prime mover. Similar to VSMs, the frequency control of the VSM adjusts the output power of the ideal virtual power source, driving the virtual inertia model [33].

Figure 3.10 shows the frequency drop controller (3.23) with a proportional controller used to control p^{r*} based on the deviation between the angular velocity of the VSM ω_{VSM} and the desired angular velocity ω^*_{VSM} of the grid. The frequency drop gain k_ω ensures that VSM operates at desired angular velocity omega. The drop gain k_ω is typically between 20 and 60 to ensure minimal deviation between ω^*_{VSM} and ω_{VSM} to keep the VSM within the frequency limit of the grid [44]. The active power reference ω^*_{VSM} acts directly on p^{r*} to set the desired power flow in or out of the VSM.

$$p^{r*} = p^* + k_\omega(\omega^*_{VSM} - \omega_{VSM}) \tag{3.23}$$

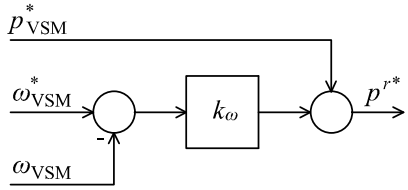

Figure 3.10: VSM frequency control adopted from [40]

3.3.5 Signal processing

The "signal processing" block shown in figure 3.6 measures the filter voltage v_f and the current i_c of the VSC. These measurements are transformed into the dq-reference frame using a park transformation (3.1) and scaled into the per-unit system presented in chapter 3.1.

The power calculations (3.24) give the active p_{VSM} and reactive power flow q_{VSM} of the VSM, determined by the d and q-axis filter voltages ($v_{f,d}$ and $v_{f,q}$) multiplied with the d and q-axis currents ($i_{c,d}$ and $i_{c,q}$) flowing in or out of the VSM.

$$p_{VSM} + jq_{VSM} = (v_{f,d} + jv_{f,q})(i_{c,d} + ji_{c,q}) \tag{3.24}$$

The power calculation is presented in scalar form (3.25) to separate p_{VSM} and q_{VSM}.

$$p_{VSM} = v_{f,d} i_{c,d} + v_{f,q} i_{c,q} \tag{3.25a}$$
$$q_{VSM} = -v_{f,d} i_{c,q} + v_{f,q} i_{c,d} \tag{3.25b}$$

The amplitude $\hat{v}_f$ of the filter voltage is determined using Pythagoras' theorem (3.26) on the d and q axis filter voltage ($v_{f,d}$ and $v_{f,q}$).

$$\hat{v}_f = \sqrt{v_{f,d}^2 + v_{f,q}^2} \tag{3.26}$$

3.4 Generator model

Generators used in ship power systems typically include a diesel or gas-powered engine as a prime mover. This prime mover feeds mechanical power to an SM, used to convert mechanical power into electrical power [28]. A typically ship power system consists of multiple generators feeding an AC bus connected to loads such as propellers, thrusters, and hotel loads to account for a considerable variation in load. It allows the system to connect or disconnect generators depending on the current load. Therefore, the generator model is designed to be removed from the grid entirely (planned or trip) during simulation or left electrically connected to the bus acting as a synchronous condenser, improving the voltage regulation and frequency stability by contributing to total grid inertia [45]. Figure 3.11 shows an overview of the generator model. The generator model consists of an SM model, an AVR controlling the output voltage of the SM by controlling the field current, and the governor controlling the prime mover speed/torque. The signal processing block converts the physical measurements to a per-unit system used by the controllers.

The following chapters will give a detailed description of the implementation, and table 3.5 lists all parameters used by the generator model.

Table 3.5: Parameters generator model

Parameter	Value
Nominal voltage, $V_{LL,RMS,SM}$	$690\,V$
Nominal apparent power, S_{SM}	1 MVA
Nominal frequency, f_{SM}	$50\,Hz$
Inertia constant, $j_{c,SM}$	0.8
Friction factor, $f_{f,sm}$	0.013
Number of pole pairs, $p_{p,SM}$	2
Stator resistance, r_s	$0.015\,pu$
Stator leakage inductance, l_{ls}	$0.080\,pu$
d-axis magnetizing inductance, l_{md}	$2.810\,pu$
q-axis magnetizing inductance, l_{mq}	$1.640\,pu$
Canay inductance, l_{f1d}	$0\,pu$
Field resistance referred to stator, r_{fd}	$0.004\,pu$
Field leakage inductance referred to stator, l_{lfd}	$0.531\,pu$
d-axis resistance referred to stator, r_{kd}	$0.234\,pu$
d-axis leakage inductance referred to stator, l_{lkd}	$0.655\,pu$
q-axis resistance referred to stator, r_{kq}	$0.034\,pu$
q-axis leakage inductance referred to stator, l_{lkq}	$0.241\,pu$
SM reactive power droop gain, k_{qg}	0.1
SM reactive power filter crossover freq, ω_{qfg}	$200\,\frac{Rad}{s}$
SM voltage controller propositional gain, k_{pvg}	35
SM voltage controller integral gain, k_{ivg}	70
SM frequency control gain, $k_{\omega g}$	40
Prime mover time response, T_e	$0.5\,s$

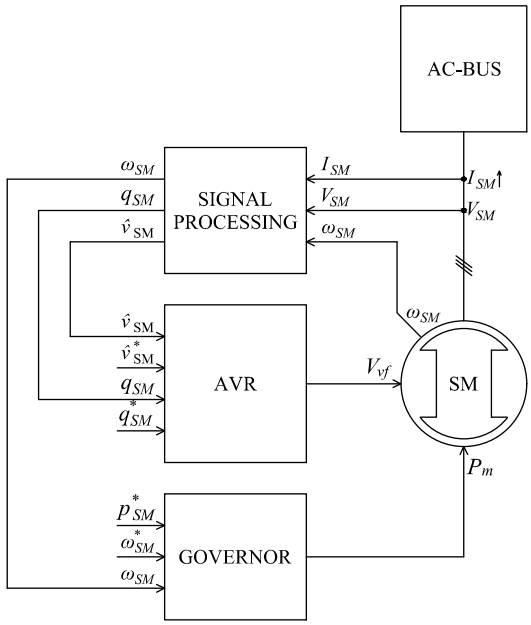

Figure 3.11: Generator model control structure

3.4.1 Synchronous machine model

The generator model uses a generic SM model named "Synchronous Machine pu Fundamental" from the Simscape™ library [46]. This SM model can either represent a generator or a motor, depending on the mechanical input. In the generator model, will this model operate in generator mode. The SM model uses two separate models describing the electrical and mechanical behavior of the SM, similar to the VSM [47]–[49]. The time-invariant swing equation (3.17) introduced in chapter 3.3.3 describes the SM's mechanical properties. Figure 3.12 shows an IEEE equivalent circuit of the electrical model. This inductance-based per-unit model forms the basis for the 5^{th} order state-space model (3.27) and comprehensively describes SM's electrical properties in the dq-reference frame. The electrical model represents the three-phase armature stator windings, the rotor containing the controllable field winding used to increase or decrease rotor flux, and damper windings that generate conducting and current paths during transients inhered to round body rotors. Designers also usually include similar conducting current paths in salient pole rotors with damper bars or windings to decrease oscillatory behaviors in the SM.

Appendix A includes the expanded matrices of the electrical model (3.27). Where $\mathbf{v^r}$ (A.1) is the voltage vector representing the different voltages of the SM, and the current vector $\mathbf{i^r}$ (A.2) represents the different currents. The per-unit resistance matrix $\mathbf{r^r}$ (A.3) represents the internal resistance of the SM. Similar to the internal inductance matrix $\mathbf{l^r}$ (A.4) represents the internal inductance of the SM. The last term in (3.27), $\omega_r \mathbf{J\Psi^r}$ decouples the stator and rotor of the SM (A.5).

$$\mathbf{v^r} = \mathbf{r^r i^r} + \frac{\mathbf{l^r}}{\omega_b}\frac{d}{dt}\mathbf{i^r} + \omega_r \mathbf{J\Psi^r} \tag{3.27}$$

The simulation model uses the same notation in figure 3.12 as the Matlab® documentation for the "Synchronous Machine pu Fundamental" Simscape™ block. The electrical model denotes stator armature winding resistance and leakage inductance r_s and l_{ls}, and stator magnetizing inductance l_{md} for the d-axis and l_{mq} for the q-axis. The field circuits are r_{fd} for field resistance, and field leakage inductance l_{lfd} referred to stator side. The salient pole SM has damper bars, or windings denoted r_{kd} for d-axis resistance and l_{lkd} for d-axis leakage inductance. Similar for the q-axis with r_{kq} representing the q-axis resistance and l_{lkq} for q-axis leakage inductance all referred to the stator. The Canay or "differential-leakage" inductance l_{lkq} compensates for physical differences in mutual inductance between the field winding and the armature winding compared to the field winding and the damper winding. v_d and v_q denote the d and q-axis stator

voltage. The field voltage is oriented in the d-axis and denoted v_{fd}. Finally, flux linkage between rotor and stator is denoted Ψ_d for d-axis flux and Ψ_q for q-axis. This equivalent circuit used fundamental parameters such as inductance and resistances to describe the electrical characteristics of the SM [50]. While equivalent circuit gives a detailed description of the SM, some parameters only exist in the equivalent circuits and are impossible to determine by measuring. Therefore are, these parameters typically estimated using standard parameters estimating the resistance and inductance equivalents based on time response measurements of the SM. The SM model in this report uses a predefined set of 1MVA parameters in the "Synchronous Machine pu Fundamental" Simscape™block. However, these parameters can be changed later to test a specific SM.

The "Synchronous Machine pu Fundamental" Simscape™block has limitations related to minimum load depending on the chosen numerical solver to avoid numerical noise [46]. The trapezoidal non-iterative solver will require a sizable resistive load proportional to the step size. For a $50\,Hz$ system, have a sample time equal to $100\,\mu S$ together with a resistive load at 0.1 (pu), proven sufficient to avoid numerical noise. However, changing the solver to a trapezoidal iterative (algebraic loop) will reduce the need for a resistive load at an increased numerical cost due to numerical loops.

3.4.2 Voltage regulator (AVR)

The excitation system consists of an exciter and an AVR and controls the terminal voltage of the SM [28]. The AVR uses the exciter mounted on the rotor shaft to supply DC currents to the field windings, controlling the SM's power factor to increase or lower the terminal voltage. The "Synchronous Machine pu Fundamental" Simscape™block uses a normalized field voltage v_{fd}. This normalized field voltage means that at zero load will 1 pu field voltage results in 1 pu stator voltage.

The field voltage v_{fd} controls the output voltage of the generator model and uses the same voltage controller as the VSM shown in figure 3.8. The voltage controller uses a standard PI controller to compensate for any deviation in the stator voltage $\hat{v}_{SM}$ compared to the desired stator voltage $\hat{v}^*_{SM}$. Tuning of the voltage controller is done manually with the propositional gain k_{pvg} and integral gain K_{ivg} acting on the integral state ζ. The voltage controller also has a reactive power droop, controlling the reactive power flow of the SM. The reactive droop controller acts on the difference between the measured reactive power q_{SM} and desired reactive power q^*_{SM}. The reactive droop gain k_{qg} is typically set to 0.1 to prevent the reactive power drop from forcing the generator output voltage $\hat{v}_{SM}$ outside 10% [44].

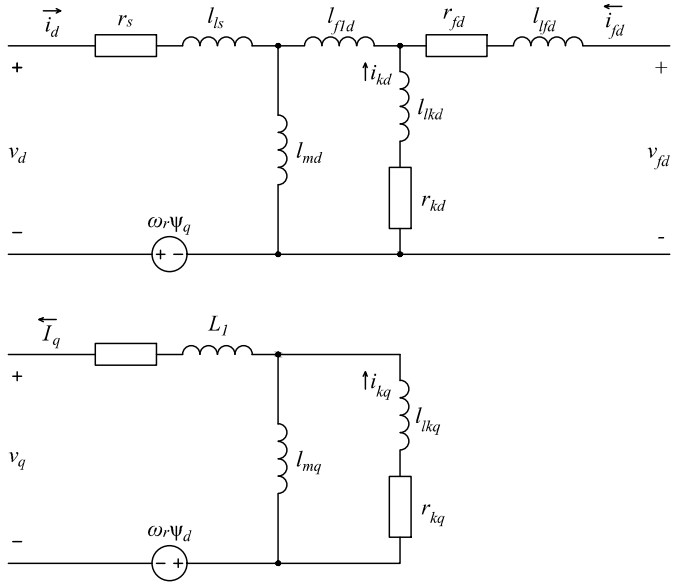

Figure 3.12: Per unit equivalent circuit based on inductance referred to stator terminals [47]

$$v_{fd} = k_{pvg}(\hat{v}^*_{SM} - \hat{v}_{SM}) + k_{pvg}k_{qg}(q^*_{SM} - q_{mg}) + k_{ivg}\zeta \tag{3.28a}$$

$$\frac{d}{dt}\zeta = (\hat{v}^*_{SM} - \hat{v}_{SM}) - k_q(q^*_{SM} - q_{mg}) \tag{3.28b}$$

Like the VSM, is q_{SM} low-pass filtered to prevent noise from being introduced back to the controller and SM by replacing q_{SM} with a low-pass filtered measurement q_{mg} (3.29). ω_{qfg} sets the cross-over frequency of the low-pass filter.

$$\frac{d}{dt}q_{mg} = \omega_{qfg}q_{SM} - \omega_{qfg}q_{mg} \tag{3.29}$$

3.4.3 Governor

Governors control the output frequency of diesel or gas generators by adjusting the torque output of the prime mover (engine) driving the SM. Fixed-speed diesel or gas engines typically used in ship AC power systems have a near-linear relationship between engine fuel input and output power [10]. Because of this linear relationship, diesel or gas engines are typically modeled using a delay or low-pass filter to represent how the engine responds. The engine time constant T_e is typically around 0.5 seconds for diesel engines and higher for gas engines [51]. Despite governors commonly being designed with an integral controller combined with a droop function, will the generator model use the same frequency controller as the VSM.

Figure 3.13 shows the governor's structure (3.30a) controlling engine fuel command and designed as a droop controller. The active power reference p^*_{sm} sets the desired active power flow by acting directly on the fuel command τ. The frequency drop gain $k_{\omega g}$ ensures that the angular velocity ω_{SM} of the SM is equal to the desired angular velocity ω^*_{SM}. $k_{\omega g}$ is typically set between 20 and 60 to ensure the generator stays within the frequency limits [44].

A low-pass filter (3.30b) represents the engine time response T_e adjusted with the crossover frequency ω_e. To ensure that the engine also contributes to the total generator inertia, $j_{c,sm}$ increased to 0.8 seconds.

$$\tau = p^*_{SM} + k_\omega(\omega^*_{SM} - \omega_{SM}) \tag{3.30a}$$

$$\frac{d}{dt}p_m = \omega_e \tau - \omega_e p_m \tag{3.30b}$$

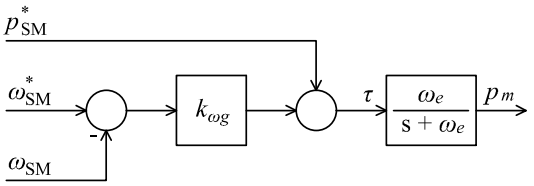

Figure 3.13: Governor control structure controlling diesel or gas prim mover

3.4.4 Signal Processing

The "signal processing" block seen in figure 3.11 measures the SMs output voltage V_{SM} and current I_{SM}. Together with the angular velocity of the rotor ω_{SM}. These measurements are then scaled to per-unit and transformed into the dq-reference frame using a park transformation (3.1).

The active and reactive power calculation is done in the dq-reference frame using (3.31). Where p_{SM} is the active power, and q_{SM} is the reactive power output of the SM. $v_{SM,d}$ and $v_{SM,q}$ are the stator d and q-axis voltages, and $i_{SM,d}$ and $i_{SM,q}$ are the d and q-axis currents flowing in or out of the SM.

$$p_{SM} = v_{SM,d} i_{SM,d} + v_{SM,q} i_{SM,q} \tag{3.31a}$$
$$q_{SM} = -v_{SM,d} i_{SM,q} + v_{SM,q} i_{SM,d} \tag{3.31b}$$

The amplitude $\hat{v}_{sm}$ of the stator voltage is determined using Pythagoras' theorem (3.32) on the d and q axis voltage ($v_{SM,d}$ and $v_{SM,q}$).

$$\hat{v}_{SM} = \sqrt{v_{SM,d}^2 + v_{SM,q}^2} \tag{3.32}$$

3.5 Load models

The simulation model consists of three different load models used to simulate different loads. These three models represent an active rectifier, a passive rectifier, and a pure impedance model.

The first load model presented is an active rectifier based on the VSC developed in chapter 3.2. Active rectifiers typically have lower harmonic distortion than passive rectifiers due to increased switching frequency [32], [52]. The second model is a twelve-pulse diode rectifier representing a passive front-end rectifier causing higher harmonic distortion than active rectifiers. Both the active and passive rectifier load model is variable, representing propellers and thrusters. The final load model is a pure impedance model. This model is necessary because the SM model requires a restive load to avoid issues with numerical noise and represent hotel loads and other constant consumers in ships. Table 3.6 lists all parameters used by the load models.

Table 3.6: Parameters load models

Parameter	Value
DC-load capacitance, c_{dc}	$4\,pu$
DC voltage controller propositional gain, k_{pdc}	25
DC voltage controller integral gain, k_{idc}	250
Transformer primary winding voltage, V_{p1}	$690\,V$
Transformer primary winding resistance, r_{p1}	$0.005\,pu$
Transformer primary winding inductance, l_{p1}	$0.04\,pu$
Transformer secondary winding voltage, V_{s1}	$690\,V$
Transformer secondary winding 1 resistance, r_{s1}	$0.005\,pu$
Transformer secondary winding 1 inductance, l_{s1}	$0.003\,pu$
Transformer secondary winding 2 voltage, V_{s2}	$690\,V$
Transformer secondary winding 2 resistance, r_{s2}	$0.005\,pu$
Transformer secondary winding 2 inductance, l_{s2}	$0.003\,pu$
Diode forward voltage, V_{df}	$0.8\,V$
Diode internal on resistance, R_{on}	$1\,m\Omega$
Constant hotel active load, p_h	$0.1\,pu$
Constant hotel reactive load, q_h	$0\,pu$

3.5.1 Variable voltage source converter load model

Active front-end drives increase complexity compared to traditional diode rectifiers. However, they are used as a rectifier to decrease harmonic distortion on the AC input due to higher switching frequency combined with active or passive power filters. VSCs used as a rectifier in inverters also decouples DC link voltage from the AC input voltage reducing sensitivity towards the supply voltage variations. Moreover, this decoupling in active front-end drives can increase DC link voltage levels, leading to higher AC voltage output and enabling electrical machines to achieve a higher speed without increasing stator currents.

The variable VSC load model uses the VSC control structure presented in chapter 3.2. In figure 3.14 the VSC is connected to a DC load to create a variable load model consisting of a sizeable ideal capacitor C_{DC} and controlled DC current source I_{DC}. The electrical power equation (3.33) ensures that the DC load has constant power consumption despite any changes in the DC voltage v_{DC} by adjusting i_{DC} to meet desired load p^*_{DC} based on the current DC voltage.

$$i_{DC} = \frac{p^*_{DC}}{v_{DC}} \tag{3.33}$$

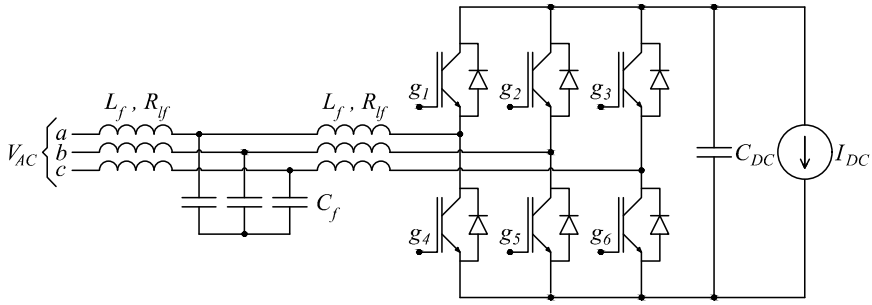

Figure 3.14: Variable voltage source converter load model

The control objective of the variable VSC load model seen in figure 3.15 is to keep C_{DC} at a constant voltage level. The DC voltage controller consists of a conventional PI controller (3.34) used to control the d-axis current reference i^*_d of the SRF-PLL current controller to keep v_{dc} constant. Tuning of the DC voltage controller is done manually with the propositional gain k_{pdc} and integral gain K_{idc} acting on the integral state η. Keeping reactive currents of the VSC to a minimum is desired, and the q-axis current

reference i_q^* is set equal to zero. A fast PLL response ensures proper decoupling between d and q-axis currents, which is essential to ensure that any impact in d-axis currents does not cause oscillations or other destructive behaviors in the q-axis currents.

$$i_d^* = k_{pdc}(v_{DC}^* - v_{DC}) + k_{idc}\eta \tag{3.34a}$$

$$\frac{d}{dt}\eta = v_{DC}^* - v_{DC} \tag{3.34b}$$

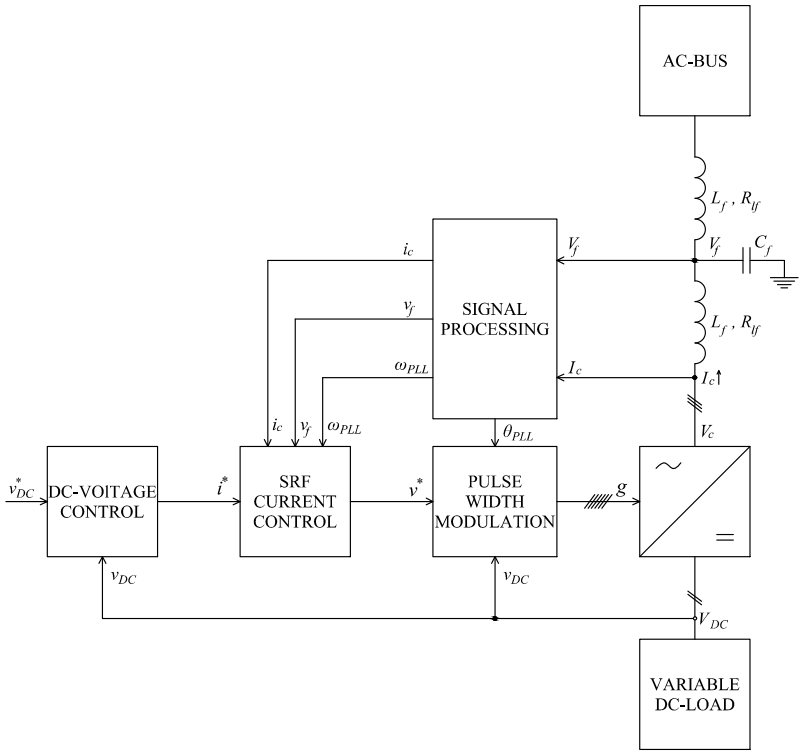

Figure 3.15: Variable voltage source converter load model control structure

3.5.2 Variable twelve-pulse diode rectifier load model

Diode rectifiers are used in everything from household products to massive industrial machines for AC to DC conversions due to their simplicity and control-free operation [53]. One of the main problems with diode rectifiers is harmonic distortion on their AC input. For high power, rectifiers are low-pass filters required to attenuate harmonic distortion caused by diode rectifiers, increasing the cost and complexity of the system. Twelve-pulse diode rectifier reduces harmonics in power systems without using filters by combining two three-phase diode rectifiers shifted 30° from each other using a transformer to cancel out harmonics. The twelve-pulse diode rectifier cancels out the 5^{th}, 7^{th}, 17^{th}, 19^{th}, 29^{th}, and 31^{st} harmonic produced by the rectifier, while the 11^{th}, 13^{th}, 23^{rd}, 25^{th}, 35^{th}, and 37^{th} will remain on the AC input.

A variable load model of the twelve-pulse diode rectifier has been developed similarly to the variable VSC load model by connecting a sizeable ideal capacitor C_{DC} and controlled DC current source I_{DC} on the rectifier output seen in figure 3.16. The current source I_{DC} uses the same electrical power equation (3.33) as the VSC load model. It ensures that the DC load has constant power consumption despite changes in the unregulated DC voltage V_{DC}. The twelve-pulse diode rectifier model uses the "Three-Phase Transformer (Three Windings)" Block from the Simscape™library [54]. The transformer has a 1:1 voltage ratio between the primary winding (Y) and the Y configured secondary winding and Δ configured secondary winding connected to conventional three-phase diode rectifiers.

3.5.3 Constant impedance load model

Hotel load in ship power systems represents control systems, navigation systems, heating, and other domestic loads, and short-term are these regarded as constant loads.

The constant hotel load model uses the "Three-Phase Parallel RLC Load" block from the Simscape™library configured as a Y-connected floating constant impedance [55]. The "Three-Phase Parallel RLC Load" block uses a per-unit system where p_h and q_h specify the active and reactive power of the hotel load and determine a constant impedance Z_h used during the entire simulation period calculated only once at simulation start up.

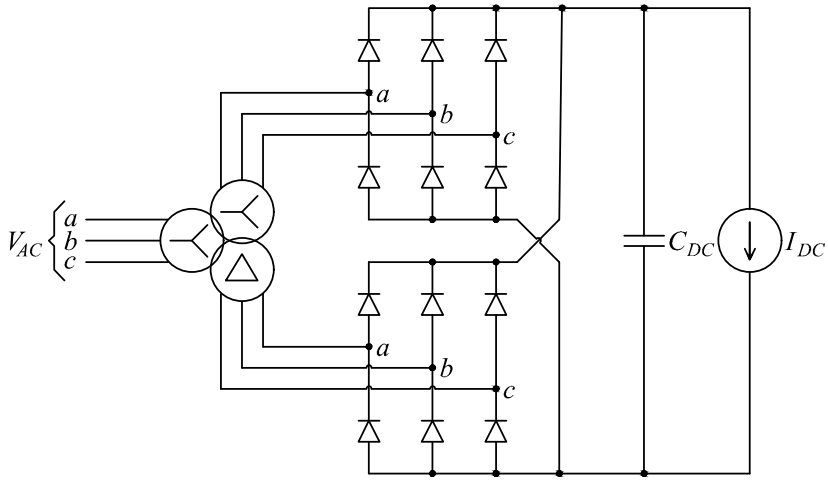

Figure 3.16: Variable twelve-pulse diode rectifier load model

Chapter 4

Simulation results and analysis

Reducing maintenance and fuel cost is of great interest to ship owners and operators for ship power systems as this is directly connected to the operational cost of vessels and increases the overall profitability. This chapter will discuss the effect of adding a VSM-based ESS in an AC-distributed ship power system to increase flexibility and grid stability, enabling the EMS/PMS to decrease operational cost, and GHG emissions. From an environmental standpoint, reducing GHG emissions is also closely related to fuel consumption and is essential to minimizing contribution to global warming.

While peak shaving is believed to reduce fuel consumption in hybrid diesel-electric ships, the actual savings from peak shaving are minimal. Because the potential fuel savings are limited, and potential savings will be lost in power conversion and battery efficiency [56], [57]. Instead, turning off generators is the main contributor to a reduction in operational cost from ESS in hybrid diesel-electrical propulsion systems using an EMS optimizes the power system by minimizing generators running at all times. The EMS utilizes the power reserve in power-producing units, with the ESS mainly supporting the grid as an emission-free power and inertia reserve. In other operations, generators can be replaced entirely with onshore energy stored in the ESS, such as ferries and operations with short transits and access to onshore power. Alternatively, strategic loading of the generators enables all-electric operation in moored ships, low load operations, or during shorter transits using energy produced by the generator sets at an earlier stage.

However, minimizing the number of power-producing units affects grid stability. In a DC-distributed power system, short-term stability results from the immediate energy reserve of capacitors or batteries. Therefore, integrating a battery-based ESS will contribute to this immediate energy reserve by directly supplying energy to the DC bus or using a DC/DC converter. However, short therm grid stability or inertia in AC systems fundamentally differs from DC systems as short-term stability is related to kinetic energy stored in the rotating mass of electrical machines connected to the grid. Therefore, adding a grid following ESS will not contribute to initial grid stability, only to the overall power balance. Changing to a grid-forming ESS using converters controlled as VSM is expected to improve some of the shortcomings of the grid-following ESS and give AC-distributed power systems the same benefits of the ESS as DC-distributed power systems. Using a VSM-based converted to interface the ESS, it will inherit essential properties such as inertia and electromechanical behaviors of the SM.

The VSM-based ESS can also use the same control structures used for the SM to simplify integration in highly dynamic and multi-source AC-grids such as ship power systems. This VSM-based ESS will simplify the integration of a PMS/EMS used to ensure grid stability and power balance of ship power systems as it uses the same interface as the generator, except the ESS can also consume active power. Typically, the PMS/EMS limits the rate of change and maximum load in large consumers such as thruster and main propellers, depending on the combined system inertia and power reserve to prevent frequency drops or blackouts in the grid. In low-load situations where a single generator powers the propulsion system, the PMS/EMS will limit/delay the rate of change in thrust or wait for generators to start in cases where the load exceeds the current grid capacity. This delay in thrust is unacceptable in some mission-critical operations such as DP, cable laying, and close to harbors, offshore wind or petroleum constructions requiring an increased spinning reserve to ensure safe operation. In AC-distributed diesel-electric power systems, similar to DC-distributed power systems, can a VSM-based ESS system reduce delay in thrust, using the battery as an immediate power reserve in low-load situations. This spinning reserve based on a VSM-based ESS can also simplify the integration of generators with slow response times, such as variable speed generators at low speed, and generators with alternative fuel types, such as LNG engines, used to reduce GHG emissions and operational costs. Load variations used in simulations presented in this chapter are based on the data set presented in chapter 2.3, indicating typical loads and load variations in a PSV. For this PSV, a ”constant” 10% base load covers hotel loads, such as control systems, base loads for the propulsion system, and production units, such as smaller compressors, pumps, and cranes. The total load of the PSV is dynamic and related to the propulsion system

and production equipment, such as larger compressors, pumps, and cranes. In the PSV data set, the maximum step in load at around 30% are related to switching on and off production equipment or a change in thrust, increasing power consumption in the propulsion system. However, in failure events, the power system shall sustain extreme load variations, such as in a trip event in one of the main propellers at maximum or close to the maximum load, without causing a blackout for the rest of the grid or violating the maximum tolerances for both voltage and frequency.

All electric distribution systems shall operate in accordance with national or international standards to ensure the safe operation of equipment and prevent damage to humans or equipment. These standards specify nominal levels and tolerances for voltage, frequency, EMC, and EMI enabling equipment from different manufacturers to coexist in the same grid. For electric distribution systems used in ships, DNV has defined an open classification which has been used to evaluate the performance of the VSM-based ESS in this report [44]. Table 4.1 lists essential requirements related to grid voltage, frequency, and harmonics.

Table 4.1: Tolerances for ship power systems during transient and steady-state [44]

Description	Value
Steady-state grid voltage	±2.5%
Transient grid voltage	−15% to +20%
Transient grid voltage after 1.5 seconds	±3%
Steady-state grid frequency	±5%
Transient grid frequency	±10%
Voltage harmonic distortion	5%
Total voltage harmonic distortion	8%

4.1 Islanded operation with VSM-based ESS

Islanded operation is an essential feature of the grid forming VSM converter as it enables the ESS to operate the entire AC-bus standalone as shown in figure 4.1. Islanded operation of the ESS can be used during shorter transit and enables plug-in hybrid solutions to operate using cheaper onshore power or moored ships with grid forming ESS to operate emission-free (locally) without any generators running. Because the load in moored ships typically is low compared to the battery capacity, can moored ships usually be sustained for extended periods by utilizing energy stored during

transit towards the harbor if onshore power systems are unavailable. Introduction of hydrogen-fueled ships are expected to be a part of the solutions moving toward decarbonization of the marine sector and an emerging technology [58]. Hydrogen can be converted to either mechanical energy using internal combustion engines or electricity energy using fuel cells. Because fuel cells supply DC-voltage grid forming DC to AC converter are necessary if hydrogen are used replace diesel engines as power source in AC-power systems.

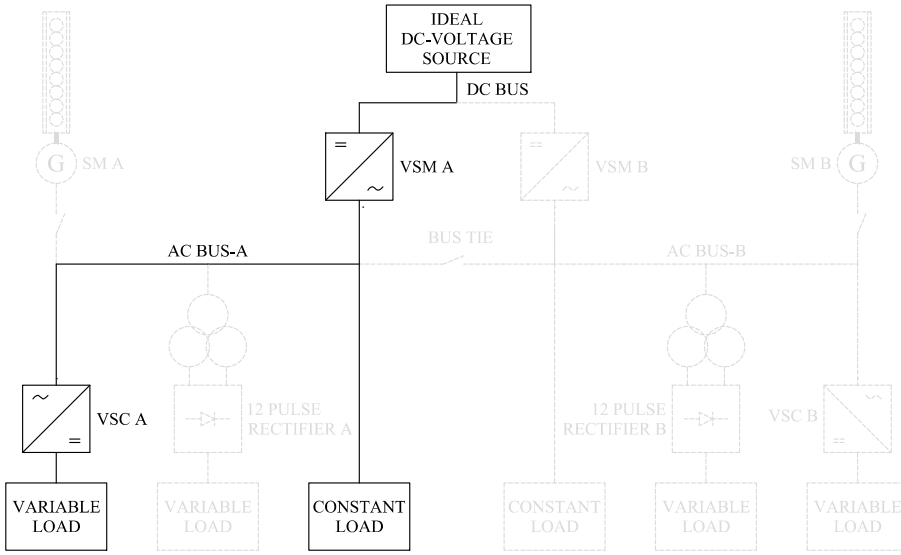

Figure 4.1: Configuration of simulation model during islanded operation with VSC load model

4.1.1 Typical load variations

Figure 4.2 presents the first simulation verifying islanded operation of the VSM related to grid stability after a typical step in load. The VSM-based ESS operates the AC-bus as the only power source, and the generator model is disconnected entirely from the grid shown in figure 4.1. On the consumer side is the pure impedance load model used to add a 10% baseload, while the variable VSC load model increases the load by 30% after 0.1 seconds. The combined inertia and fast primary control response of the VSM ensures that the maximum grid frequency deviation is limited to -1.5% well within the

+-10% limit specified for frequency transients by DNV. During stationary operation, the grid frequency stabilizes at a steady-state equal to −0.5% and stays within the ±5% limit. A slightly larger transient occurs in grid voltage maxing out at −5% with a 1% overshoot before the voltage stabilizes at 0.4% after 0.3 seconds, well within the +20% limit.

The simulation shows that both the frequency and voltage deviations are well within limits set by DNV and indicate that the VSM can deliver both inertia and primary control of the converter to operate the grid standalone during normal load variations.

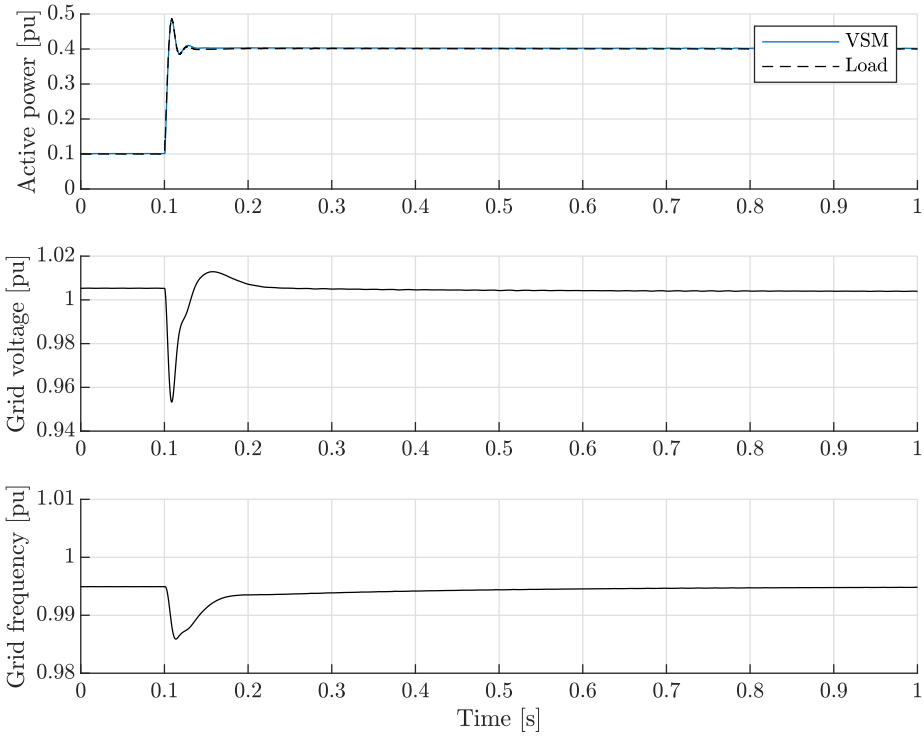

Figure 4.2: Islanded VSM operating grid during a typical change in load

4.1.2 Extreme load variations

Figure 4.3 presents an extreme load change that exceeds the regular operation of the grid and is limited to failure events such as a trip in one of the prominent consumers, such as the main propeller or thruster drives.

During the simulation, the VSM operates islanded as the only power source, with the variable VSC and constant impedance load model as consumers. The VSM operated at 100% load until a failure event occurred at 0.1 seconds, where the load instantly dropped from 100% to 10%, simulating a trip in a large consumer such as the main propeller. The initial response of the VSM dampens both grid frequency and voltage, combined with fast primary control of the VSM, keeping deviations in grid voltage and frequency to a minimum. The voltage controller keeps the grid voltage within the +20% limit and settles at 1.8% after about 250 milliseconds. The frequency control system keeps the grid frequency within the steady-state limit and settles at 4.4% after about 1.5 seconds. Because both the steady-state frequency and voltage are within their limits, it reduces the need for a fast secondary control system (PMS). Moreover, it gives the PMS time to adjust both the active and reactive power reference droop, to minimize the voltage/frequency deviation in the grid. As the VSM manages to keep the grid within limits set by DNV for ship power systems, the results indicate that the VSM can sustain and operate the grid during extreme changes in load without affecting other equipment connected to the grid.

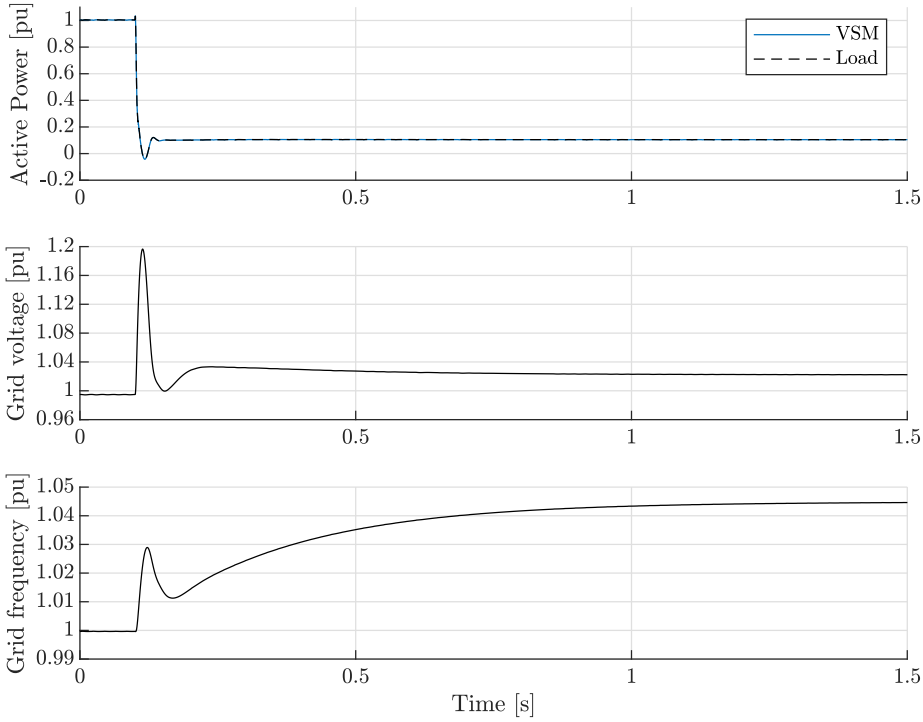

Figure 4.3: Islanded VSM operating grid during an extreme change in load

4.1.3 Sensitivity to inner-loop tunning

Islanded operation of the QSEM-based VSM has shown that low load situations are challenging for the VSM and can cause instabilities. Figure 4.4 shows three time-domain simulations of the VSM where the constant hotel load is decreased from 40% to 0.05% per unit at 0.1 seconds resulting in unstable operation of the VSM using modulus optimum-based tuning of the PI controllers with $k_{ad} = 1.2$ and $k_{ffv} = 1$ seen in the left column. By reducing the bandwidth of the PI controllers, the system becomes stable again, as seen in the middle collum. Alternatively, as in the right collum, increasing active damping $k_{ad} = 1.5$ of the LCL filter and setting the feedforward voltage term $k_{ffv} = 0$ also results in stable operation of the VSM at low loads.

The small-signal model attached in appendix B is similar to the simulation model and represents an islanded QSEM-based VSM operated with a reactive power droop instead of a frequency controller (AVR). The small-signal model show similar results to the time-domain model, and figure 4.4 presents eigenvalue trajectories of the VSM as the load moves from 100% load to 0.05%. The left column in figure 4.4, with modulus optimum-based VSC tuning, results in eigenvalue trajectories moving from blue towards red, eventually entering the right half-plane (black triangle) as the load decreases, resulting in an unstable system. In the middle column, the bandwidth of the PI controllers is reduced, resulting in a stable system also at low loads, as seen in the simulation model. However, by studying the eigenvalue trajectories in the right column, increasing the active dampening of the LCL filter pushed the eigenvalues further into the left half-plane resulting in increased dampening of the modes and a smoother response in the time domain. Based on this observation, will increasing k_{ad} and reducing k_{ffv} be preferred over reducing the k_{kpc} and k_{ic} during the island operation of the VSM.

Appendix C includes an abstract of a scientific publication under preparation. This paper will continue to investigate stability limits for an islanded QSEM-bases VSM to identify the sources of the stability problems and leads to recommendations for parameter tuning that can ensure stable operation of the QSEM-based VSM.

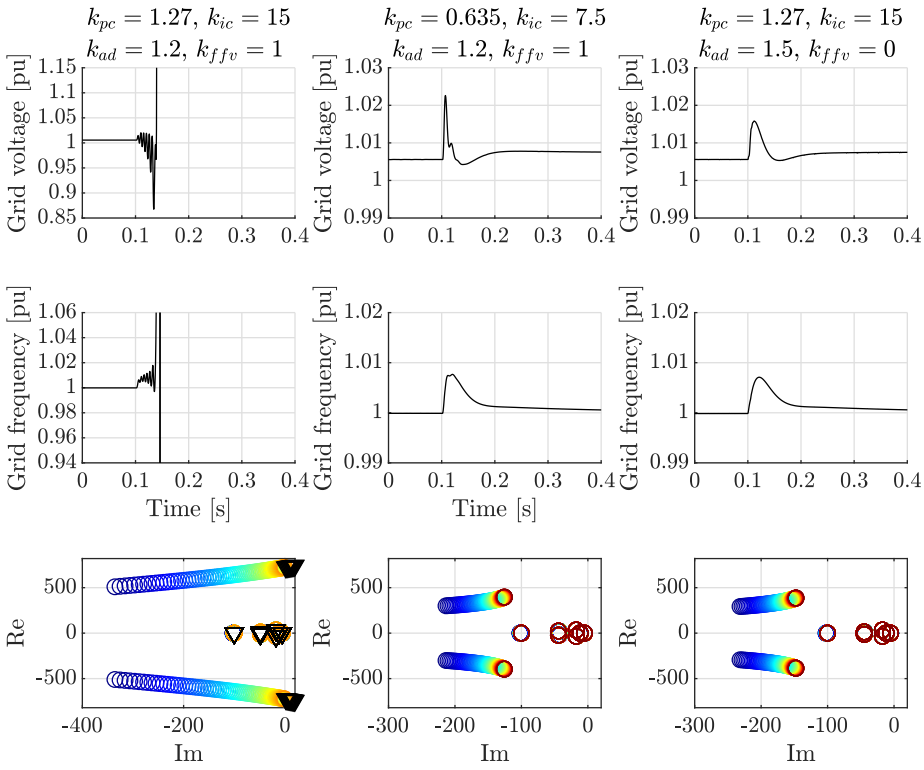

Figure 4.4: Effects of inner loop tuning depending on load (from blue 100% to red 0.05%)

4.1.4 Sensitivity to voltage feedback in QSEM

The QSEM implementation used in the VSM omits all dynamical behaviors connected to the electrical model of the SM, and the QSEM-based VSM relies on a low-pass filter (3.12) in the voltage feedback to ensure stable operation of the VSM. Therefore, will the crossover frequency ω_{vf} play a critical role in ensuring the stable operation of the VSM. To verify the effects ω_{vf} has on grid stability have, four time-domain simulations with increasing crossover frequencies been executed and presented in figure 4.5. Where the islanded VSM initially operates at 10% load until a 30% step in load occurs after 0.1 seconds, increasing the total load to 40%. This change in load causes a drop in voltage/frequency at 0.1 seconds, disturbing the VSM and used to verify the effects of ω_{vf}.

Figure 1 shows that ω_{vf} below 46 Hz or larger than 1400 Hz results in unstable operation of the QSEM-based VSM, and ω_{vf} tuned between these two results in stable operation of the VSM. Setting $\omega_{vf} = 800$ results in stable operation of the VSM and decreases deviation in both frequency and voltage compared to $\omega_{vf} = 200$. Figure 1 also contains a parametric sweep of ω_{vf} using the small-signal model of the islanded VSM with a 10% constant load attached in appendix B. The eigenvalue trajectories moving from dark blue ($\omega_{vf} = 40Hz$) to red ($\omega_{vf} = 1500\,Hz$) confirm that the small-signal model is stable for ω_{vf} between 40 Hz and 1500 Hz, and the VSM becomes unstable with a complex eigenvalue in the right half of the complex plan for ω_{vf} bellow 40 Hz or above 1500 Hz.

The article [33] conducted a similar parametric sweep of ω_{vf} with the QSEM-based VSM connected to an AC power source. Their results show that connecting the QSEM-based VSM to another AC power source allows for a wider selection of ω_{vf} than islanded operation seen in figure 4.5. This indicates increased sensitivity toward voltage filter tuning during islanded operation of the QSEM-based VSM. Therefore, is it recommended to keep ω_{vf} between 200 Hz and 1000 Hz if the QSEM-based VSM will operate islanded. Further testing also shows that ω_{vf} equal to 800 Hz results in the lowest real part of the eigenvalue trajectory independent of the load and is preferable if the QSEM-based VSM operates islanded.

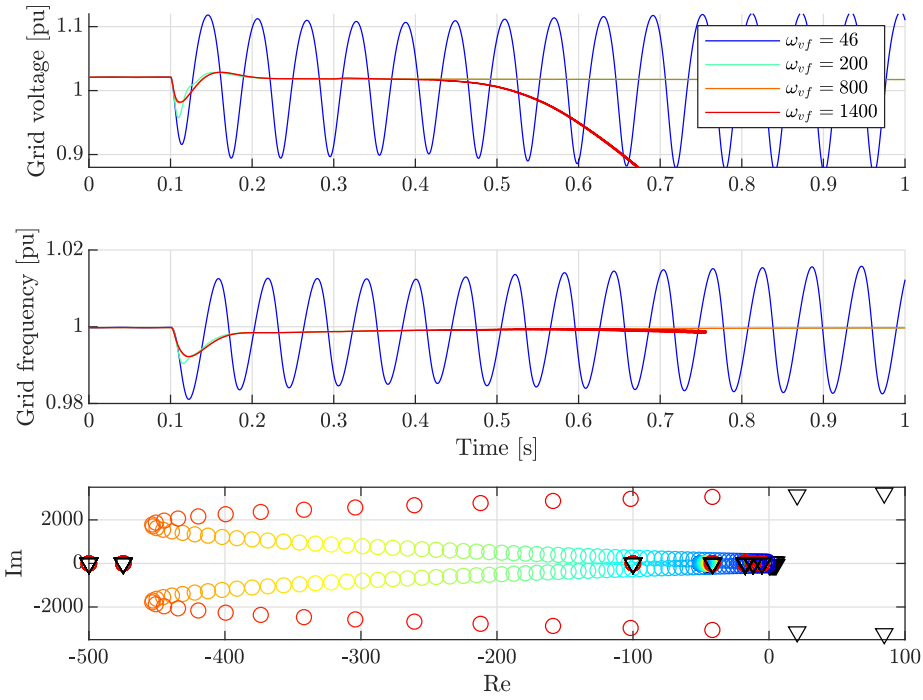

Figure 4.5: Effects of low-pass filter in QSEM stator voltage (from blue 30 Hz to red 2200 Hz)

4.1.5 Sensitivity to virtual stator impedance in QSEM

To verify how the virtual stator inductance of the QSEM affects grid stability during islanded operation of the VSM. Four simulations of the islanded VSM were executed with different virtual stator inductance and presented in figure 4.6. As a baseline, a simulation using the generator model islanded has been included, showing the response of an SM with the initial inertia response followed by slow oscillations that slowly converge towards zero after about 4 seconds. The VSM operates the grid with an initial load at 40% during the simulation. After 0.1 seconds, the VSC load model steps down from 30% load to zero leaving only the remaining 10% load supplied by the constant impedance load model. The islanded VSM shows that decreasing the virtual inductance will increase the sensitivity of the VSM and result in faster regulation of the grid until the VSM becomes over-sensitive and fails to operate the grid. The bottom row shows an eigenvalue trajectory from blue $l_{vs} = 1$ to red $l_{vs} = 0.01$ and confirms that decreasing l_{vs} will result in eigenvalues moving towards the imaginary axis and become unstable for values of l_{vs} below 0.15 both in the small-signal model and time-domain simulation model. These results show that virtual inductance below 0.15 will make the unstable during islanded operation. Virtual inductance l_{vs} should, therefore, be chosen carefully and preferably between 0.35 and 0.2.

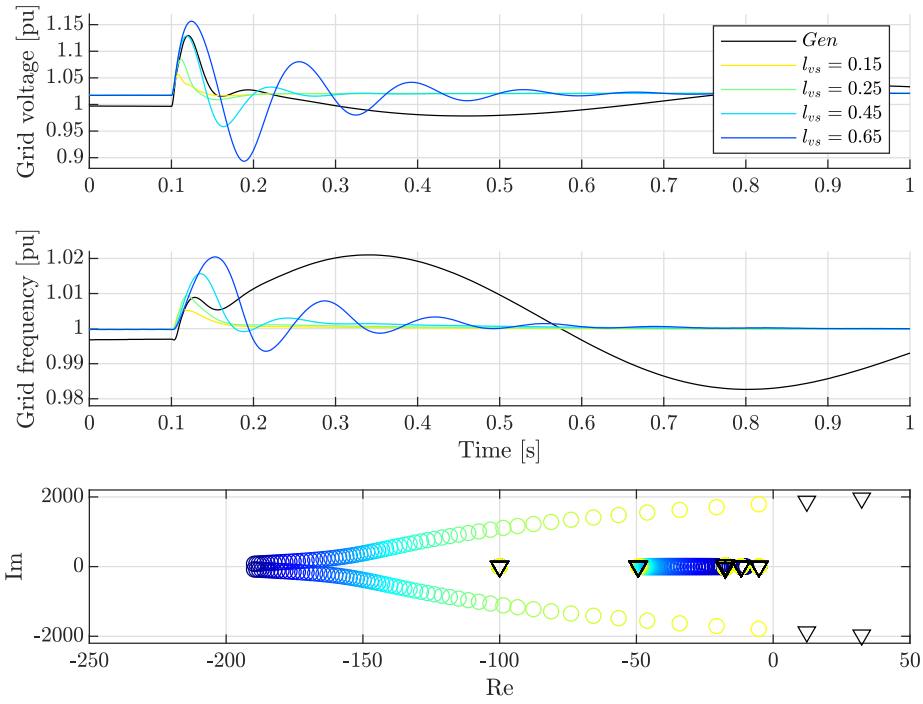

Figure 4.6: Eigenvalue trajectories of virtual stator resistance at 10% load (from blue 1 to red 0.01)

Reducing virtual stator resistance r_{vs} will decrease the cross-coupling between d and q-axis currents in the QSEM, and keeping r_{vs} as low as possible is desired. To verify the effects of r_{vs} has, simulations with both r_{vs} equal to 0.01 and 0 been executed and presented in figure 4.7. These results show that the QSEM can operate with r_{vs} equal to 0 with similar performance in terms of grid stability as r_{vs} equal to 0.01 with a well tuned VSC. These results are confirmed by the eigenvalue trajectory sweep of r_{vs} from blue (0.1) to red (0) where the eigenvalues trajectories stops at $-130 + j380$ for r_{vs} below 0.001. Simulations show similar results at loads below 1% and indicate that reducing r_{vs} to 0 can reduce cross-coupling in the QSEM during islanded operation.

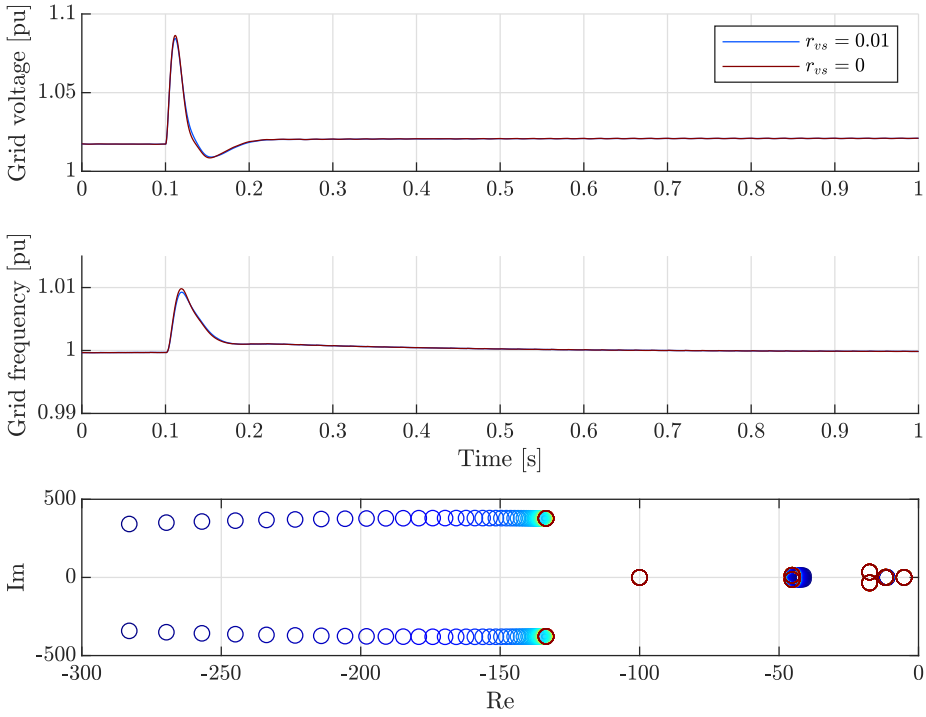

Figure 4.7: Eigenvalue trajectories of virtual stator resistance at 10% load (from blue 0.1 to red 0)

To verify how the r_{vs} affects the system with a VSC already near the stability margin, have a parametric sweep of r_{vs} been executed and presented in figure 4.8. This parametric sweep starts at r_{vs} equal to 0.1 and moves towards r_{vs} equal to 0.01, while the VSC is tuning is $k_{pc} = 1.27$, $k_{ic} = 15$, $k_{ad} = 1.2$ and $k_{ffv} = 1$, resulting in an unstable operation of the QSEM at r_{vs} below 0.013. These results indicate that if the VSC is close to the stability margin, a trade-off between VSC tuning and r_{vs} results in increased stability, and r_{vs} equal to zero requires a well-tuned VSC.

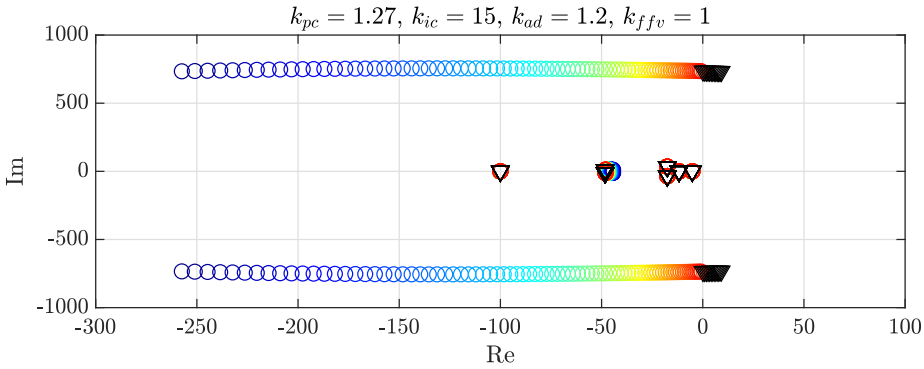

Figure 4.8: Eigenvalue trajectories of virtual stator resistance at 10% load with VSC close to the stability margin (from blue 0.1 to red 0.01)

4.1.6 Sensitivity to frequency feedback in inertia model

The damping torque describes how the VSM resists changes in grid frequency and is one of the essential properties of the VSM. The inertia model (3.20) introduced in chapter 3.3.3 relay on frequency feedback to determine how much damping torque to apply during transients in grid frequency and results from the difference between the angular frequency of the VSM and the grid. The grid frequency is either estimated or measured before the difference between ω_{VSM} and ω_{AC} is multiplied by the damping coefficient k_d.

Figure 4.9 shows a series of simulations with varying crossover frequencies for ω_d and ω_f, used to evaluate how estimated feedback using a high-pass filter compared to measured feedback with a PLL in the inertia model will affect grid frequency and damping properties. During the simulation, the VSM operates the grid islanded. The initial load is 10% until the load is stepped up to 40% after 0.1 seconds using the variable VSC load model. In the left column are grid voltage and frequency presented using different crossover frequencies in the PLL. There is no significant difference as long as the PLL filter tunning is within a typical range between 1 and 200 milliseconds. In the right column are k replaced and an estimation of the angular frequency, and again there is no significant difference between different crossover frequencies. The estimated feedback provides a shorter settling time as it eliminates dynamics of the PLL. However, this may change when the system operates with a combination of VSMs and generators, as a PLL always give a reliable synchronization to the grid frequency.

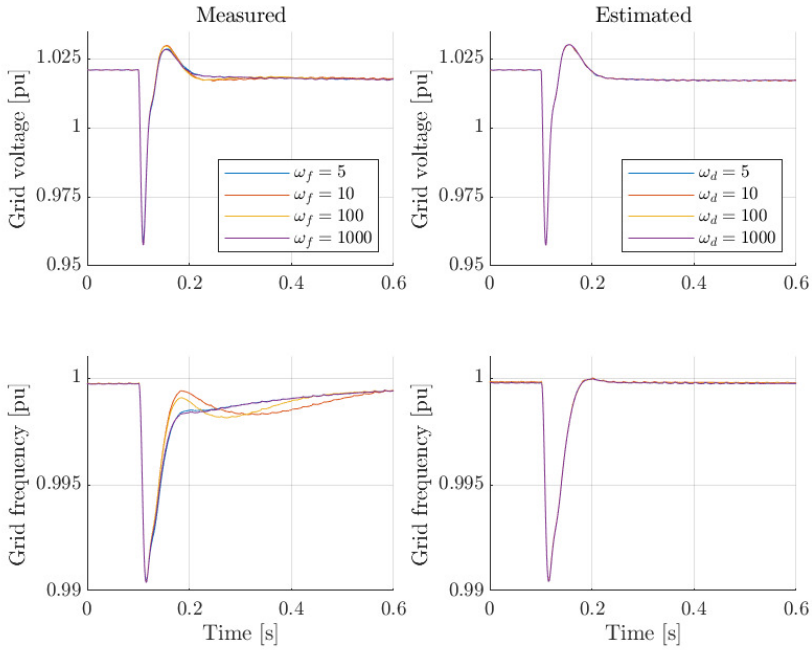

Figure 4.9: Comparison between measured and estimated grid frequency feed back in inertia model

4.1.7 Sensitivity to grid harmonics

Large variable frequency AC to AC drives used to control speed and torque in trusters and propellers are typically designed with a passive front-end to reduce cost and simplify the control structure of the drive. Drives designed with a passive front-end introduce an increased level of harmonics in the AC-grid and may cause instabilities in other equipment connected to the grid, such as the VSM. To verify the VSM's sensitivity towards grid harmonics, the variable VSC load model is replaced by the variable twelve-pulse load model, as seen in figure 4.10.

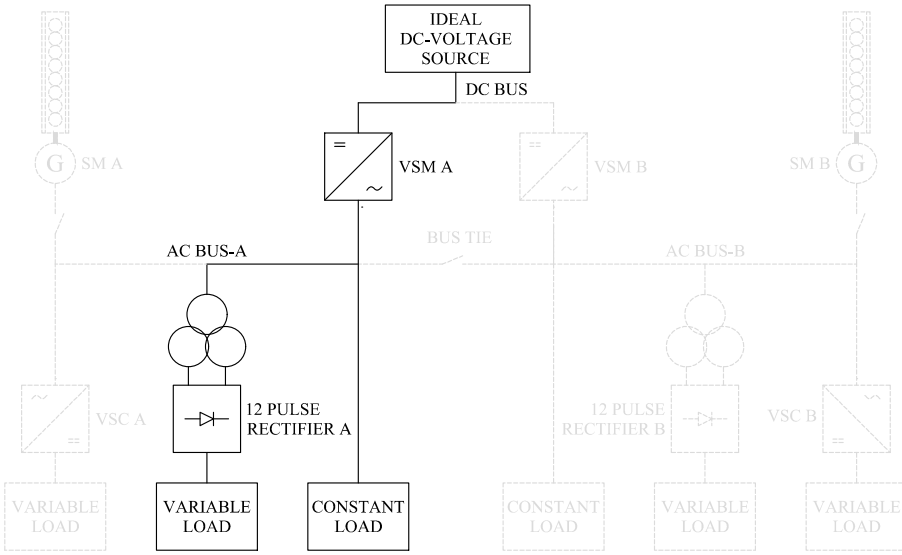

Figure 4.10: Configuration of simulation model during islanded operation with twelve-pulse load model

Initially, the VSM operates the grid at 70% until the load increases at 0.1 seconds to 100%, where the twelve-pulse load model represents 90%, and the remaining 10% is the constant impedance load model. DNV have specified that no single order voltage harmonic shall exceed 5% and total harmonic distortion shall not exceed 8% to ensure normal operation of equipment connected to the grid. A spectrum analysis of the grid voltage are presented in figure 4.11 show single order harmonics occurring at 11^{th}, 13^{th}, 23^{rd}, 25^{th}, 35^{th}, and 37^{th}. The total harmonic distortion of the grid has increased

to 3.2%, and the 11^{th} harmonic are the largest single order harmonics at 2.5%. Because harmonics introduced by the twelve-pulse rectifier have no visual effect on the VSM, have the twelve-pulse rectifier been modified to a six-pulse rectifier to further increase harmonics in the grid.

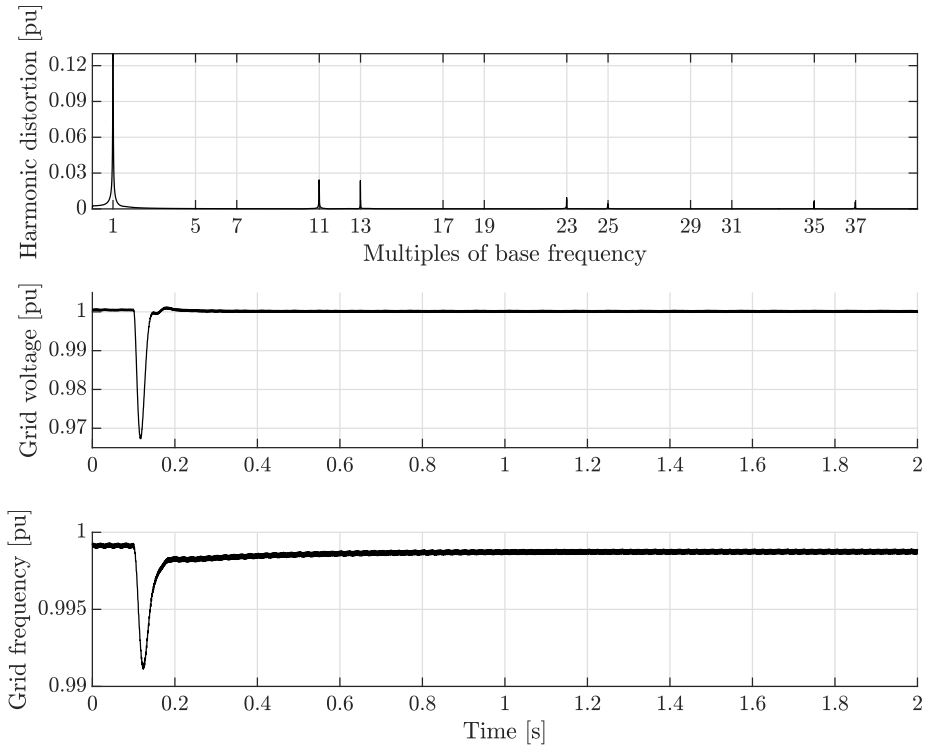

Figure 4.11: Islaned VSM operating grid with harmonic distortion from twelve-pulse diode rectifier

Replacing the twelve-pulse rectifier with a six-pulse rectifier without additional filtering has increased harmonic distortion in the grid. Figure 4.12 shows a spectrum analysis of the grid where the total harmonic distortion has increased to 11.5%. With the 5^{th} harmonic as the most significant single order harmonic at 10.6%, both violate the limits set by DNV and exceed the expected levels of harmonic distortion in ship power systems. Despite these high levels of harmonic distortion, does the VSM operate the grid with only a tiny increase in transient oscillations seen in grid voltage and

frequency. It should be noted that the VSM model uses an ”average” based VSC model, eliminating high-frequency harmonics from the VSC with low amplitude. However, low-frequency harmonics from passive diode rectifiers will dominate the noise floor. Therefore, removing these high-frequency harmonics from the grid reduces only the total THT and is not expected to affect these results.

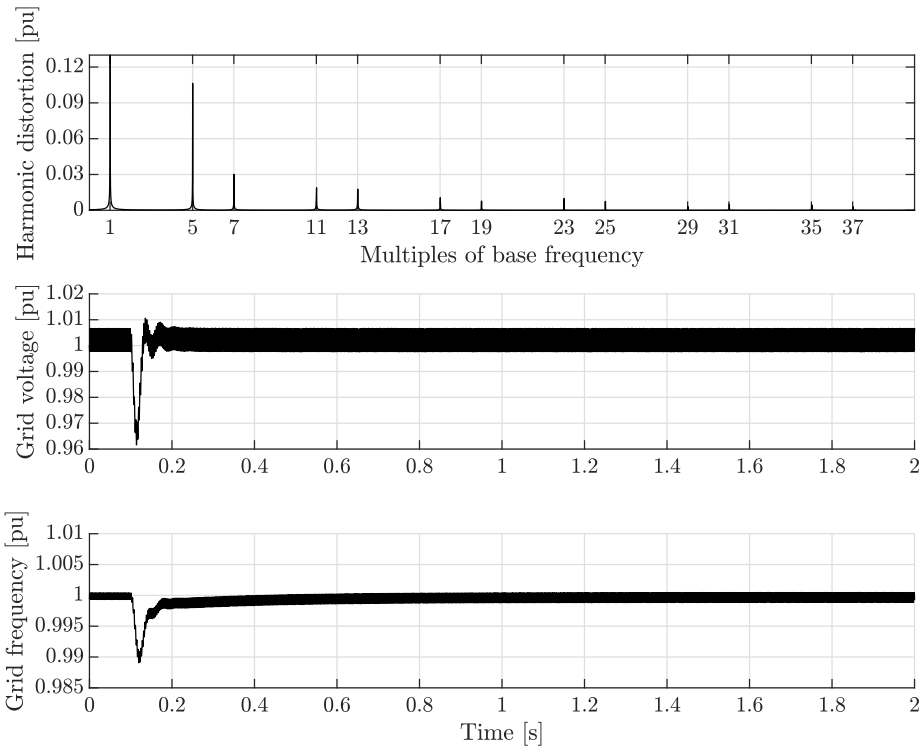

Figure 4.12: Islaned VSM operating grid with harmonic distortion from six-pulse diode rectifier

4.2 Improved grid stability with VSM-based ESS

The VSM-based ESS will also operate in multi-power grids, as seen in figure 4.13. This system consists of both generators and the VSM, and the VSM needs to handle dynamical loads without decreasing performance of the existing power system. This section aims to verify how the VSM-based ESS can support a low inertia grid during operation and reduce the need for spinning reserve during typical operations and during failure events. Load sharing among power sources is also an important subject and determines the complexity and design of PMS/EMS used to manage power and energy distribution in ship power systems.

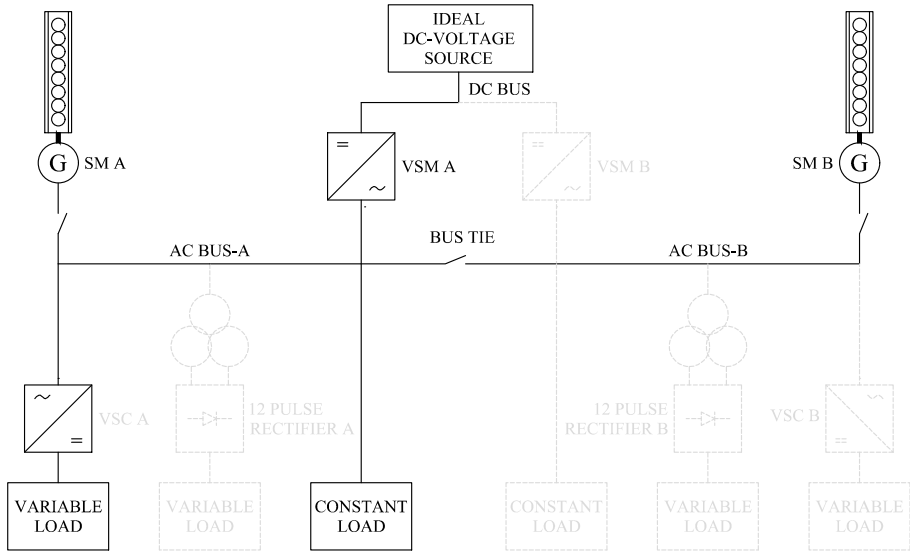

Figure 4.13: Configuration of simulation model with VSM operated in multi-power grid

4.2.1 Typical load variations with grid supporting VSM-based ESS

To verify how the VSM-based ESS can support a single generator in terms of grid voltage and frequency during a typical change in load has, three simulations been executed with different configurations and presented in figure 4.14. Both single generator and

dual generator operations of the grid have been added as a baseline and used to compare the performance of a VSM-based ESS. The grid also consists of a pure impedance load model used to add a 10% baseload and a variable VSC load model used to increase the load by 30% in one step after 0.1 seconds.

While all configurations manage to stay within limits set by DNV for ship power systems during a typical step in load, a single generator has a significant deviation in grid voltage and frequency power due to low grid inertia and power reserve. Adding a second generator will double the total grid inertia and power reserve, improving both voltage and frequency stability. The second generator has decreased the voltage deviation from -9% to -3% transient and the following oscillations. Grid frequency is also improved, reducing deviations from -2.5% to -1% with decreased oscillatory behaviors. Changing to a single generator combined with a VSM has further improved grid stability due to the added ”virtual” inertia and fast primary frequency regulation of the VSM. The combined inertia and fast primary control response of the VSM ensures that the maximum grid frequency deviation is limited to -0.6% and stabilizes at a steady-state frequency equal to -0.01%. A slightly larger transient occurs in grid voltage, maxing out at -2.5% with close to zero oscillations before stabilizing at -0.1% after 1.5 seconds.

These simulations show that the VSM can replace a second generator as a ”spinning” reserve and maintain short-term grid stability due to the ”virtual” inertia of the VSM. As a result of the imitated energy supply of the battery/DC bus, the VSM-based ESS provides a faster frequency regulation of the grid, reducing oscillations in frequency and voltage to a minimum.

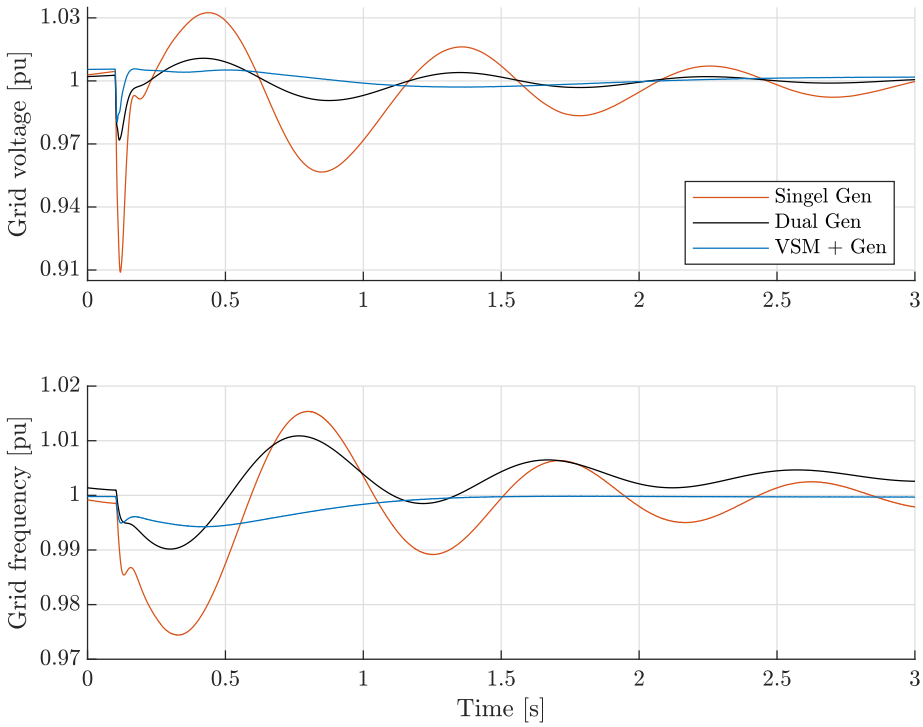

Figure 4.14: Grid Voltage and frequency during a typical change in load

4.2.2 Extreme load variations with grid supporting VSM-based ESS

To verify how the VSM-based ESS supports the grid during extreme changes in load compared to a traditional power system. Have simulations of a power system with a single generator, dual generators, and a single generator with grid-supporting ESS been simulated an presented in figure 4.15. The grid also consists of a pure impedance load model used to add a 10% baseload and a variable VSC load model used to decrease the load by 90% in one step after 0.1 seconds. This step in load close to 100% is challenging and requires inertia and fast primary regulation of power-producing units. All simulations are executed without a PMS updating the power reference of power-producing units to verify the stationary operation and if the initial and primary frequency control can stabilize the grid without any interaction from a PMS.

Simulations with a single generator resulted in large transient voltages at 50%, violating the +20% limit set by DNV and proves how challenging trips are. Transients at this scale are likely to damage equipment or cause trip in safety equipment connected to the grid and will most likely cause a blackout in parts or the entire grid. However, further tuning of the AVR and governor function in the generator is likely to improve the standalone operation of the grid. The oscillations at 0.5 seconds originate from the variable VSC load model reacting to voltage variations in the grid. Changing to the variable twelve plus load model removes these oscillations entirely. Despite these undesired oscillations are, the variable VSC load model preferred as it simulates a more realistic simulation of a trip event due to a faster rise time.

Adding a second generator increases the grid's total power reserve and inertia, improving grid stability during an extreme change in load. An extra generator reduced the transient voltage overshoot from 50% to 13.9%, together with the following oscillations, without re-tuning the AVR or governor. The increased grid inertia and power reserve provided by the second generator also improve grid frequency and reduce deviation from 8.6% to 4.3%, combined with reduced oscillations. Changing the configuration to a single generator combined with a VSM-based ESS has further improved grid stability due to the added "virtual" inertia and fast primary frequency regulation of the VSM. Similar to simulations of the islanded VSM, there are no signs of the grid supporting VSM struggling with significant variations in load, and the combined inertia and fast primary control response reduced frequency deviation to 2.1% in the grid. The grid stabilizes at a steady-state frequency equal to 1.3% and improves settling time in grid frequency by one second compared to a duel generator setup. A slightly larger transient occurs in grid voltage for all configurations. This transient is reduced from 13.8% in the dual generator configuration to 9.5%, and settling time is improved by 0.5

seconds with the VSM-based ESS. All stationary values are within DNVs requirements without interaction of the PMS and give the PMS time to adjust the generator's power droop without violating any stationary voltage or frequency requirements.

Similar to chapter 4.2.1, these simulation results show that a VSM-based ESS can replace a second generator while improving grid stability during extreme load variations without increasing operational costs and GHG emissions compared to a single generator. As a result of the immediate energy supply of the battery/DC bus, the VSM-based ESS also reduces transients and oscillations in grid frequency and voltage compared to a generator operated as a "spinning" reserve.

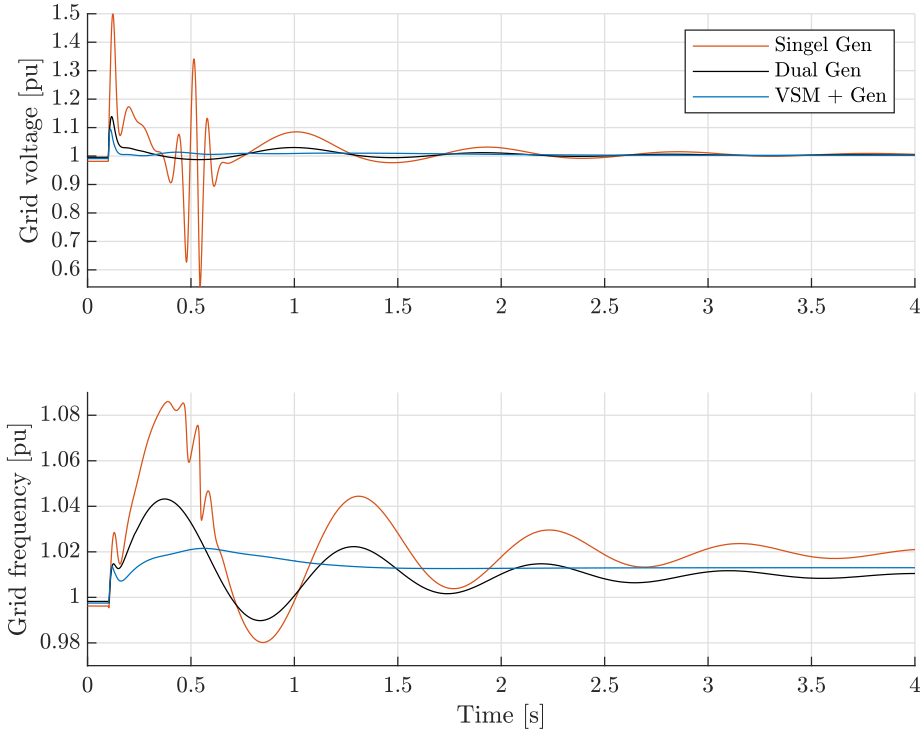

Figure 4.15: Grid Voltage and frequency during a extreme change in load

4.2.3 Load sharing between grid supporting VSM-based ESS and Generator

One of the benefits of using a VSM-based ESS in AC-distributed power is inherent load sharing between the VSM and generator sets. The PMS/EMS controls the stationary power balance by adjusting the power references of the VSM-based ESS and generator. To verify how the system distributes active and reactive power between the VSM and the generator during grid supporting operation, have simulations of a typical step in load been executed and presented in figure 4.16. During grid supporting operation, the generator delivers all energy to the grid stationary by setting the active power reference equal to the current load and leaving the active power reference of the VSM equal to zero, as seen initially in figure 4.16. After 0.1 seconds, the PMS/EMS increased the active power in one step from 10% to 40% by adjusting the variable VSC load model and the power reference of the generator simultaneously. The initial response of the generator is to release kinetic energy stored in rotating machinery, also known as the inertia response. Simultaneously the VSM feeds about the same amount of energy from the battery due to the VSMs ”virtual” inertia. Shortly after, the primary frequency controller of the VSM increases active power delivery to the grid due to the fast frequency control and an immediate power reserve of the battery. Because the VSM-based ESS handles the initial power delivery, the governor function of the generator has time to ”slowly” increase power delivery and replace the VSM entirely after one second. The reactive power of the grid is balanced to keep the grid voltage at a nominal level by setting the reactive power droop reference to zero on both the Generator and VSM-based ESS, leaving the voltage controller to balance reactive power in the grid.

These results indicate that the VSM-based ESS is, as anticipated, able to inherently share transients or changes in load with the generator by contributing to grid inertia and primary frequency control. Because the VSM-based ESS provides the initial energy for the primary control, the prime mover has time to increase output power steadily and positively affect fuel consumption. Because the VSM-based ESS also uses the same interface as a traditional generator, this simplifies the integration of a PMS/EMS. The VSM-based ESS has inherent load sharing, and if the combined power references of generators and VSMs are below the grid’s actual power output, the remaining load is divided equally. Alternatively, if the generator’s power reference is higher than the actual power consumption, will the VSM act as a load storing energy in the battery until the power reference of the generator is updated to meet the actual power consumption. As a result of the VSM’s ability to automatically balance the system, this reduces pressure on the PMS/EMS system to update power references.

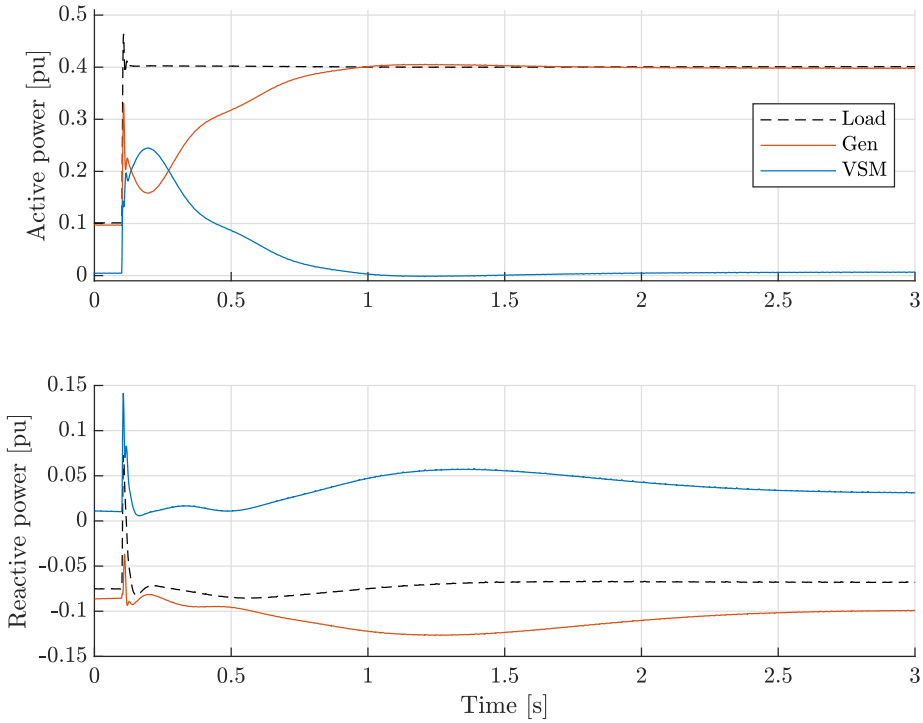

Figure 4.16: Load sharing between generator and grid supporting VSM during a typical change in load

4.2.4 Load sharing between grid feeding VSM-based ESS and Generator

The primary function of a grid-supporting ESS is to provide a spinning reserve in operations with strict requirements for grid reliability, reducing the total number of spinning generators by replacing generators and increasing the load on the remaining generators powering the grid. In some situations, this load increase exceeds the generator's remaining power reserve and requires the PMS/EMS to turn on a second generator for a potentially short duration. In these situations, the energy stored in the battery can prevent turning on a second generator to cover a potentially short-term increase in power consumption. With a correct-sized battery, the ESS will typically have no issues supporting a low load for an extended period.

Figure 4.17 shows a simulation of a situation where the load exceeds the generator's capabilities, and the VSM is used to cover the load temporarily. Initially, the VSM operates as a spinning reserve for the grid where the generator is powering the grid standalone at 90% capacity. After 0.1 seconds, the total load increases from 90% to 110%, exceeding the generator's capabilities. Without the ESS, will this require a second generator to be turned on, reducing the total efficiency of the grid operating with two generators at low loads instead of a single generator with an optimal load. Because PMS/EMS initiates the thrust command, can the active power reference of the VSM be updated simultaneously as the PMS/EMS are increasing the load. The initial grid reaction then is to split the load equally between the VSM and the generator due to the combined system inertia before the primary control system stabilizes the grid and moves toward the power reference set by the PMS/EMS. Moreover, the simulation shows that the grid frequency and voltage stayed well within the requirements set by DNV, indicating that the system has no issues operating at a load exceeding the maximum capacity of a single generator supported by the VSM.

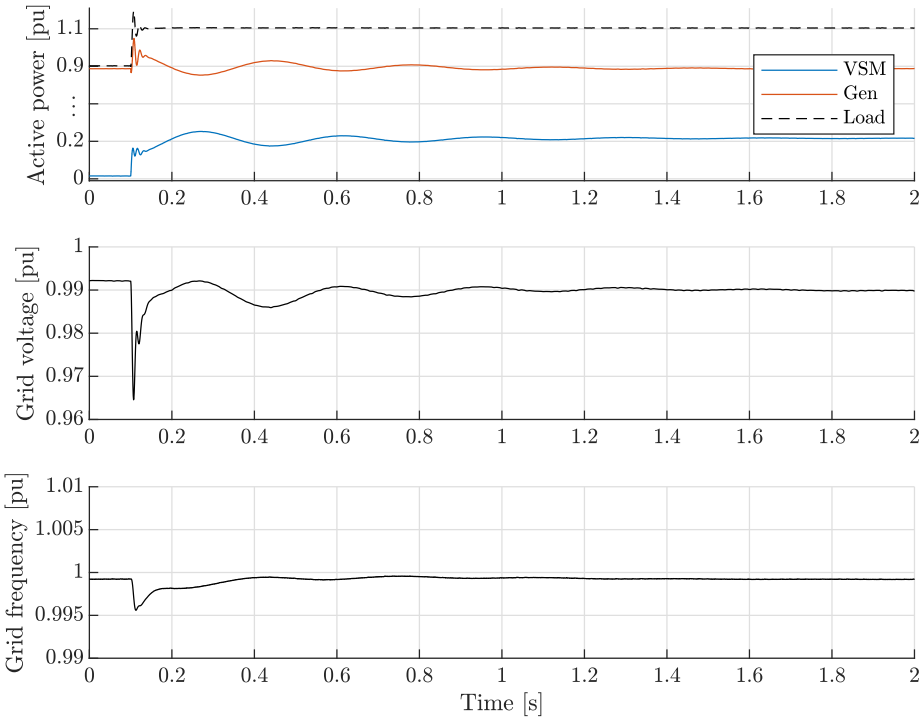

Figure 4.17: Load sharing between generator and VSM

4.2.5 Prime movers with slow response time in AC-distribution systems

Generators based on diesel engines dominate the market of electric ship power systems. However, other fuel types, such as LNG, have recently begun to challenge this to reduce ship's GHG emissions and operational costs. Replacing a diesel engine with an LNG engine will increase the generator's response time due to the slow load response in LNG engines [51]. The increased response time of the generator will result in slow primary frequency control and decrease grid stability regardless of system inertia. To overcome issues related to slow load response in LNG engines affecting the grid, have mechanical and electrical ESS solutions been proposed to support the grid during transients and rapid changes in load.

Figure 4.18 shows a system simulated with a slow prime mover powering the generator. The Governor model relays on the prime mover time response constant T_e to simulate the response of a diesel engine, and increasing T_e to 4 seconds results in a much slower load response simulating an LNG engine. During the simulation, the ESS is used to support the generator with an initial load equal to 10% before the load increased to 40% in one step 0.1 seconds into the simulation. The initial inertia response of the grid shares the load equally before the primary frequency control takes over, similar to the simulation presented in chapter 4.2.3. The faster VSM-based ESS supports the grid, giving the generator time to increase slowly. The main difference is that the generator now uses about 4.5 seconds instead of 1 second to reach a stationary point set by the PMS/EMS.

The VSM's combined inertia and fast primary control response ensure that the maximum grid frequency deviation is limited to -1.2%, with a slightly larger transient occurring in grid voltage at -2%, both well within the stationary requirements set DNV. Indicating the VSM-based ESS can support the grid until the slower LNG engine has increased power delivered.

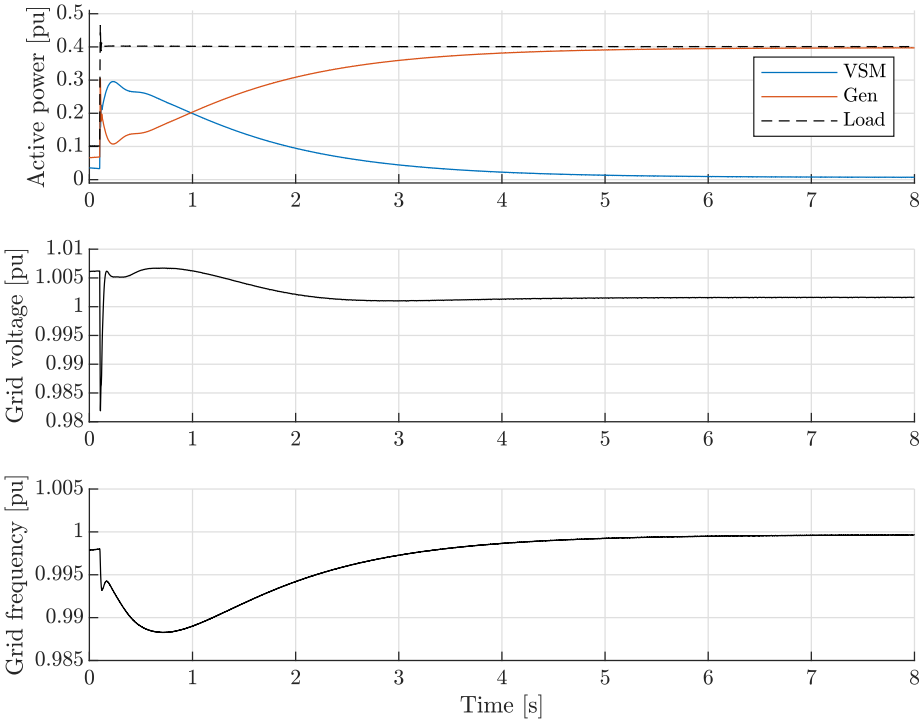

Figure 4.18: Load sharing between slow generator and grid supporting VSM

4.2.6 Transition between grid supporting and islanded operation of the VSM-based ESS

A grid-following ESSs rely on a generator or other grid-forming solutions to form a grid the PLL-based VSC can follow, making islanded operations challenging in ship power systems. Some grid-following ESSs can operate a grid standalone by setting a fixed frequency and regulating the grid voltage. While this is a possible solution, it will require a changeover in the control structure. In many cases, this transition will require a complete shutdown of the grid transitioning between grid following and islanded operation or at least increase the real-time requirements of the system and PMS/EMS to enable a transition without a blackout of the grid.

The VSM-based ESS simplifies this process by seamlessly transitioning between multi-power and islanded operations of the grid. Figure 4.19 shows a planned transition between grid-supporting and islanded operation of the VSM-based ESS. The generator initially powers the grid at 40% load before the PMS/EMS updates the power reference and begins the transition from a grid-supporting to a grid-feeding ESS. Two seconds into the changeover, the VSM and generator reach the new stationary point with 40% load in the VSM and 0% in the generator. At this point, the generator is disconnected from the grid, leaving the VSM islanded. Transients are normal when disconnecting equipped for the grid, and the "Three-Phase Breaker" block switches when the current passes through the first current, zero-crossing as an actual high power switch [59]. However, to keep the generator model numerically stable, a large snubber load is used to bleed energy from the disconnected generator model. Therefore, is this transient most likely introduced or affected by this snubber load switching "on" before the generator model is disconnected entirely. Independent of this transient, there is no indication of the VSM-based ESS struggling with the transition between grid-supporting and islanded operation, keeping the grid frequency and voltage within 1% during the transition. Because the VSM and Generator operated independently, there are no longer any real-time requirements of the PMS/EMS systems during transitions between grid-supporting and islanded operations of the VSM-based ESS. However, reconnecting a generator to the grid will require resynchronization between the generator and the grid/VSM, similar to reconnecting a generator to grids operated by other generators.

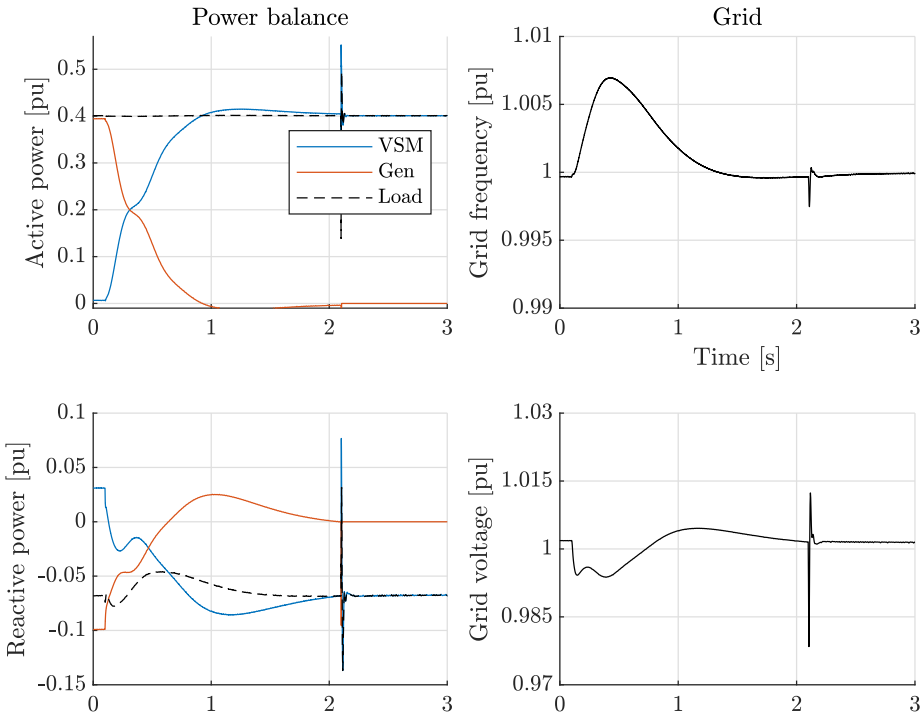

Figure 4.19: The VSM-based ESS is transitioning from multi-power to islanded operation of the grid

4.2.7 Load sharing with ”virtually” closed bus ties

To verify the dual-infeed concept and if the VSM can create a ”virtual” bus tie used to transfer energy between AC bus A and B via the DC bus. The simulation model is reconfigured, as seen in figure 4.20, with two active VSMs, a single generator, and open bus ties.

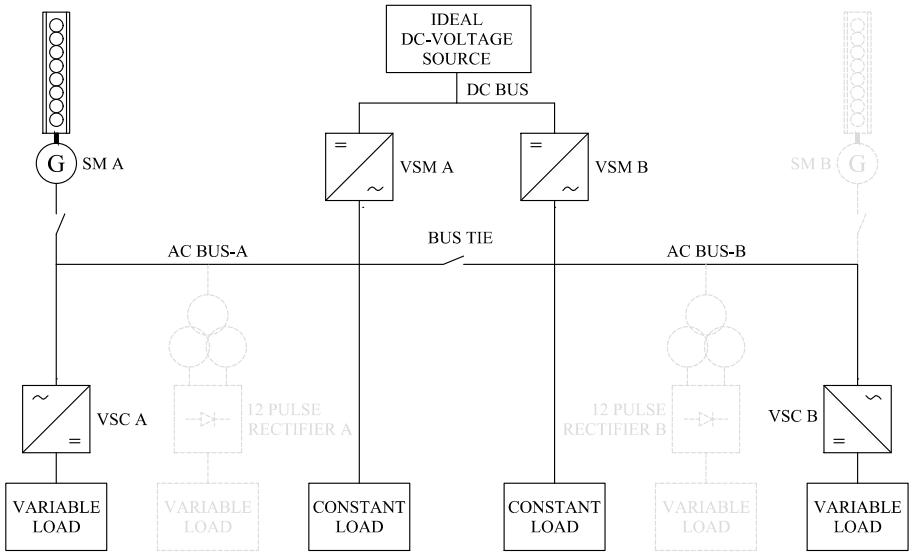

Figure 4.20: Configuration of simulation model during two-bus operation with open bus ties

These simulations are intended to verify ship operations with high requirements for grid reliability, such as DP, cable laying, and close to harbors, offshore wind, or petroleum constructions. To meet these requirements are ships operating with open bus-ties and increased spinning reserve to ensure safe operation. In a traditional diesel-electric ship, will this require at least four generators running independently of the actual load. Introducing an ESS in these systems can replace generators operated as spinning reserves, decrease the number of running generators, and reduce GHG emissions and operational costs. An exciting feature of an ESS using a common DC bus presented in chapter 2.4 is the ”virtually” closed bus. The concept behind a ”virtually” closed bus is to transfer power between AC bus-A and B in situations with open bus

ties using the common DC bus. To achieve this, VSM A is operated as a load in bus A, feeding energy to the DC bus, and VSM B power bus B islanded using energy for the DC bus or the opposite. Therefore, using a ”virtually” closed bus can reduce the number of running generators by matching any configuration of generators from four to one depending on the load as if the system operated with closed bus ties.

Figure 4.21 shows a ”virtual” closed bus simulation where the initial load is 10% in each bus before the load increases to 40% in one step at 0.1 seconds. In bus A the initial response of the inertia and primary frequency control system is to stabilize the grid frequency by temporarily increasing the power output of VSM A. The PMS/EMS has also updated the power reference of generator A at 0.1 seconds, and after about one second, generator A reaches the stationary power output at 80%. At this point, VSM A transfers energy to the DC bus operating as a 40% load in bus A again. Simultaneously, VSM B operates bus B islanded using energy from the DC bus stored in the battery. The battery operates, therefore, as an energy reserve for both bus A and B until generator A has increased power output and regained its position as the primary energy source. This simulation indicates that the VSM-based ESS can transfer energy between bus-A and B while contributing to grid stability. Moreover, a dual-infeed ESS solution can reduce GHG emissions and operational costs in ships during operations with high requirements for grid reliability.

However, because the two VSMs can consume/deliver power to the AC simultaneously, will the combined power output determine the battery size for batteries directly connected to the DC bus to prevent damage to the battery. Alternatively, the VSMs must have limitations depending on State-Of-Available-Power (SOAP) to protect the battery from damage [60]–[62]. While optimizing battery size is challenging and depends on parameters such as ship size, type, and operations are this important to maximize profits from ESS installations in ship power systems.

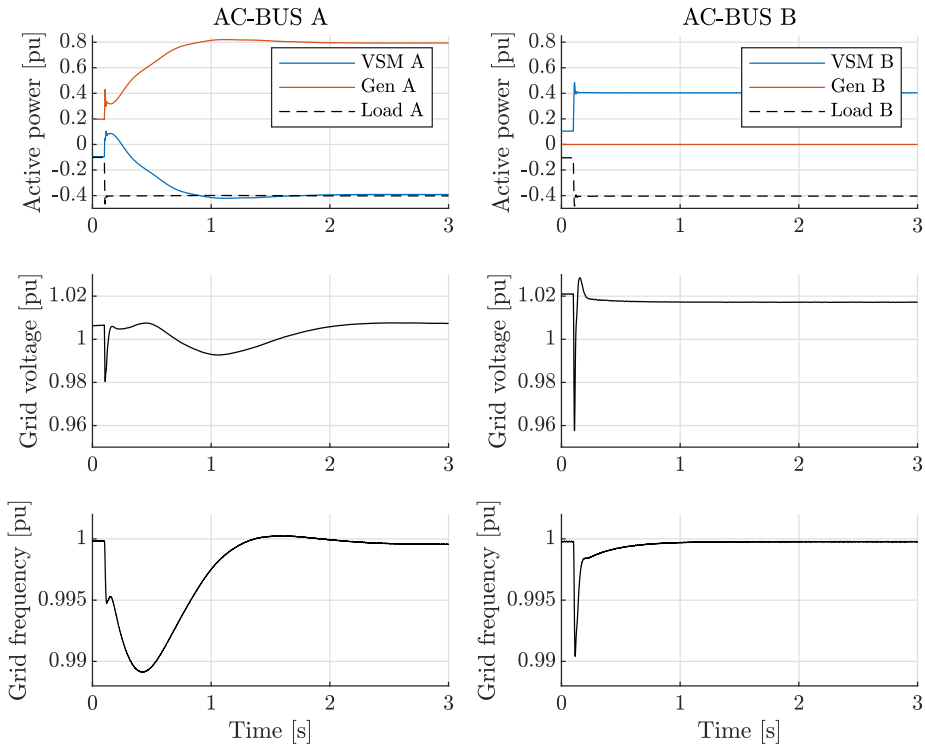

Figure 4.21: Load sharing with ”virtual” closed bus-ties

4.2.8 Load sharing between multiple grid supporting VSMs and generators

Ships typically operate with closed bus-ties with generators and the VSM-based ESS connected to a common grid during transit, as seen in figure 4.22. During transits are, the load is generally high and constant, as seen in chapter 2.3.2, which limits the ability of EMS to optimize energy consumption with an ESS. In this situation, the best option is to change fuel type or increase efficiency in the generators. Chapter 4.2.5 showed that the VSM-based ESS could improve grid stability in systems with slower prime movers enabling a more comprehensive selection of fuel types. Another method of increasing efficiency in fixed-speed diesel generators is increasing the load using the ESS for grid support. Because ship power systems typically are designed with multiple generators of different sizes (i.e., 2+2), can generators be matched to be as close to 100% load as possible and use the ESS as power reserve during transits.

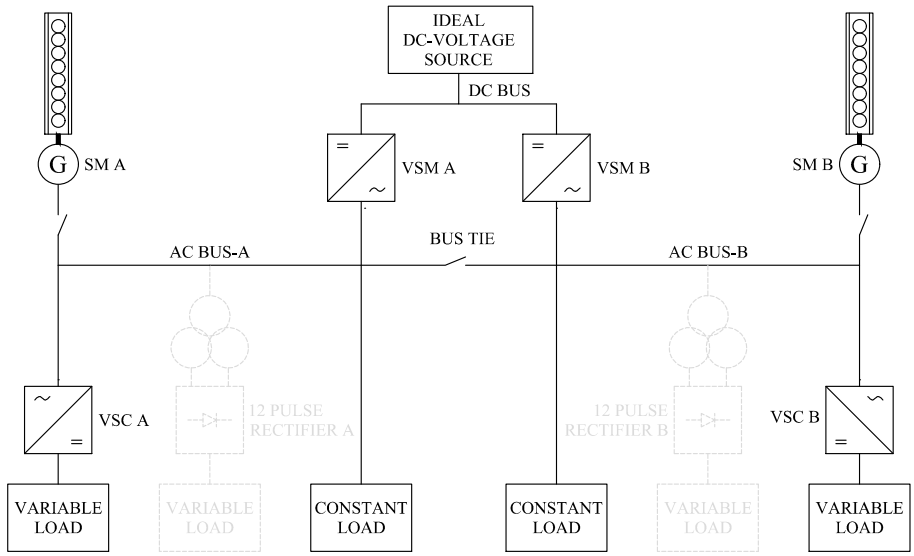

Figure 4.22: Configuration of simulation model during two-bus operation with closed bus ties

To ensure that multiple VSMs operated in the same grid are able to share the load equally, a simulation during transit operation was executed and presented in figure 4.23. Initially, each generator operates with 10% load, and the ESS supports the grid without delivering power to the grid. After 0.1 seconds, the load increased to 60% in one step. The simulation shows a similar response to a single VSM supporting the grid, and the inertia response was shared equally between the VSMs and generators. The following primary frequency response of the VSMs supports the grid until the generators have reached their stationary point and regained their position as the primary energy source.

The simulations show that the grid voltage and frequency are kept well within the limits set by DNV. The load is shared equally between the generators and VSMs, with the VSMs only supporting the grid during transients and changes in load as intended for a grid supporting ESS.

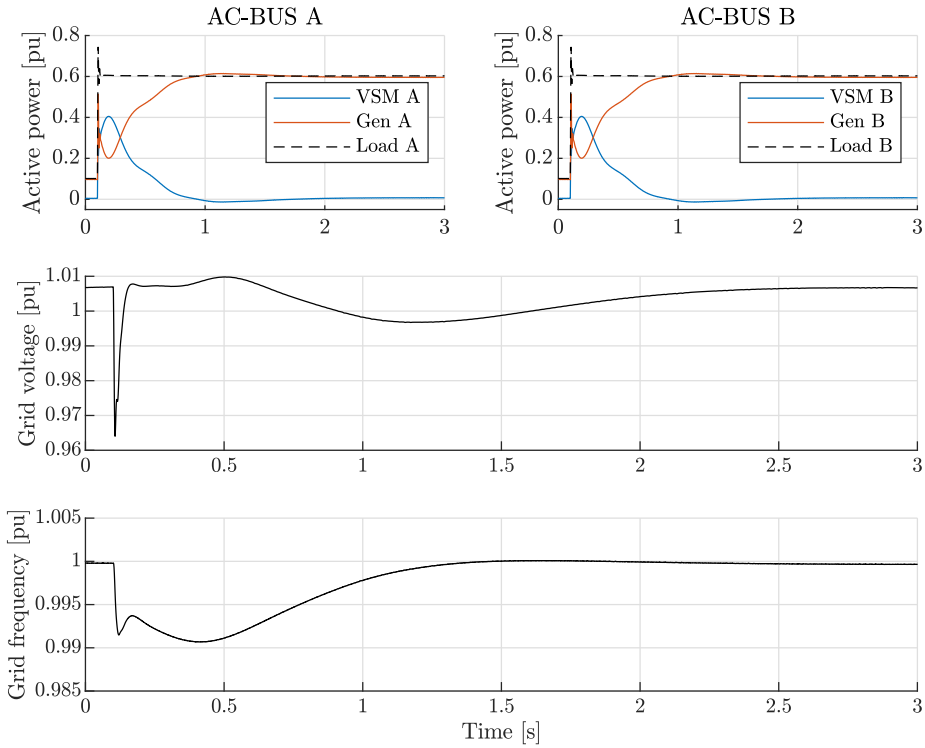

Figure 4.23: Load sharing with closed bus-ties

Chapter 5

Conclusion and further work

5.1 Conclusion

The marine industry and ship owners are always searching for methods to reduce operational costs, maintenance costs, and GHG emissions to increase overall profitability. In the last decade, the number of hybrid power systems has increased steadily. Hybrid power systems are now often the preferred choice in new builds due to the potential energy savings of optimizing the load situation using a battery as energy storage and power reserve. While adding batteries in DC systems can immediately result in increased grid stability and simplified regulation of the DC-bus voltage due to the immediate energy reserve supplied by the batteries. Is short-term stability AC systems fundamentally different and related to the energy stored in rotating mass connected to the grid, also known as system inertia. Because grid-following ESSs rely on generators to form and maintain a stable grid, are ships limited by the available inertia rather than the actual power reserve of the grid. This lack of inertia will limit available thrust and, in some critical operations where this is unacceptable, will require an increased number of spinning generators.

This report studied how the grid-forming VSM-based ESS improves AC systems in terms of dynamical response, provides an emission-free spinning reserve, and enables islanded operation during low loads. The VSM-based ESS has shown promising results by increasing grid stability due to virtual inertia and fast primary control. This increase in grid stability translates to less grid voltage and frequency variations

during transients and changes in load. The VSM also enables seamless transitions between islanded and muli-power operations of the grid using energy stored in the battery. While the islanded operation is not limited to the VSM architecture, will a transition between multi-power and islanded operation with grid-following inverters requires a changeover in the control structure, increasing the system's complexity. The dual-infeed configuration also shows that the system can operate with a "virtually" closed bus tie. This "virtually" closed bus tie enables energy transfer between AC bus A and B during critical operations requiring a split bus configuration to increase power reliability. Therefore, due to the virtually closed bus tie, the system can configure and optimize the generator sets depending on the actual load as if the main bus tie were closed, reducing operational costs and GHG emissions during critical operations.

The results also show that the QSEM-based VSM behaved as expected in multi-power grids, resulting in increased grid stability, and load sharing between VSMs and generators is shared equally during transients and steps in active or reactive load with a steady state controlled by the power reference. However, during islanded operation of the QSEM-based VSM has shown stability issues at low loads and increased sensitivity toward inner loop tuning. As a result, does the QSEM-based VSM require a VSC with a well-tuned SRF current controller and feed-forward terms. Alternatively, can an increased virtual stator resistance improve system stability if the VSC is near the stability-limit. Islanded operation of the QSEM-based VSM also showed increased sensitivity towards filtering of the QSEM voltage feedback independent of load. Therefore to ensure stable operation of the VSM in all operation modes, it is essential to tune this crossover frequency for islanded operation to prevent instability when transitioning from multi-power to islanded operation. When it comes to stator inductance, is this a balance between creating an over-sensitive VSM with a small inductance and an increased amount of oscillation in the grid as the inductance increases. Finally, results show that the QSEM-based VSM is robust against harmonic caused by diode rectifiers and has no issues operating the grid islanded with noisy loads.

5.2 Further work

5.2.1 Laboratory tests to verify the QSEM architecture

The simulation results of the VSM-based ESS using the QSEM architecture are promising, and it would be interesting to conduct laboratory tests to verify the QSEM architecture islanded and and in a microgrid. The actual risk of implementing a full-scale project is also limited. Because the hardware/inner loop of the QSEM-based VSM and a PLL-based VSC is the same, can the control structure for a VSM-based ESS be tested on an ESS based on PLL-based VSCs, and potentially upgrade the ESS to a VSM control structure.

5.2.2 EMS using a VSM-based ESS

An EMS is used to optimize energy production depending on the current load and the expected load depending on current and planned operations. The main intention of EMS is to reduce operational costs, maintenance costs, and GHG emissions. The increased flexibility of the dual-infeed VSM-based ESS can utilize the EMS as the enabling tool to decrease operational costs, maintenance costs, and GHG emissions.

An interesting study would then look at the potential for savings in operational costs, maintenance costs, and GHG emissions using a dual-infeed VSM-based ESS to support the EMS. This study could potentially include a comparison between the VMS-based solution, a grid following solution using traditional VSC, and a DC-distributed system with variable speed generators [12]. Moreover, do a cost-benefit analysis comparing a ”virtually” closed bus-tie using dual-infeed compared two separate VMS-based ESS to support each bus during operations with open bus-ties.

Bibliography

[1] UNFCCC, "Adoption of the paris agreement," 2015.

[2] DNV. "Cii – carbon intensity indicator." (), [Online]. Available: https://tinyurl.com/2p8ucvae (visited on 04/30/2022).

[3] ——, "Key drivers." (), [Online]. Available: https://tinyurl.com/4nustv5e (visited on 05/26/2022).

[4] IMO. "Energy efficiency measures." (), [Online]. Available: https://tinyurl.com/yfcxd9bc (visited on 05/30/2022).

[5] ——, "Guidelines to support new carbon intensity cutting measures agreed by working group ahead of mepc." (), [Online]. Available: https://tinyurl.com/34d79knf (visited on 04/11/2022).

[6] G. P. Haugom, M. A. Røe, N. Mjøs, E. Mollestad, and L. O. Valøen, "The future is hybrid," 2015.

[7] Wartsila. "Electric propulsion systems, electric drive systems." (), [Online]. Available: https://tinyurl.com/bj5twsn4 (visited on 04/04/2022).

[8] DNV. "Leading the charge." (), [Online]. Available: https://tinyurl.com/5yhwd9tk (visited on 04/30/2022).

[9] C. Bordin and O. Mo, "Including power management strategies and load profiles in the mathematical optimization of energy storage sizing for fuel consumption reduction in maritime vessels," *Journal of Energy Storage*, vol. 23, pp. 425–441, 2019.

[10] J. Hamilton, M. Negnevitsky, and X. Wang, "The potential of variable speed diesel application in increasing renewable energy source penetration," *Energy Procedia*, vol. 160, pp. 558–565, 2019.

[11] E. Skjong, T. A. Johansen, M. Molinas, and A. J. Sørensen, "Approaches to economic energy management in diesel–electric marine vessels," *IEEE Transactions on Transportation Electrification*, vol. 3, no. 1, pp. 22–35, 2017.

[12] Simens-Energy. "Bluedrive plusc." (), [Online]. Available: `https://tinyurl.com/4sje8xxk` (visited on 04/19/2022).

[13] DNV, "Rules for classification - ships - newbuildings - special equipment and system additional class pt.6 ch.7," 2011.

[14] ——, "Analysis of charging- and shore power infrastructure in norwegian ports - recharge," 2017.

[15] Miljødirektoratet. "Tiltak og virkemidler mot 2030." (2020), [Online]. Available: `https://tinyurl.com/yebw2nap` (visited on 04/19/2022).

[16] DNV, "Rules for classification - ships - newbuildings - special equipment and system additional class pt.6 ch.2," 2011.

[17] K. Kim, K. Park, G. Roh, and K. Chun, "Dc-grid system for ships: A study of benefits and technical considerations," *Journal of International Maritime Safety, Environmental Affairs, and Shipping*, vol. 2, no. 1, pp. 1–12, 2018.

[18] X. Pei, O. Cwikowski, D. S. Vilchis-Rodriguez, M. Barnes, A. C. Smith, and R. Shuttleworth, "A review of technologies for mvdc circuit breakers," in *IECON 2016-42nd Annual Conference of the IEEE Industrial Electronics Society*, IEEE, 2016, pp. 3799–3805.

[19] J. Rocabert, A. Luna, F. Blaabjerg, and P. Rodriguez, "Control of power converters in ac microgrids," *IEEE transactions on power electronics*, vol. 27, no. 11, pp. 4734–4749, 2012.

[20] P. Tielens and D. Van Hertem, "The relevance of inertia in power systems," *Renewable and Sustainable Energy Reviews*, vol. 55, pp. 999–1009, 2016.

[21] P. Makolo, R. Zamora, and T.-T. Lie, "The role of inertia for grid flexibility under high penetration of variable renewables-a review of challenges and solutions," *Renewable and Sustainable Energy Reviews*, vol. 147, p. 111 223, 2021.

[22] E. Spahic, D. Varma, G. Beck, G. Kuhn, and V. Hild, "Impact of reduced system inertia on stable power system operation and an overview of possible solutions," in *2016 IEEE power and energy society general meeting (PESGM)*, IEEE, 2016, pp. 1–5.

[23] E. Skjong, "Bluectrl data set sampled form 11. december 2021 to 11. january 2022," unpublished, 2022.

[24] "Github repository." (), [Online]. Available: `https://github.com/haakenl/TTK4900-Master-Thesis` (visited on 06/15/2022).

[25] O. I. Elgerd, *Electric Energy Systems Theroy*, 2nd ed. McGraw-Hill, INC, 1982.

[26] D. Beeman, *Industrial Power Systems Handbook*, 1st ed. McGraw-Hill, INC, 1955.

[27] S. Buso and P. Mattavelli, *Digital Control in Power Electronics*, 1st ed. Morgan & Claypool, 2006.

[28] J. Machowski, J. W. Bialek, and J. R. Bumby, *Power Systems Dynamics Stability and Control*, 2nd ed. John Wiley & Sons, Ltd, 2008.

[29] C. Bajracharya, M. Molinas, J. A. Suul, T. M. Undeland, *et al.*, "Understanding of tuning techniques of converter controllers for vsc-hvdc," in *Nordic Workshop on Power and Industrial Electronics (NORPIE/2008), June 9-11, 2008, Espoo, Finland*, Helsinki University of Technology, 2008.

[30] J. Rocabert, A. Luna, F. Blaabjerg, and P. Rodriguez, "Control of power converters in ac microgrids," *IEEE transactions on power electronics*, vol. 27, no. 11, pp. 4734–4749, 2012.

[31] H. S. Lunn, "Analysis of system configurations for integration of a single battery installation in a two-bus ship power system," unpublished, 2021.

[32] W. Zhao and G. Chen, "Comparison of active and passive damping methods for application in high power active power filter with lcl-filter," in *2009 International Conference on Sustainable Power Generation and Supply*, IEEE, 2009, pp. 1–6.

[33] O. Mo, S. D'Arco, and J. A. Suul, "Evaluation of virtual synchronous machines with dynamic or quasi-stationary machine models," *IEEE Transactions on industrial Electronics*, vol. 64, no. 7, pp. 5952–5962, 2016.

[34] N. Mohan, T. M. Undeland, and W. P. Robbins, *Power Electronics*, 3rd ed. John Wiley & Sons, INC, 2003.

[35] S. Chiniforoosh, J. Jatskevich, A. Yazdani, *et al.*, "Definitions and applications of dynamic average models for analysis of power systems," *IEEE Transactions on Power Delivery*, vol. 25, no. 4, pp. 2655–2669, 2010.

[36] N. Flourentzou, V. G. Agelidis, and G. D. Demetriades, "Vsc-based hvdc power transmission systems: An overview," *IEEE Transactions on power electronics*, vol. 24, no. 3, pp. 592–602, 2009.

[37] D. G. Holmes and T. A. Lipo, *Pulse Width Modulation For Power Converters, Principles and Practice*, 1st ed. John Wiley & Sons, INC, 2003.

[38] H.-P. Beck and R. Hesse, "Virtual synchronous machine," in *2007 9th International Conference on Electrical Power Quality and Utilisation*, IEEE, 2007, pp. 1–6.

[39] M. Van Wesenbeeck, S. De Haan, P. Varela, and K. Visscher, "Grid tied converter with virtual kinetic storage," in *2009 IEEE Bucharest PowerTech*, IEEE, 2009, pp. 1–7.

[40] S. D'Arco, J. A. Suul, and O. B. Fosso, "A virtual synchronous machine implementation for distributed control of power converters in smartgrids," *Electric Power Systems Research*, vol. 122, pp. 180–197, 2015.

[41] Y. Hirase, K. Abe, K. Sugimoto, and Y. Shindo, "A grid-connected inverter with virtual synchronous generator model of algebraic type," *Electrical Engineering in Japan*, vol. 184, no. 4, pp. 10–21, 2013.

[42] K.-i. Sakimoto, K. Sugimoto, and Y. Shindo, "Low voltage ride through capability of a grid connected inverter based on the virtual synchronous generator," in *2013 IEEE 10th International Conference on Power Electronics and Drive Systems (PEDS)*, IEEE, 2013, pp. 1066–1071.

[43] S. D'Arco and J. A. Suul, "Virtual synchronous machines—classification of implementations and analysis of equivalence to droop controllers for microgrids," in *2013 IEEE Grenoble Conference*, IEEE, 2013, pp. 1–7.

[44] DNV, "Rules for classification - ships - newbuildings - special equipment and system additional class pt.4 ch.8," 2018.

[45] F. O. Igbinovia, G. Fandi, Z. Muller, and J. Tlusty, "Reputation of the synchronous condenser technology in modern power grid," in *2018 International Conference on Power System Technology (POWERCON)*, IEEE, 2018, pp. 2108–2115.

[46] MathWorks. "Synchronous machine pu fundamental." (), [Online]. Available: `https://tinyurl.com/2w7h74wv` (visited on 06/15/2022).

[47] IEEE, "Guide for synchronous generator modeling practices and parameter verification with applications in power system stability analyses," *IEEE Std 1110-2019 (Revision of IEEE Std 1110-2002)*, pp. 1–92, 2020.

[48] A. E. Fitzgerald, J. Charles Kingsley, and S. D. Umans, *Electric Machinery*, 6th ed. McGraw-Hill, INC, 2003.

[49] E. F. Fuchs and M. A. Masoum, *Power quality in power systems and electrical machines*. Academic press, 2011.

[50] P. Kundur, *Power Systems Stability and Control*, 2nd ed. McGraw-Hill, INC, 1993.

[51] M. A. Dijkman, "Solving the lng load response challenge," 2016.

[52] J. J. Shea, *Vfd challenges for shipboard electrical power system design*, 2020.

[53] M. Ohta and S. Fukuda, "Twelve-pulse diode rectifier with reduced input current harmonics," in *The Fifth International Conference on Power Electronics and Drive Systems, 2003. PEDS 2003.*, IEEE, vol. 2, 2003, pp. 1442–1447.

[54] MathWorks. "Three-phase transformer (three windings)." (), [Online]. Available: `https://tinyurl.com/mrx4bkz7` (visited on 06/15/2022).

[55] ——, "Three-phase parallel rlc load." (), [Online]. Available: `https://tinyurl.com/ytj4hevn` (visited on 06/15/2022).

[56] R. Barrera-Cardenas, O. Mo, and G. Guidi, "Optimal sizing of battery energy storage systems for hybrid marine power systems," in *2019 IEEE Electric Ship Technologies Symposium (ESTS)*, IEEE, 2019, pp. 293–302.

[57] M. Godjevac, B. Mestemaker, K. Visser, *et al.*, "Electrical energy storage for dynamic positiong operations: Investigation of three application case," in *2017 IEEE Electric Ship Technologies Symposium (ESTS)*, IEEE, 2017, pp. 182–186.

[58] DNV, "Handbook for hydrogen-fuelled vessels," 2021.

[59] MathWorks. "Three-phase breaker." (), [Online]. Available: `https://tinyurl.com/bdk2p53u` (visited on 06/15/2022).

[60] W. Zhang, L. Wang, L. Wang, C. Liao, and Y. Zhang, "Joint state-of-charge and state-of-available-power estimation based on the online parameter identification of lithium-ion battery model," *IEEE Transactions on Industrial Electronics*, vol. 69, no. 4, pp. 3677–3688, 2021.

[61] F. Sun, R. Xiong, and H. He, "Estimation of state-of-charge and state-of-power capability of lithium-ion battery considering varying health conditions," *Journal of Power Sources*, vol. 259, pp. 166–176, 2014.

[62] A. Anvari-Moghaddam, T. Dragicevic, L. Meng, B. Sun, and J. M. Guerrero, "Optimal planning and operation management of a ship electrical power system with energy storage system," in *IECON 2016-42nd Annual Conference of the IEEE Industrial Electronics Society*, IEEE, 2016, pp. 2095–2099.

[63] W. L. Brogan, *Modern control theory*. Pearson education india, 1991.

Appendix A

Per unit electrical inductance SM model

$$\mathbf{v^r} = \left[v_d, v_q, v_f, 0, 0\right]^T \tag{A.1}$$

$$\mathbf{i^r} = \left[i_d, i_q, i_f, i_{kd}, i_{kq}\right]^T \tag{A.2}$$

$$\mathbf{r^r} = \begin{bmatrix} r_s & 0 & 0 & 0 & 0 \\ 0 & r_s & 0 & 0 & 0 \\ 0 & 0 & r_{fd} & 0 & 0 \\ 0 & 0 & 0 & r_{kd} & 0 \\ 0 & 0 & 0 & 0 & r_{kq} \end{bmatrix} \tag{A.3}$$

$$\mathbf{l^r} = \begin{bmatrix} l_{ls} + l_{md} & 0 & l_{md} & l_{md} & 0 \\ 0 & l_{ls} + l_{mq} & 0 & 0 & l_{mq} \\ l_{md} & 0 & l_{lfd} + l_{f1d} + l_{md} & l_{lkd} & 0 \\ l_{md} & 0 & l_{md} + l_{f1d} & l_{lkd} + l_{f1d} + l_{md} & 0 \\ 0 & l_{mq} & 0 & 0 & l_{lkq} + l_{md} \end{bmatrix} \tag{A.4}$$

$$\omega_r \mathbf{J\Psi^r} = \begin{bmatrix} 0 & -\omega_r(l_{ls} + l_{mq}) & 0 & 0 & -\omega_r l_{mq} \\ \omega_r(l_{ls} + l_{md}) & 0 & \omega_r l_{md} & \omega_r l_{md} & 0 \\ 0 & 0 & 0 & 0 & 0 \\ 0 & 0 & 0 & 0 & 0 \\ 0 & 0 & 0 & 0 & 0 \end{bmatrix} \begin{bmatrix} i_d \\ i_q \\ i_f \\ i_{kd} \\ i_{kq} \end{bmatrix} \tag{A.5}$$

Appendix B

Small signal model

To verify some of the findings during islanded operation of the QSEM-based VSM in this report, have authors of [33] provided a small-signal model of the QSEM-based VSM.

For this project, the nonlinear state-space model (B.1) consists of eighteen first-order ordinary differential equations (B.5) to (B.22) describing the QSEM-based VSM, slightly modified to operate islanded with a constant impedance load, and a voltage droop has replaced the voltage controller (AVR).

$$\frac{d\mathbf{x_i}}{dt} = \mathbf{f_i}(\mathbf{x_1}, \mathbf{x_2}, ..., \mathbf{x_n}, \mathbf{u_1}, \mathbf{u_2}, ...\mathbf{u_r}, \mathbf{t}) \qquad i = 1, 2, ..., n \tag{B.1}$$

In order to study the nonlinear power system in steady-state, a small signal model of the system is made by linearizing the state-space model (B.2) using a Taylor's series expansion around the equilibrium point $\mathbf{x_0}$, where Δ denotes small deviations in $\mathbf{x}$ [50]. $\mathbf{x_0}$ is determine by solving $f(x, u) = 0$.

$$\frac{d\mathbf{x_i}}{dt} \approx \frac{d\mathbf{x_{i0}}}{dt} + \frac{d\mathbf{\Delta x_i}}{dt} = \mathbf{f}[(\mathbf{x_0}, \mathbf{\Delta x}), (\mathbf{u_0}, \mathbf{\Delta u})] \tag{B.2}$$

The linearized small-signal model is typically generalized on matrix form (B.3), where vector $\mathbf{x}$ repents the system states, $\mathbf{y}$ the system outputs, and $\mathbf{u}$ the system inputs [63]. Combined with system matrix $\mathbf{A}$, input matrix $\mathbf{B}$, output matrix $\mathbf{C}$, and feedforward

matrix **D**, the generalized state-space model describes the entire system around the equilibrium point $\mathbf{x_0}$.

$$\begin{aligned} \frac{d\mathbf{\Delta x}}{dt} &= \mathbf{A}(\mathbf{x_0}, \mathbf{u_0})\mathbf{\Delta x} + \mathbf{B}(\mathbf{x_0}, \mathbf{u_0})\mathbf{\Delta u} \\ \mathbf{\Delta y} &= \mathbf{C}(\mathbf{x_0}, \mathbf{u_0})\mathbf{\Delta x} + \mathbf{D}(\mathbf{x_0}, \mathbf{u_0})\mathbf{\Delta u} \end{aligned} \tag{B.3}$$

The eigenvalues λ system matrix $\mathbf{A}(x_0)$ describes the stability properties of a small-signal model around x_0. For non-trivial solutions, the characteristic equation (B.4) determines the system's eigenvalues.

$$det(\mathbf{A}(\mathbf{x_0}, \mathbf{u_0}) - \lambda \mathbf{I}) = 0 \tag{B.4}$$

These eigenvalues can either be real, imaginary, or a combination, where the two latter ones always occur in complex conjugate pairs. Lyapunov's first method state that stability in the small of a nonlinear system is given by the eigenvalues of A, and the system is asymptotically stable if all eigenvalues have negative real part $\lambda < 0$ and unstable if at least one eigenvalue has a positive real part $\lambda > 0$. When the eigenvalues have real parts equal to zero, it is not possible to determine stability based on the first approximation and requires further investigation using Lyapunov's second method

$$\frac{dv_{f,d}}{dt} = \omega_b \omega_{VSM} v_{f,q} + \frac{\omega_b}{c_f} i_{c,d} - \frac{\omega_b}{c_f} i_{h,d} \tag{B.5}$$

$$\frac{dv_{f,q}}{dt} = -\omega_b \omega_{VSM} v_{f,d} + \frac{\omega_b}{c_f} i_{c,q} - \frac{\omega_b}{c_f} i_{h,q} \tag{B.6}$$

$$\begin{aligned} \frac{di_{c,d}}{dt} = &-\frac{\omega_b \left(1 - k_{ffv} + k_{ad}\right)}{l_f} v_{f,d} - \frac{\omega_b \left(k_{pc} + r_{lf}\right)}{l_f} i_{c,d} + \frac{\omega_b k_{ic}}{l_f} \gamma_d - \frac{\omega_b k_{ad}}{l_f} \varphi_d \\ &- \frac{\omega_b k_{pc} r_{vs}}{l_f \left(r_{vs}^2 + \omega_{VSM}^2 l_{vs}^2\right)} v_{m,d} - \frac{\omega_b k_{pc} l_{vs}}{l_f \left(r_{vs}^2 + \omega_{VSM}^2 l_{vs}^2\right)} \omega_{VSM} v_{m,q} \\ &- \frac{\omega_b k_{pc} k_{dr,pq} r_{vs}}{l_f \left(r_{vs}^2 + \omega_{VSM}^2 l_{vs}^2\right)} q_m + \frac{\omega_b k_{pc} k_{dr,pq} r_{vs}}{l_f \left(r_{vs}^2 + \omega_{VSM}^2 l_{vs}^2\right)} q^* + \frac{\omega_b k_{pc} r_{vs}}{l_f \left(r_{vs}^2 + \omega_{VSM}^2 l_{vs}^2\right)} \hat{v}^* \end{aligned} \tag{B.7}$$

$$\begin{aligned}\frac{di_{c,q}}{dt} &= -\frac{\omega_b\left(1-k_{ffv}+k_{ad}\right)}{l_f}v_{f,q} - \frac{\omega_b\left(k_{pc}+r_{lf}\right)}{l_f}i_{c,q} + \frac{\omega_b k_{ic}}{l_f}\gamma_q - \frac{\omega_b k_{ad}}{l_f}\varphi_q \\ &- \frac{\omega_b k_{pc}}{l_f r_s}v_{m,q} + \frac{\omega_b k_{pc} l_{vs}}{l_f\left(r_{vs}^2+\omega_{VSM}^2 l_{vs}^2\right)}\omega_{VSM}v_{m,d} - \frac{\omega_b k_{pc} r_{vs} l_{vs}}{l_f\left(r_{vs}^2+\omega_{VSM}^2 l_{vs}^2\right)}v_{m,q} \\ &+ \frac{\omega_b k_{pc} k_{dr,pq} k_q l_{vs}}{l_f\left(r_{vs}^2+\omega_{VSM}^2 l_{vs}^2\right)}\omega_{VSM}q_m - \frac{\omega_b k_{pc} k_q l_{vs}}{l_f\left(r_{vs}^2+\omega_{VSM}^2 l_{vs}^2\right)}\omega_{VSM}q^* \\ &- \frac{\omega_b k_{pc} l_{vs}}{l_f\left(r_{vs}^2+\omega_{VSM}^2 l_{vs}^2\right)}\omega_{VSM}\hat{v}^* \frac{\omega_b k_{pc}}{l_f r_s}v_{m,q}\end{aligned} \tag{B.8}$$

$$\begin{aligned}\frac{d\gamma_d}{dt} &= -i_{c,d} - \frac{r_{vs}}{r_{vs}^2+\omega_{VSM}^2 l_{vs}^2}v_{m,d} - \frac{l_{vs}}{r_{vs}^2+\omega_{VSM}^2 l_{vs}^2}\omega_{VSM}v_{m,q} \\ &- \frac{k_{dr,pq} r_{vs}}{r_{vs}^2+\omega_{VSM}^2 l_{vs}^2}q_m + \frac{k_{dr,pq} r_{vs}}{r_{vs}^2+\omega_{VSM}^2 l_{vs}^2}q^* + \frac{r_{vs}}{r_{vs}^2+\omega_{VSM}^2 l_{vs}^2}\hat{v}^*\end{aligned} \tag{B.9}$$

$$\begin{aligned}\frac{d\gamma_q}{dt} &= -i_{c,q} + \frac{l_{vs}}{r_{vs}^2+\omega_{VSM}^2 l_{vs}^2}\omega_{VSM}v_{m,d} - \frac{r_{vs}}{r_{vs}^2+\omega_{VSM}^2 l_{vs}^2}v_{m,q} \\ &+ \frac{k_{dr,pq} k_q l_{vs}}{r_{vs}^2+\omega_{VSM}^2 l_{vs}^2}\omega_{VSM}q_m - \frac{k_{dr,pq} l_{vs}}{r_{vs}^2+\omega_{VSM}^2 l_{vs}^2}\omega_{VSM}q^* - \frac{l_{vs}}{r_{vs}^2+\omega_{VSM}^2 l_{vs}^2}\omega_{VSM}\hat{v}^*\end{aligned} \tag{B.10}$$

$$\frac{di_{h,d}}{dt} = \frac{\omega_b}{l_h}v_{f,d} - \frac{\omega_b r_h}{l_g}i_{h,d} + \omega_b\omega_{VSM}i_{h,q} \tag{B.11}$$

$$\frac{di_{h,q}}{dt} = \frac{\omega_b}{l_g}v_{f,q} - \frac{\omega_b r_h}{l_h}i_{h,q} - \omega_b\omega_{VSM}i_{h,d} \tag{B.12}$$

$$\frac{d\varphi_d}{dt} = \omega_{ad}v_{f,d} - \omega_{ad}\varphi_d \tag{B.13}$$

$$\frac{d\varphi_q}{dt} = \omega_{ad}v_{f,q} - \omega_{ad}\varphi_q \tag{B.14}$$

$$\frac{dv_{m,d}}{dt} = \omega_{vf} v_{f,d} - \omega_{vf} v_{m,d} \tag{B.15}$$

$$\frac{dv_{m,q}}{dt} = \omega_{vf} v_{f,q} - \omega_{vf} v_{m,q} \tag{B.16}$$

$$\frac{dq_m}{dt} = -i_{h,q} v_{f,d} \omega_{qf} + i_{h,d} v_{f,q} \omega_{qf} - q_m \omega_{qf} \tag{B.17}$$

$$\begin{aligned}\frac{d\omega_{VSM}}{dt} = &-\frac{1}{T_a} i_{h,d} v_{f,d} - \frac{1}{T_a} i_{h,q} v_{f,q} - \frac{(k_d + k_\omega)}{T_a} \omega_{VSM} + \frac{1}{T_a} p^* + \frac{k_\omega}{T_a} \omega^*_{VSM} \\ &+ \frac{k_d k_{i\delta}}{T_a} \delta_f + \frac{k_d k_{p\delta}}{T_a} \arctan\left(\frac{v_{PLL,q}}{v_{PLL,d}}\right) + \frac{k_d f_b}{T_a}\end{aligned} \tag{B.18}$$

$$\frac{dv_{PLL,d}}{dt} = -v_{PLL,d} \omega_f + v_{f,d} \omega_f \cos(\delta\theta_{PLL}) + v_{f,q} \omega_f \sin(\delta\theta_{PLL}) \tag{B.19}$$

$$\frac{dv_{PLL,q}}{dt} = -v_{PLL,q} \omega_f + v_{f,q} \omega_f \cos(\delta\theta_{PLL}) - v_{f,d} \omega_f \sin(\delta\theta_{PLL}) \tag{B.20}$$

$$\frac{d\delta_f}{dt} = \arctan\left(\frac{v_{PLL,q}}{v_{PLL,d}}\right) \tag{B.21}$$

$$\frac{d\delta\theta_{PLL}}{dt} = k_{i\delta} \delta_f \omega_b + \omega_b f_b - \omega_b \omega_{VSM} + k_{p\delta} \omega_b \arctan\left(\frac{v_{PLL,q}}{v_{PLL,d}}\right) \tag{B.22}$$

Appendix C

Scientific publication under preparation

Parts of the work presented in this thesis is currently being extended to provide input to a manuscript for a scientific publication that is currently under preparation. The intention is to submit the manuscript to the 2022 IEEE International Power and Renewable Energy Conference, 16-18 December 2022, Karunagappally, India, with the following details.

Title: Stability Limits of Current Controlled Virtual Synchronous Machines under Islanded Operation

Authors: Salvatore D'Arco, Håken Sivesindtajet Lunn, Jon Are Suul

Abstract: Current Controlled (CC) Virtual Synchronous Machines (VSMs) offer a simple control implementation and good dynamic performance in grid connected operation but can experience stability problems in islanded conditions with low load. This paper presents a systematic evaluation of the small-signal stability limits for a CC VSM with a Quasi-Stationary Electrical Model (QSEM) representing the virtual stator impedance, and a power-balance-based virtual swing equation for representing the emulated rotor dynamics of a synchronous machine. Eigenvalue analysis of a linearized state-space model is presented to identify the sources of the stability problems. The results shown how the parameters of the current controller loop, the voltage-feed-forward and any active damping algorithm for suppressing LC oscillations influence

the stability limits. Furthermore, it is shown how the virtual stator resistance can have a strong damping effect on the critical eigenvalues. Systematic mapping of the stability regions as a function of the load resistance and the parameters of the CC VSM leads to recommendations for parameter tuning that can ensure stable operation in the full range of loading conditions. Time-domain simulations and experimental results are presented as validation of the results from the theoretical analysis.

Håken Sivesindtajet Lunn

Master's thesis in Industrial Cybernetics

NTNU
Norwegian University of
Science and Technology